ScuDo
Scuola di Dottorato ~ Doctoral School
WHAT YOU ARE, TAKES YOU FAR

Doctoral dissertation
Doctoral program in Environmental Engineering (29^{th} cycle)

Investigation and optimization of the performance of gravity water wheels

By
Emanuele Quaranta

* * * * **

Supervisor
Roberto Revelli

Doctoral Examination Committee:

Prof. Ilaria Butera

Prof. Walter Franco

Prof. David Lubitz

Prof. Andrea Marion

Prof. Toni Pujol Sagarò

Politecnico di Torino
June, 2017

Declaration

I hereby declare that the contents and organization of this dissertation constitute my own original work and do not compromise in any way the rights of third parties, including those relating to the security of personal data.

Emanuele Quaranta, 2017

emanuele.quaranta@polito.it

quarantaemanuele@yahoo.it

Acknowledgments

I would like to express my acknowledgments to the scientific committee composed of prof. Ilaria Butera, prof. Walter Franco, prof. David Lubitz, prof. Andrea Marion and prof. Toni Pujol. A particular acknowledgment has to be done to the two Reviewers of this work, David Lubitz and Toni Pujol, who have given to me a lot of useful advices and suggestions to improve the thesis. I would like also to acknowledge my supervisor prof. Roberto Revelli for his support during these three years. Finally, I would like to thank prof. Gerald Müller, since he gave to me the opportunity to work with him on water wheels at University of Southampton.

Fundings

The research leading to these results has received funding from ORME (Energy optimization of traditional water wheels) – Granted by Regione Piemonte via the ERDF 2007-2013 (Grant Number: #0186000275)– Partners Gatta srl, BCE srl, Rigamonti Ghisa srl, Promec Elettronica srl and Politecnico di Torino.

Abstract

Water wheels are rotating hydraulic machines that were introduced thousands of years ago to generate energy from water. Gravity water wheels are driven by the weight of the water flow and a portion of the flow kinetic energy. In the last decades, due to the increasing diffusion of micro hydropower plants (installed power less than 100 kW), gravity water wheels are being recognized as attractive hydraulic machines to produce electricity. Unfortunately, most of the engineering knowledge on water wheels is dated back to the XIX century, with several gaps and uncertainty. Additional work is still needed to fully understand the power losses and the performance within water wheels, that could lead to further improvements in efficiency.

The scope of the present thesis is the investigation and improvement of the performance of gravity water wheels. This aim was achieved using physical experiments to quantify water wheels performance under different hydraulic conditions, theoretical models to estimate and predict the efficiency, and numerical simulations to optimize the design. Undershot, breastshot and overshot water wheels were investigated, in order to give a wide overview on all the kinds of gravity water wheels.

Sagebien and *Zuppinger* undershot wheels were investigated at Southampton University, under the supervision of prof. Gerald Müller, from October 2015 until April 2016. These two wheels differ based on the shape of the blades. The blades of *Sagebien* wheels are optimized to reduce the inflow power losses, while those of *Zuppinger* wheels are conceived to minimize the outflow power losses. The objective of the experiments was to understand which of the two designs is better in term of efficiency. The tests showed that the *Sagebien* type exhibits a more constant efficiency as a function of the flow rate and the hydraulic head than the *Zuppinger* type. The maximum efficiency (excluding leakages) was identified as 88%.

Breastshot water wheels were investigated experimentally, theoretically and using numerical Computational Fluid Dynamic (CFD) methods at Politecnico di Torino. The maximum experimental efficiency was estimated as 75% using a sluice gate inflow. A vertical inflow weir was also investigated, and found to have a more constant efficiency versus the rotational speed of the wheel, but with similar maximum values. A theoretical model that was developed to estimate the power output, power losses and efficiency, had a discrepancy with the experiments of 8%. A dimensionless law was also developed to estimate the power output. Numerical CFD simulations were performed to understand the effects of the number

and shape of the blades on the efficiency. The optimal number of blades was 48 for the investigated wheel, and the efficiency can be improved using a circular shape. The numerical discrepancy with experiments was less than 6%.

Overshot water wheels were investigated using a similar approach as done for breastshot wheels, and were found to have a maximum experimental efficiency of 85%. A theoretical model was developed to estimate the power losses and the efficiency, in particular to quantify the volumetric losses at the top of the wheel, that is the fraction of the flow which can not enter into the buckets and that is lost. Then, numerical simulations will be started to try to improve the wheel efficiency, reducing the previous volumetric losses. More specifically, a circular wall around the periphery of the wheel was added to the original design, leading to a performance improvement up to 60%.

The results of this work show that water wheels can be considered attractive hydropower converters.

Contents

List of Figures

List of Tables

Nomenclature

B= width of the channel [m]

C= estimated shaft torque [Nm]

C_{exp}= experimental shaft torque [Nm]

C_D= drag coefficient [-]

D= wheel diameter [m]

H= hydraulic head [m]

H_g= geometric head [m]

H_{gr}= gross head [m]

H_{net}= net head [m]

L= power loss [W]

N= rotational speed [rpm, rad/s]

P = power output [W]

P_{el}= electrical power output [W]

P_{gr}= gross power input [W]

P_{net}= net power input [W]

P_{out}= estimated power output [W]

P_{exp}= experimental power output [W]

Q= flow rate into the wheel [m^3/s]

Q_{gap}= flow through the gaps [m^3/s]

Q_{in} = flow rate of the pump [m^3/s]

R= wheel radius [m]

V= water inside the bucket [m^3]

a= gap height [m]

b= width of the wheel [m]

d= depth of the bucket [m]

g= gravitational acceleration [m/s^2]

h_d= downstream water depth [m]

h_s= height of the weir [m]

h_u= upstream water depth [m]

l= distance between two blades [m]

n= number of blades [-]

n_b= number of wet blades [-]

n_p= number of experiments [-]

u= tangential speed of the wheel [m/s]

v= flow velocity [m/s]

v_d= downstream flow velocity [m/s]

v_e= entering flow velocity [m/s]

v_u= upstream flow velocity [m/s]

w= relative flow velocity [m/s]

α= water surface inclination [rad]

β= angle between two blades [rad]

χ= volumetric loss coefficient [-]

δ= error [-]

η= efficiency [-]

γ= specific weight [N/m^3]

ρ= density [kg/m^3]

ψ= dimensional analysis coefficients [-]

θ= angular coordinate [rad]

ξ= impact coefficient [-]

Brief introduction and summary

Due to the always more increasing attention and sensibility to renewable energy sources, hydropower is playing a central role in satisfying the world energy demand. However, the installation of large hydropower plants is decreasing, due to the adverse effects on the ecosystems. Furthermore, in developed countries few suitable sites are currently available to accommodate for large hydro plants. Therefore, small scale hydropower plants, called micro or mini hydropower plants (installed power lower than 100 kW and 1 MW, respectively) are spreading worldwide. These plants exploit sites with low heads (few meters or few tens of meters head) and discharges (few cubic meters per second); these sites are present in almost all countries. For example, it is estimated that in Europe 350,000 sites suitable for mini/micro hydro plants are available.

The advantages of micro hydropower over larger hydro schemes are several, and different micro hydropower converters can be identified. But, being micro hydropower a relative new field, there is still the need of improve its technology and potential. In particular, there exists the need of a simple and cost effective micro hydropower converter for the exploitation of very low heads (few meters) and discharges. Gravity machines can be attractive technologies for these purposes. They exploit mainly the water weight, and they generally rotate slower than common turbines. Gravity machines are suitable to be installed in flowing water, with very low impacts on ecosystems and, especially, on fish. In chapter 1 a brief literature review on the most common micro hydropower converters and its status will be presented.

Among gravity machines, it is possible to distinguish mainly Archimedes screws and water wheels; the investigation of water wheels will be the aim of the present thesis. Water wheels were in widespread use until the nineteenth century, since they were an important component of water mills. Unfortunately, they were forgotten in the twentieth century, as a consequence of the advent of modern turbines. Nowadays, thanks to the new rebirth of micro hydro, water wheels are being recognized as attractive hydropower converters in very low head sites. However, there is still a lack of engineering and scientific knowledge on water

wheels; most of the available data is dated back to more than one century ago. Some experimental tests were performed during the modern era, but they are very few; the available theoretical models are often not very accurate and not complete. A lot of design suggestions are empirical, with no scientific evidence. In chapter 2 a literature review on water wheels will be reported.

Therefore, there exists the possibility to still improve the scientific knowledge on water wheels, and the need to achieve better engineering rules and data to use for the design of water wheels, thus for engineering applications. With these aims, in chapter 3, chapter 4 and chapter 5, breastshot, overshot and undershot (*Sagebien* and *Zuppinger*) water wheels, respectively, will be investigated. Experimental tests will be presented to determine the performance of these machines and to understand their optimal working conditions. The efficiency will be presented as a function of flow rate, hydraulic head and wheel rotational speed. Theoretical models will be developed to estimate the power losses, hence the efficiency, and they will be compared to older ones. Numerical simulations will be also performed to optimize the performance as a function of the wheel geometry: breastshot wheels will be investigated for different blades numbers and shapes, while overshot wheels will be simulated with an additional wall along the wheel periphery.

The achieved results will demonstrate that the efficiency of water wheels is very good, and it remains optimal over a wide range of external hydraulic conditions. One other important result is that the maximum efficiency of water wheels is affected by the geometry and external hydraulic conditions: the blade shape, the number of blades and the rotational speed, for example, are important factors that affect the water wheel performance, and that should be taken into account in the design.

Therefore, writing this thesis I hope to shed more light on water wheels and to attract the public interest into this old, but still competitive, technology.

Chapter 1

Introduction: Micro Hydropower

1.1 Current energy situation and potential: the role of micro hydropower

For the next decades, the International Energy Agency (2013) forecasts an increase in energy demand, developing two possible scenarios. The first scenario foresees an overall increase in energy demand, especially in China and India. According to this model, fossil fuels will constitute the main sources of energy. Coal will undergo the greatest growth in absolute terms, while oil may remain the most widely used fuel. This situation would lead to an increase in the level of emissions. A second possible scenario is, instead, the possibility of a long-term transition towards a model of renewable energy and sustainable development. Therefore, in order to make the second scenario realizable, in the European Commission legislations, large scale electricity production from renewable sources is becoming a major purpose to limit greenhouse gas emissions (Bódis et al., 2014). As a consequence, a new and wide interest on renewable sources is spreading in Europe and also worldwide, especially the energy production by wind, solar and hydro power.

Figure 1.1 shows the usage proportion of each renewable energy source till end of year 2008. It can be seen from Fig.1.1 that among renewable energy sources, large hydropower, biomass heating, solar heating system, wind and mini hydro (installed power less than 1 MW) play a significant role in supplying the electricity demand. For what concerns with Italy, 28% of the total consumed energy is from renewable sources, divided as follows: 15.0% hydropower, 6.5% solar energy, 4.6% wind energy and 1.8% geothermal energy (Terna Rete Italia, 2012). Therefore, hydropower, wind and solar power play a significant role, both in Italy and also at a global scale.

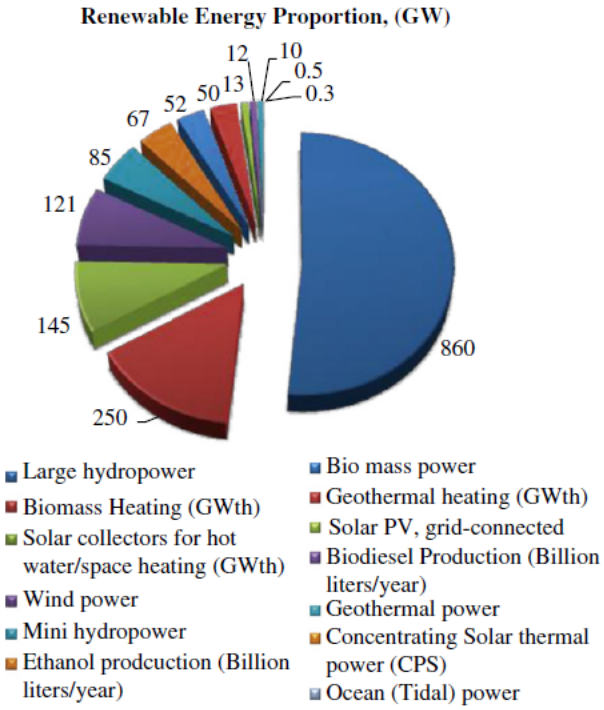

Fig. 1.1. Global installed capacity of renewable energy sources (Laghari et al., 2013).

Generally speaking, with respect to wind and solar power, hydroelectricity generally exhibits some advantages: hydro plants can be managed by human control easier (they are more responsive to load management requirements) and hydro output is more predictable than solar and wind output, because the flow rate can be controlled using dams. Furthermore, the drawback of wind and solar resources is their daily variability, hence they need of additional storage capacity (Bódis et al., 2014). Figure 1.2 depicts the exploited hydropower potential for each continent. It can be seen from Fig.1.2 that Asia, Africa and South America still have a large potential for hydropower which has not been exploited yet.

However, the hydropower potential on large scale has been exploited in almost every part of the world, especially in Europe; moreover the environmental impacts of large dams are generally not well accepted. Mini/micro/pico hydropower (installed power lower than 1 MW, 100 kW and 5 kW, respectively) is instead considered to be more sustainable, due to its simple technology, eco-sustainability and short payback periods. The mini hydro energy source is available in almost every country of the world. Mini hydro plants are becoming attractive also because they can be more diffused on the territory, and they are particularly suitable in rural and decentralized areas for self-sustainment. In Laghari et al. (2013), the

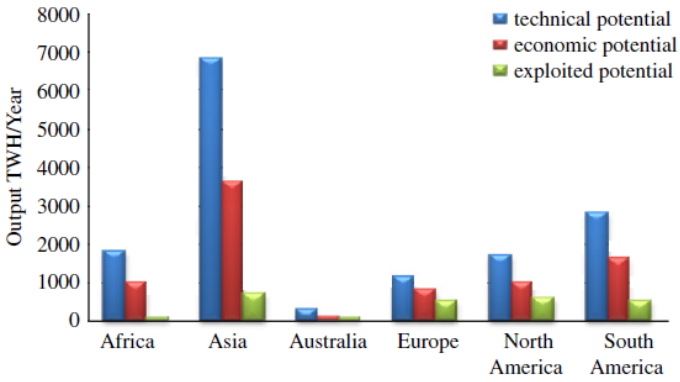

Fig. 1.2. Hydro potential by continent (Laghari et al. 2013).

adaptation of mini hydro schemes is considered as the most economical option for rural electrification (in this paper a general overview of new designs in the electrical equipment and controllers of mini hydropower plants is also shown). In the industrialized countries, mini/micro hydropower is also important for meeting the non-fossil fuel targets, while in emerging countries and developing worlds it may contribute to satisfy the rising demand of decentralized electricity. When existing civil structures are used, only few new civil works are required, and the infrastructures costs are reduced. The additional advantages of mini hydropower plants are numerous and include grid stability, reduced land requirements, local and regional development and good opportunities for technologies export (Barelli et al., 2013).

Mini hydro technology is a reliable technology, with easy operation and with an estimated life cycle of more than fifty years. Mini hydro schemes can convert hydro power into electricity with a global efficiency of 60% to 90% (in comparison, despite the difference in the technology, solar cells convert about 10% to 12% of light energy directly to electric energy). Furthermore, mini and micro hydro plants reduce the emissions of CO_2, SO_x and NO_x, respectively, when compared with equivalent thermal power plants. When compared with diesel plants, a 2.5 kWh of energy through micro-hydro saves 1 litre of diesel (Laghari et al., 2013).

Figure 1.3 depicts the top six countries having the largest installed mini hydro capacity, among which also Italy is included (Laghari et al., 2013). China is the country with the highest installed capacity: it has 15 GW of electricity from mini hydro power plants and it will be able to install further 75 GW of mini hydro by 2020. China is followed by Japan (11%); USA, Italy and Brazil have got mini hydro capacity of 8%, 3% and 3% respectively. UK generates 100 MW from 120 sites. The Czech Republic, Romania, Poland, Turkey and Bulgaria have

established the target of more than 300 MW by 2015. Malaysia has got 18,500 MW of electricity from hydro power plants. In Canada, over 1600 potential sites are identified to be suitable for 100 kW micro-hydropower plants, while in Sri Lanka there is a mini hydro potential of 97.4 MW. Bangladesh has installed a micro hydro plant of 10 kW thank to private efforts, with the aim of illuminating 140 houses (Laghari et al. 2013). Therefore, mini/micro hydropower potential can be of interest worldwide.

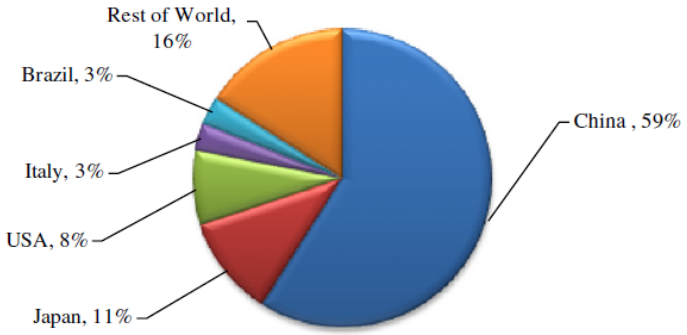

Fig. 1.3. World top six countries having largest installed mini hydro capacity (Laghari et al., 2013).

However, although the advantages are numerous, mini hydro is not fully exploited nowadays, especially because of the long delay in approval processes, institutional and environmental issues in getting approvals for implementation of new schemes. Administrative bureaucracy is one of the main obstacles in the deceleration of these schemes (Laghari et al. 2013).

1.2 Mini/micro hydropower turbines

1.2.1 Introduction

Generally speaking, hydraulic turbines are machines that convert the power of water into mechanical power at the shaft of the turbine. In order to choose the optimal turbine for a specific site, a careful analysis of the head and the available flow rate must be done (Barelli et al., 2013). Technical parameters (turbine type, turbine dimensions, annual energy production, maximum installation height in order to avoid cavitation), and economical parameters (machine cost, Net Present Value and Internal Rate of Return) have also to be taken into account to choose the proper design operating conditions (Santolin et al., 2011).

Hydraulic turbines can be classified into impulse turbines and reaction turbines. The rotor of reaction turbines is enclosed in a pressure casing, and fully immersed in water. The blades of the runner are designed to exploit the lift force due to pressure differences across them, and also the momentum of the water flow. The most used reaction turbines are *Kaplan* and *Francis* turbines. In the late Nineteenth and early Twentieth century, reaction turbines started also to be employed as micro/mini hydropower converters in sites below 2.5 m. A particular kind of reaction turbine used in very low head sites (head less than 2.5 m, Bozhinova et al., 2013) is the gravity turbine. The blades of gravity turbines exploit the hydrostatic force of water, so that the water weight is the main force that drives the turbine. Although the blades are immersed in water and a pressure difference is generated across them, a gravity turbine operates at atmospheric pressure. Water wheels and Archimedes screws are the most used gravity turbines.

On the other side, the blades of impulse turbines operate in air at atmospheric pressure. A water jet moves along the rotor blade without pressure differences across it, but with a changing in momentum. The most diffused impulse turbines are *Pelton*, *Turgo*, and *Crossflow* (or *Banki*) turbines, but their performance is poor at very low heads.

Figure 1.4 depicts the operational range of the described turbines.

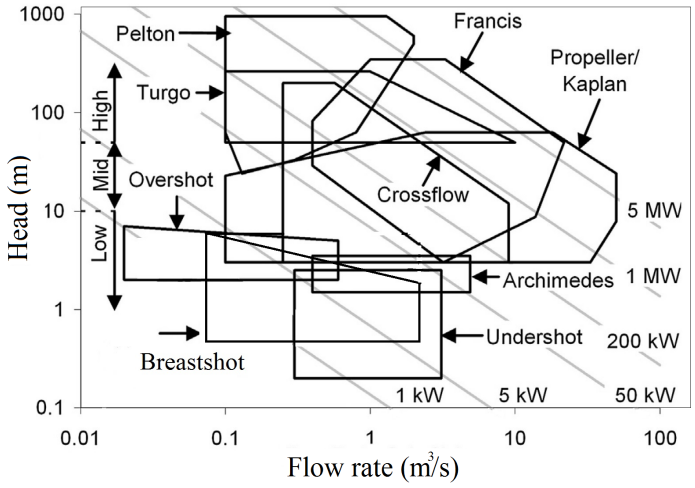

Fig. 1.4. Working conditions of some hydropower converters (Williamson et al., 2014).

In the last decades, hydrokinetic turbines were introduced (Vermaak et al., 2014). They exploit the kinetic energy of flowing water; some of these turbines can be completely immersed in flowing water. Hydrokinetic turbines can be classified into action turbines or reaction ones, depending whether the blades are

moved by the drag or by the lift force generated by the flowing water, respectively.

1.2.2 Description

In the next paragraphs, reaction, hydrokinetic and gravity turbines will be briefly discussed considering their applications in the micro hydro field, focusing especially on low head sites (less than 2.5 m). Then, in chapter 2 gravity water wheels will be described, being them the topic of this thesis.

Francis turbines were introduced for head differences from 0.75 m upwards. For head differences between 0.75 m and 5.0 m, these turbines were built in open top arrangements and with a vertical shaft. The efficiency ranged between 75% and 85%. Also *Kaplan* turbines were built from the late 1920s onwards for low head applications (from 1.8 to 5.0 m head difference). In order to operate at the optimum efficiency, the turbine systems require an inflow structure, minimizing the inflow losses. An outflow suction tube (the draft tube) decreases the flow velocity and thereby recovers pressure head. The maximum efficiency is 92%. Compared to *Francis* turbines, *Kaplan* turbines exhibit a slightly higher peak efficiency and the efficiency is constant over a wider range of flow rates, due to the adjustable pitch of the blades (Bozhinova et al., 2013).

The very low head (VLH) turbine is a new kind of reaction turbine, introduced recently, combining the regulated propeller turbine with an in-built generator inside a movable housing and a trash removal screen (Fig.1.5). This turbine was conceived for flow rates of 10-30 m^3/s and head differences between 1.4 and 3.2 m; hence it has to be classified as mini hydropower turbine. The diameter generally is 3.15-5.0 m. The efficiency can reach approximately 80% (Bozhinova et al., 2013).

However, the previous reaction turbines exhibit some drawbacks, in particular the significant environmental impacts, especially on fish safety, and the large investment costs, since important civil works are generally needed.

Therefore, in the micro hydropower field, *hydrokinetic* turbines and *gravity* turbines have been spreading (Bozhinova et al., 2013). A review on hydrokinetic turbines is reported in Vermaak et al. (2014). One example is represented by the hydrokinetic water wheel with horizontal axis, also known as stream water wheel (Fig.1.6). This wheel rotates around an horizontal axle, which is over the water surface. The stream exchanges its momentum with the wheel impacting on the blades immersed in water, and only the kinetic energy of water is exploited (also the vertical axis water wheel exploits the velocity of the water jet - converting the

Fig. 1.5. The very low head turbine (Bozhinova et al., 2013).

whole hydraulic head into flow velocity - , but this should be considered an action turbine). Water wheels will be better described in chapter 2.

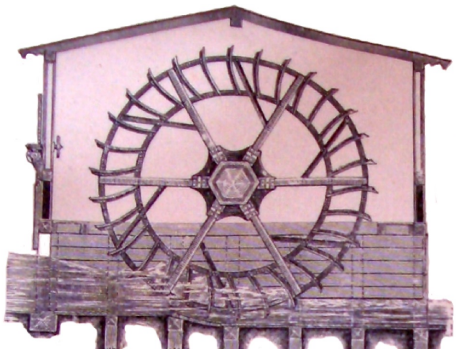

Fig. 1.6. Stream water wheel in shallow water (Brockhaus, 1903).

It is curious also to cite the gravitational vortex converter (GVC). It consists of an inflow, a circular chamber with a central outflow and a simple vertical axis turbine (Fig.1.7). The kinetic energy of the vortex flow drives the turbine. This turbine can be employed at head differences between 0.5 and 2.5 m, and flow rates between 0.5 and 20.0 m^3/s, although at the moment real installations use few cubic meter per second of flow rate. The maximum hydraulic efficiency is declared, from the companies that sell it, to be 79%, although experimental tests show maximum hydraulic efficiency of 40%(Bozhinova et al., 2013).

Instead, gravity machines exploit also the water weight, and they are installed in flowing water where there is also present an hydraulic head (i.e. the free surface of water upstream is higher than the downstream one), generated by a channel drop (geometric head). Among gravity hydropower converters, the oldest ones are the gravity water wheels. Gravity wheels spread after Smeaton's experiments

Fig. 1.7. The gravitational vortex converter (Bozhinova et al., 2013).

in the Eighteenth century (see section 2.3), who found the higher efficiency of gravity water wheels with respect to stream water wheels. The water weight in the buckets between two blades exerts an hydrostatic force on the blades. The maximum efficiency of gravity wheels can reach 90%. Undershot water wheels are generally used for head lower than 1.5 m, and the flow enters into the buckets significantly below the rotation axle. Breastshot water wheels are generally used with head up to 4 m, and the water enters into the buckets near the rotation axle. Overshot water wheels, used up to 10 m of head and for few hundreds l/s of flow rate, receive water at the top. These gravity water wheels will be deeply described in chapter 2.

The *Archimedes* screw is an other gravity machine. It was employed in the past as a pump, and only in the last two decades it has been introduced as turbine (Fig.1.8). The screw rotates around a rotation axle inclined at $22° - 35°$ from the horizontal. The hydrostatic pressure that makes the screw rotate is generated by the water in the buckets, which are delimited by the helical screw installed around the internal tubular structure. The diameters of Archimedes screws range from 0.6 to 4 m. They can be applied for head differences up to 8 m, flow rates from up to 8.0 m^3/s, with maximum hydraulic efficiency of 85-90% (Lubitz et al., 2014; Waters and Aggidis, 2015).

In addition to these already known machines, a new attention is also being given to new gravity machines. For example, *Aqualienne* and *Staudruck* machines are relatively new gravity machines, since they were patented in 2001 and 2004 in France and Austria, respectively. The cells of both the wheels are completely filled during operation, maximising the discharging capacity of the wheel. *Aqualienne* (Fig.1.9) is designed with a shroud structure to guide the flow and is suitable for head differences between 1 to 5 m, and the efficiency is approximately 80%. The *Staudruck* machine is claimed to be suitable for head differences from 1 to 3 m

Fig. 1.8. Archimedes screw used as turbine. Three installations in parallel (picture of Quaranta, 2016).

(Fig.1.10). The blades are mounted diagonally around their circumference, which enter and exit the water continuously across the width of the wheel.

The Hydrostatic Pressure Machine (Fig.1.11) is the result of further optimization of the *Staudruck* machine, with the introduction of the bottom shroud for minimizing leakage losses and the removal of side disks to allow cells to be filled and vented from the sides of the cells. HPM is appropriate for head from 1 to 2.5 m, with maximum efficiency of 80% (Paudel, 2015; Senior, 2010). HPM creates a dam effect on the upstream river, since the hub diameter is equal to the head drop.

Fig. 1.9. The *Aqualienne* machine (Senior, 2009).

No detailed investigation of the performance and/or theoretical framework is currently available for the most of the just introduced machines, and some proposed machines are not cost effective. For example, standard turbines (such as *Kaplan* turbines) cannot be employed economically in very low head and discharge conditions, while the very Low Head Turbine is only economically appro-

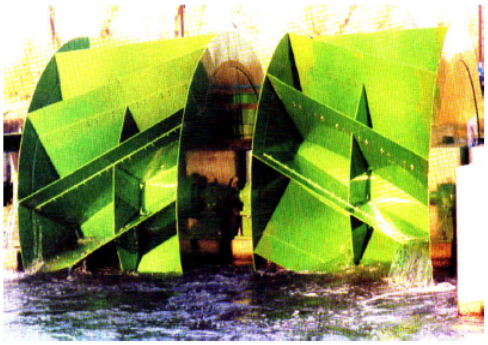

Fig. 1.10. The *Staudruck* machine (Senior, 2009).

Fig. 1.11. The Hydrostatic Pressure Machine (Bozhinova et al., 2012).

priate for power output bigger than 100 kW. The gravity machines that create a dam effect may generate problems upstream (the rising of the water levels) and with migratory fish. As a consequence, most low head and low discharge sites are currently not exploited. Therefore, considering the high potential of micro hydropower, especially in Europe, there exists the need of a cost-effective low head hydropower converter. Gravity water wheels can represent an attractive solution to this problem, and for this motivation this thesis will focus on them (Bozhinova et al., 2013; Müller and Kauppert, 2004).

Chapter 2

Water wheels: classification and literature review

In the previous section a brief review of micro hydropower machines was reported in order to illustrate how water wheels fit into this field. As previously said, gravity water wheels can represent an attractive solution in the micro hydropower field (Bozhinova et al., 2013; Müller and Kauppert, 2004).

The scope of the present chapter is to give an overview of different kinds of water wheels and their geometric characteristics. Some general information on their efficiency will be also reported, but the detailed performance characteristics of the wheels will be discussed in the next chapters.

2.1 Water wheels classification

Water wheels can be divided into horizontal axle and vertical axle water wheels, also called vertical and horizontal wheels, respectively.

Horizontal wheels have a vertical rotational axis, and they are impulse turbines. The water flows on the paddles of the water wheel, causing its rotation around the vertical axle. Horizontal water wheels are generally smaller than vertical wheels, thus they usually transfer the torque without using gearing mechanisms, due to their higher rotational speed. When installed in water mills, the axle of the water wheel acts as spindle of the mill. The mechanical effect of these wheels is determined in according to the theory of the impact of water. If the blades are flat, the efficiency is generally around 30%, because only the impact of water is employed. These wheels are generally constituted of 16 to 20 blades,

inclined at $50°$ to $70°$ relative to the horizontal. They are employed for falls from 3 to 6 meters, when a high rotational speed is desired, and when simplicity of construction is more important than efficiency. The diameters range between 0.9 to 1.5 m (Weisbach, 1849). Wheels of this form were diffused in all mountainous countries of Europe, and in north of Africa, used as mills for grinding grain. When the blades are designed with a greater length and a good curved shape, the water jet undergoes a changing in momentum and, therefore, the efficiency of the wheel becomes greater than in the impact type (Weisbach, 1849, Fig.2.1).

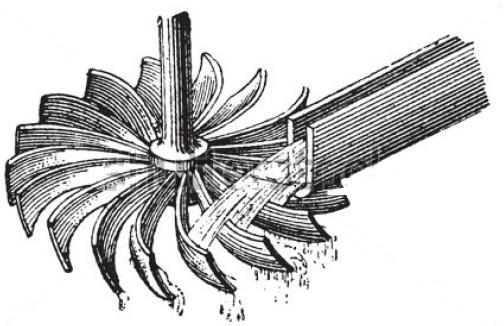

Fig. 2.1. Vertical axis water wheel.

Vertical wheels have an horizontal axle and they can be classified as either *stream wheels* and *gravity wheels*. Gravity wheels are potential energy converter, whereas stream wheels are kinetic energy converters.

Stream wheels are hydrokinetic machines, where change of head at the wheel location is negligible and the torque is provided by the momentum of the water stream. They are used in sites with very low heads or in flowing water, and the kinetic energy of water is exploited (e.g. Müller et al., 2007). Recent studies have introduced considerable improvements, employing also the hydrostatic force of water (Gotoh et al., 2001). A stream water wheel is depicted in Fig.2.3.

Gravity wheels are used in sites with higher heads, as the water weight is employed for producing energy. Therefore, gravity water wheels exploit mainly the potential energy of water and a portion of the kinetic energy. Three main types of gravity water wheels can be identified (e.g. Müller and Kauppert, 2004; Senior, 2009): *overshot*, *breastshot* and *undershot* water wheels. Breastshot water wheels can be divided in *high*, *middle* and *low*, depending whether the water entry point to the wheel is over the rotation axle (approximately in the uppermost third of the wheel, and these wheels can also be called pitch back water wheels), near the axle (approximately in the middle third of the wheel) or under the axle (also called undershot water wheels), thus approximately in the lowest third of the wheel, respectively. High breastshot wheels are also called pitch back water

wheels. Sketches of these water wheels are depicted in Fig.2.2 (Vidali et al. 2015; Quaranta and Revelli, 2015a).

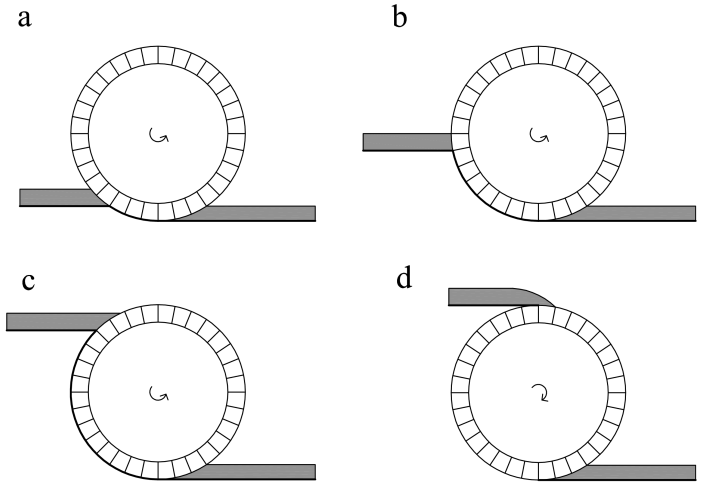

Fig. 2.2. Types of gravity water wheels: low breastshot/undershot (a), middle breastshot (b), high breastshot (c) and overshot (d). Undershot water wheels with no channel bed drops are stream water wheels.

In overshot wheels (Quaranta and Revelli, 2015b) the water enters into the wheel from the top, and in breastshot water wheels the flow fills the buckets entering from the upstream side of the wheel. Breastshot wheels rotate in the opposite direction with respect to overshot wheels (Quaranta and Revelli, 2015a). An overshot water wheel is depicted in Fig.2.12, while a breastshot water wheel is depicted in Fig.2.10. In breastshot water wheels the water can enter into the wheel as a free stream, without upstream inflow structures. The inflow is often regulated using overflow weir (*slow* breastshot wheels) or sluice gate (*fast* breastshot wheels), in order to regulate the upstream water depth and the flow velocity to the wheel (Garuffa, 1897; Quaranta and Revelli, 2016a).

Table 2.1 reports the heads and flow capacities per meter width of the traditional water wheels. Undershot and breastshot water wheels are suitable at high water volumes but low heads, while overshot wheels at high heads and low water volumes. The inflow quantity also depends on the width of the wheel. When compared to Archimedes screws, water wheels are more suitable in sites of high heads (higher than 3 m) and low flow rates (few hundreds of liters for second), or low heads (less than 1 m) and high discharges (few cubic meters for seconds). Archimedes screw should be preferred in sites with heads higher than 3 m and high flow rates, such as some cubic meter for second, because a water wheel would be too large.

Table 2.1. Water wheel operational ranges (Müller and Kauppert 2004)

Type	Head, m	Flow, $\frac{m^3}{s \cdot m}$
Undershot	0.5-1.5	0.5-1.2
Breastshot	1.5-4	0.35-0.65
Overshot	2.5-10	0.1-0.2

2.2 Advantages and drawbacks of water wheels

The advantages of gravity water wheels over common low head turbines are numerous: fast payback periods, simplicity of construction and good efficiency, lending themselves also to the developing world for local fabrication and maintenance, and to rural areas.

The total cost of a water wheel depends on its dimensions and geometry. In Germany, overshot water wheels are currently built (including installation and grid connection) for 3900÷4340 €/kW. Undershot wheels cost 6900÷8670 €/kW, Archimedes screws approximately 7380÷7804 €/kW of installed capacity. For comparison, low head Kaplan turbines cost 13000÷13900 €/kW (Müller et al., 2002). Water wheels cost is between 30% and 66% of Kaplan turbines (Müller and Kauppert, 2002). Payback periods can be estimated as 14.4÷15.4 for Archimedes screws, 7.5÷8.5 years for an overshot and 12÷17 years for an undershot wheel, (with expected life time of 30 years), which are very low if compared to Kaplan turbine installations for the same head, where payback periods of $25 \div 30$ years can be expected (Müller and Kauppert 2001; Müller and Kauppert 2004). If water wheels are well designed, they can reach an hydraulic efficiency of $75 \div 90\%$, depending on the type of water wheel (as found in this thesis). The efficiency can be maintained optimal over a wide range of external conditions.

Concerning with stream water wheels, the payback periods are generally more variable, in function of the hydraulic conditions and geometric dimensions. The payback period has been estimated in about 20 years for a floating stream wheel (Handler and Broeckel, 2011), while in Akinyemi and Liu (2015) the assumed payback period of an hydropower system with six stream wheels is calculated about 4 and 5 years (Akinyemi and Liu, 2015). Water wheels can therefore constitute an economically interesting investment also in industrialized countries.

Water wheels also fit well into the ecosystems (fish are able to pass through water wheels unharmed, hence expensive fish screens are not necessary), thus they are considered not out of place when installed along a river (Quaranta and Müller,

2017). They can be built using existing civil structures, for instance rehabilitating the old water mills into micro hydro plants (contributing to the development of eco-tourism, valorization of the cultural heritage and promotion of social activities). In developing countries the total installation costs can be minimized by using indigenous expertise and technology (Paish, 2002).

The drawback of water wheels is that, turning at slow rotational speeds (≤ 20 rpm), they need of high ratio gearboxes for generating alternate electricity. Some water wheels may produce a "low frequency thumping noise", which anyway can be reduced by an accurate design of the blades (Quaranta and Müller, 2017). Hence the employment of classical water wheels for the generation of renewable energy from water is becoming a cost-effective and sustainable solution in the micro hydropower field, where hydraulic heads of a pair of meters and few cubic meters for second of flow rate are available.

The scientific community spent a lot of efforts on water wheels especially during the Eighteenth and Nineteenth century. Some experimental tests and theoretical estimations for the determination of the efficiency of water wheels were developed, but they generally were not totally satisfactory. Indeed, theoretical analyses were not supported by experimental tests, and comparisons of different geometric configurations and types of water wheels under the same hydraulic conditions were generally not presented. However, few research has been carried out on water wheels nowadays. Therefore, the most of the available engineering and scientific information is ancient, with uncertainty and often published in not well known text-books. This lack of knowledge is a significant drawback of water wheels.

Therefore, the filling of this gap will be the aim of the present thesis. This was achieved firstly by analyzing the historic literature, and by experimental tests. Then, theoretical and numerical models were developed and validated using experimental results, with the aim of estimate and improve the efficiency of water wheels.

2.3 Brief scientific history of water wheels

Water wheels were introduced more than two thousands of years ago; they were used for producing energy, grinding grain, forging iron, pumping water, sawing wood and stones, for metalworking and leather tanning.

The oldest documented water wheel had a vertical axle, while the first kind with an horizontal axle was the *stream* water wheel, which was described by Vit-

ruvius in 27 BC. Stream water wheels have been later analyzed by many engineers and scientists, including Parent, de Borda and Smeaton (Senior, 2009; Capecchi, 2013). From the 18th Century onwards, stream wheels were frequently employed in order to generate mechanical energy. They were considered cost effective since little civil engineering work was required.

In 1704 Antoine Parent published his theory on jets and calculated the efficiency of stream wheels, assuming that: (a) the force exerted by the water flow on a blade is proportional to the square of the relative velocity between the blade and the water $(v-u)^2$, where v and u are the blade and stream velocity, respectively; (b) friction is negligible and a steady state is reached. There were also two further fundamental assumptions not made explicit: (c) only one blade at a time is immersed in water; (d) the stream is perpendicular to the blade. With these assumptions, the maximum efficiency should be $\eta = 8/27$ for $u/v = 1/3$, but Parent limited the hydraulic efficiency of stream water wheels to just 4/27.

In 1767, de Borda published his theory and corrected Parent's analysis. He observed that the action of water is not exerted against an isolated blade, but against several blades simultaneously; the blades also close all the breading of the canal and remove from the fluid all the velocity that it has more than the blades. Therefore, the shock experienced by a paddle is no longer proportional to the square of the difference between fluid and paddles velocity, but to the difference in the speed; hence the effect is represented by $v(v–u)$, and not by $(v–u)^2$ as supposed by Parent. The maximum efficiency is now $\eta = 1/2$, when $u/v = 1/2$. However, there are not theoretical evidences justifying the fact that when there are several blades immersed in water the force of impact should vary as $v(v–u)$ instead of $(v–u)^2$. De Borda had good reasons to accept his theory, as it was in good agreement with experience.

John Smeaton published then experimental data which demonstrated a maximum efficiency for stream water wheels of $\eta = 1/3$, greater than that provided by Parent ($\eta = 4/27$) but lower than that provided by de Borda ($\eta = 1/2$) (Capecchi, 2013). In 1759 John Smeaton published experimental data on gravity wheels (Capecchi, 2013), demonstrating the higher efficiency of *gravity* wheels over the efficiency of impulse stream wheels.

Therefore, in order to link the higher efficiency of gravity wheels with the simplicity of hydrokinetic wheels (stream wheels), in the early 19th century, the French engineer J. V. Poncelet performed a new blade design for the stream water wheels, increasing the maximum efficiency from $\simeq 30\%$ to $\simeq 65\%$. The blades of the *Poncelet* wheel were shaped in order to avoid power losses during the impact; the blades were curved in order that the water could flow from the tip of the blade toward the root, pushing against the blades also by its weight. This design was

the first effective improvement of the original stream water wheel, and is further discussed in section 2.6.

In the Eighteenth and Nineteenth century, additional theories were developed and experimental tests on water wheels were conducted (Poncelet, 1843; Morin and Morris, 1843; Weisbach, 1849; Bach, 1886; Chaudy, 1896; Garuffa, 1897; Church, 1914) and their use spread considerably. By 1820 France had 60,000 water wheels (Denny, 2003), by 1850 England had 25-30,000 water wheels, and as late as 1925 Germany had 33,500 water wheels (Müller and Kauppert, 2004). However, theories were generally developed separately from experimental tests, and they were usually not validated. Several prescriptions on water wheels design were empirical, and not based on scientific evidence. Furthermore, the experimental tests were carried out more than one century ago, with several uncertainty.

At the end of the Nineteenth century, the rising demand of energy, the rapid improvement in the engineering knowledge (especially the design of big hydroelectric plants) and the economic development led to the diffusion of modern turbines (*Pelton*, *Francis* and *Kaplan* turbines and big hydroelectric plants). Therefore, the water wheels used in low head sites especially for self sustainment were replaced and by then considered bygone and ancient hydraulic machines. Nowadays, due to the new interest in mini hydropower as described before, the scientific research on water wheels is experiencing a revival and there are now some companies which are specialized in the manufacture of water wheels (Müller and Kauppert, 2004). In the next sections a literature review on vertical water wheels will be presented.

2.4 Stream water wheels

The stream wheel was the first vertical type of wheel used in the past, because of its simplicity; it is installed in flowing water and high flow rates are requested to generate appreciable power output. In this section the general characteristics of these machines are described.

In Müller et al. (2007) three kinds of stream wheels were identified and described: stream wheels in subcritical and shallow water, stream wheels in supercritical and shallow water and stream wheels in deep water. In the cited work it has been highlighted that each type interacts with the stream in a different way, thus it is essential to distinguish between them, as it was not considered by Parent, de Borda and Smeaton.

In shallow flow the water depth of the stream is comparable with the blade height. A shallow flow can be subcritical, when the free surface depth is over the

critical depth, or supercritical, when the free surface depth is under the critical depth. Stream wheels in shallow water are confined wheels, due to the fact that they exploit all the depth and width of the stream. For water wheels in shallow water, a curved shroud on the bed of the channel (under the wheel) is suggested for improving the efficiency and for reducing the leakage volumetric losses. If a wheel is positioned very close to the base of the river's bed, and it is nearly as wide as the channel, then the power output and efficiency will increase as the flow is forced through a small space at high velocity. However, since the high flow velocity and power losses during the impact on the blades, the maximum efficiency is lower than the maximum efficiency of gravity wheels. An early investigation into this phenomenon was the Cairo University based paper (Bagdhadi and Mikhail, 1985). The paper estimated that efficiencies of up to 63% were possible with this design.

2.4.1 Historical literature

2.4.1.1 Stream wheels in deep flow

The most ancient kind of stream wheel is that in deep water, generally called floating mill. Floating mills were first recorded in Rome in 540 AD when Belisarius had them operating during Vitibes's siege of Rome. They usually consisted of a mill boat, which contains the mill's machinery, and a water wheel which was usually supported by the boat on one side, and a float on the other side. Sometimes, floating mills were built with two symmetrical floating bodies, often with conically bows to guide the water into the wheel, or with a central boat and two wheels on each side (Müller et al., 2010).

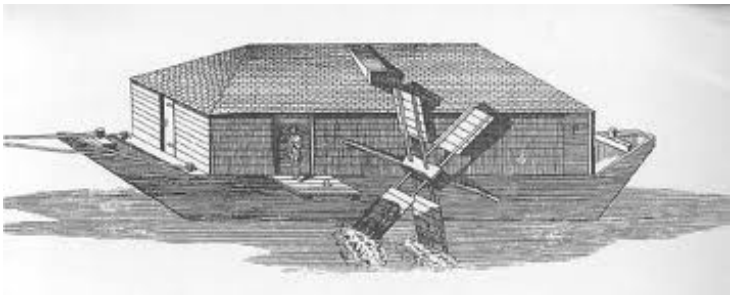

Fig. 2.3. Image of a floating mill (Müller et al., 2010).

Floating water wheels represent a simple technology for decentralized power generation in large rivers, for example in developing countries (Müller et al., 2010). They are of simpler construction (little civil engineering work is required), their installation costs are lower and their cultural and aesthetic value is higher

with respect to other kinetic devices. Although the efficiency of the early stream wheels ranged between 25% to 50%, modern tests show that their current geometric designs can reach maximum efficiency higher than 70% (Müller et al., 2010; Batten and Müller, 2011).

Floating mills have diameters approximately of 4 to 5 m, with 10-12 blades slightly inclined forward (about $10^\circ \div 20^\circ$, Weisbach 1849). Bach (1886) and Busquet (1906) suggest to use $18 \div 24$ blades, while Chaudy (1896) suggests 6 to 10 blades.

The drawback of floating mills is that the wheel is fixed to a barge or catamaran, hence a build up of river bed or a reduction in the water level could lead to the blades becoming damaged hitting the river's bed.

2.4.1.2 Stream wheels in shallow flow

One example of stream water wheel in shallow water is shown in Fig.1.6. The water flows with a velocity greater than the peripheral velocity of the wheel, and impacts on the wheel, leaving it with the same velocity of the blades. In order to generate power, a high flow velocity is thus required. The optimal ratio u/v between the tangential speed of the wheel u and the absolute flow velocity v is suggested as 0.4, both in shallow and in deep water. These information are confirmed both in historic books (Weisbach, 1849; Bresse, 1869; Bach, 1886; Busquet, 1906) and in modern times (the British Hydropower Association suggests $u/v = 9/20$).

Stream wheels in shallow water are generally constructed with diameters between 4 to 8 m, with 24 to 48 blades. The straight blades are constructed in radial direction, or with a slight forward inclination, in order to reduce the inflow power losses (as in Fig.1.6). The height of the blades is generally 1/5 of the radius of the wheel; at least one blade should be always immersed in water, while Weisbach (1849) suggests an optimal number of immersed blades of three.

2.4.2 Modern literature

2.4.2.1 Stream wheels in shallow flow

In Müller et al. (2007) two different theoretical models have been reported for estimating the performance of stream water wheels in shallow water, the former for subcritical flow and the second for supercritical flow. In the theoretical models, the following hypothesis have been assumed: (1) the behavior is one-dimensional

and a steady state is considered; (2) one blade only interacts with the stream; (3) the blade is perpendicular to the stream velocity. In subcritical flows, the maximum experimental hydraulic efficiencies are generally lower than 30%, and the theoretical model shows maximum efficiency of 29.6%. In supercritical flows, the maximum efficiencies are generally lower than 40%; physical model tests indicate that a 22.5 degree forward inclination of the blades gives the maximum power output.

In Gotoh et al. (2001) detailed experimental tests on the performance of stream wheels in shallow subcritical water have been performed. The damming effect discovered in these tests due to the presence of the wheel was later used in the Rotary Hydrostatic Pressure Machine (Senior et al., 2010), where the hydrostatic force of water is exploited for the production of energy, although no geometric head (difference in the channel bed elevation upstream and downstream) is available. The maximum efficiency was 80%. In Paudel et al. (2013) the effect of channel width on a water wheel with flexible rubber blades has been investigated. The results show significant improvement in the water wheel performance (from 50% to 70%) by reducing the channel width, and adopting the diverged channel shape on the downstream side. In Tevata and Chainarong (2011) and in Luther et al. (2013) the effect of the blades number has been investigated, illustrating that an optimum blades number exists and that curved blades perform better than flat ones.

2.4.2.2 Stream wheels in deep flow

In deep flow, the water depth is significantly higher than blades dimensions.In Müller et al. (2007) a simple theoretical equation is reported for calculating the power output of a deep water stream wheel, with maximum efficiencies generally lower than 50%.

In Müller et al. (2010) a stream water wheel in deep water using different numbers of blades has been investigated. A maximum efficiency of $\eta = 0.42$ for 24 blades has been achieved and, if any kind of mechanical loss would be negligible (such as friction and leakage losses), probably the maximum efficiency would be $\eta = 0.5$ for $u/v = 0.5$, as suggested theoretically by de Borda. Instead, for 8 and 12 blades, the maximum experimental efficiency was $\eta = 0.25$ and $\eta = 0.35$, respectively. The maximum efficiency velocity ratio was $u/v = 0.4 \div 0.55$. In Müller et al. (2010) and Batten and Müller (2011) the confinement effects of stream wheels in deep water have been investigated. The experimental efficiency improved from $\eta = 0.25 - 0.42$ (Müller et al., 2010) to a maximum of about $\eta = 0.8$. The beneficial effect of the confinement has also been demonstrated

numerically in Akinyemi and Liu (2015), using a plate under the wheel.

2.5 Undershot water wheels

Undershot water wheels are used for very low heads, typically less than 1.5 m. Four significant types can be identified: undershot wheels with straight radial blades, *Sagebien* and *Zuppinger* water wheels, and *Poncelet* wheels. Radial blade, *Sagebien* and *Zuppinger* water wheels are used in sites where channel drop are present (geometric head) and they are potential energy converters. The radial blade wheel is the simplest and least efficient type. *Sagebien* and *Zuppinger* wheels are conceived to minimize the upstream or the downstream power losses, respectively. Instead, *Poncelet* wheels are generally used in straight channels, with an upstream sluice gate in order to increase the water level upstream and the water velocity to the wheel. Since the water jet which is generated flows along the curved blade, also the water weight is employed. Examples of these wheels are reported in Fig.2.5 for *Sagebien* wheels, in Fig.2.6 for *Zuppinger* and in Fig.2.8 for *Poncelet* wheels. Practically, *Sagebien* wheels are radial blade undershot wheels but with the blades inclined forward.

2.5.1 Historical literature

2.5.1.1 Undershot water wheels with radial blades

In the historic literature some geometric prescriptions can be found for radial blades water wheels. For example, in Weisbach (1849) the diameter D of a generic undershot water wheel with straight blades is suggested to be calculated by (1) $D = (H - h_2)/(1 - \cos\alpha)$, where H is the head difference, $h_2 = 4.4v^2/2g$ (v is the absolute flow velocity and $g = 9.8$ m/s^2) and $\sin\alpha = \sqrt{\frac{h_2 - h_d}{h_2}}$, with h_d the tailrace water depth. Weisbach suggests to calculate the number of blades n or the peripheral distance between two blades l by the following formulations: (2a) n=18+9.8*R or (2b) l= 7(1+4d), with the bucket depth d and the radius of the wheel R in meters, with a general suggestion of (3) l=0.25÷0.37 m and $d = 0.37 \div 0.45$ m. The bucket depth is defined as the distance between the root and the tip of the blade. Pacinotti (1851) suggests to use (4) $n = 12R$, with radius generally between 2.5 to 3.5 m (30÷42 blades); Bresse (1869) considers diameters of 3÷5 m and (5) $l = 0.35 \div 0.4$ m (thus approximately 36 blades), with $u/v = 0.4$. Cadolini (1835) proposes diameters of 4÷8 m and (6) $l = 0.28 \div 0.45$ m (hence 45÷56 blades) (Fig. 2.4).

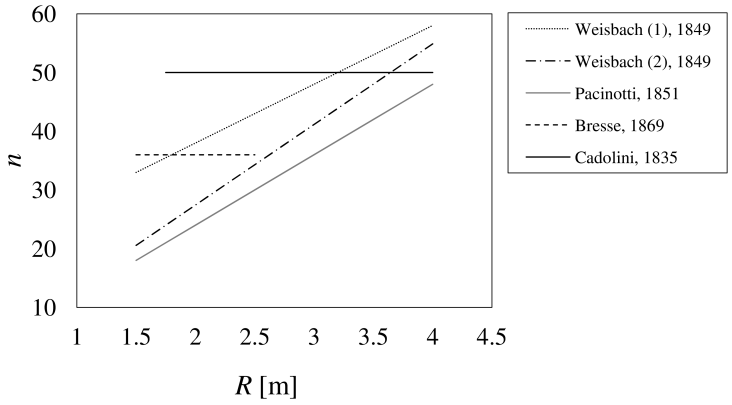

Fig. 2.4. The number of blades proposed by *Weisbach* (1849), *Pacinotti* (1851), *Bresse* (1869) and *Cadolini* (1835) as a function of the wheel radius. Except for *Cadolini* and *Bresse*, the proposed number of blades increases with the wheel dimensions.

2.5.1.2 Special undershot water wheels: Sagebien and Zuppinger wheels

As previously said, among gravity undershot wheels, it is possible to distinguish *Sagebien* wheels (represented in Fig.2.5) and *Zuppinger* wheels (in Fig. 2.6).

The *Sagebien* wheel was developed by Alphonse Sagebien, a French engineer, in 1858, and designed for minimizing the upstream power losses, when the water enters into the wheel. The *Zuppinger* undershot water wheel was developed by the Swiss hydraulic engineer Walter Zuppinger and patented in 1853; the blades were designed in order to minimize the power losses downstream of the wheel.

The *Sagebien* wheel had generally diameters from 7.5 to 10 m and 70 to 80 blades, although Busquet (1906) suggests a diameter of approximately 4 m and a peripheral distance between two blades of 0.35-0.4 m (thus about 32 blades). The tangential velocity was usually taken as 0.6 to 0.8 m/s, although in some cases up to 2 m/s. The rotational speed ranged from 1.5 to 2 rpm, and the flow volume per meter width from 1 to 1.2 m^3/s. The blades are inclined of $40° \div 45°$ to the upstream surface of water (Chaudy, 1896; Müller, 1899). In 1870, a total of 63 *Sagebien* wheels were installed in 15 Départements in France (Tresca, 1870). *Sagebien* wheels are currently diffused especially in France; they have generally diameters between 7.5 to 11 m, with 70 blades, that sometimes are reduced to a minimum of 32 (Marie-Paule Dupuy, Région Aquitaine - Limousin - Poitou-Charentes). Hydrowatt has employed these wheels for heads of $H = 1$ m, with a diameter of 6.5 m, a number of blades of 42 and rotational speed of 4.5 rpm.

Table 2.2 reports some example of existing *Sagebien* water wheels.

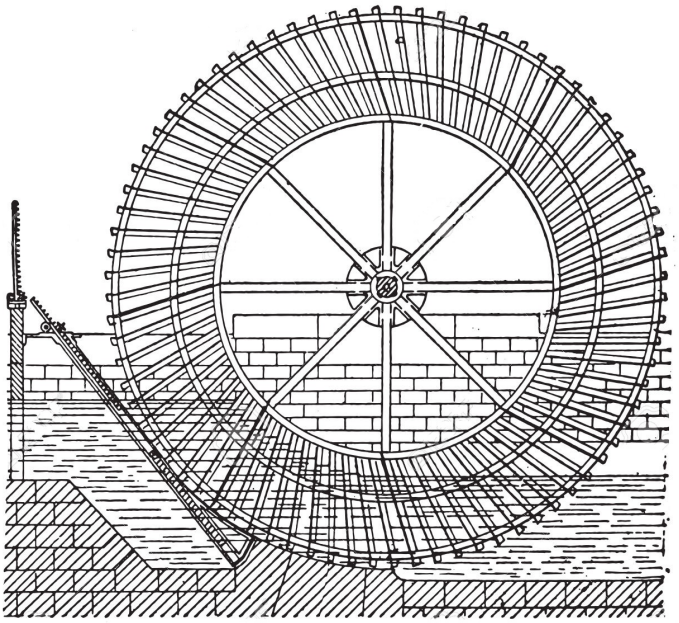

Fig. 2.5. An example of *Sagebien* water wheel (Industrial encyclopedia E.-O. Lami - 1875).

Table 2.2. Some characteristics of *Sagebien* water wheels in operation collected by Quaranta, E., with their exploited head H, flow rate Q, diameter D, width b, number of blades n, rotational speed N and electrical power P_{el}. Source: personal communications. Water wheel installed by: [1] German company, [2] French cooperative Condroz Energies Citoyennes, [3] Région Aquitaine Limousin Poitou-Charentes.

Company	H [m]	Q [$\frac{m^3}{s}$]	D [m]	b [m]	n –	N [rpm]	P_{el} [kW]
Hydrowatt (Germany) [1]	1		6.5	2.3	42	4.5	20
www.panoramio.com (France)	-	-	11	6	70	-	112.5
Les Avins Roue (France) [2]	-	-	9.2	-	70	-	13-18
Marie-Paule DUPUY (France) [3]	-	-	7.5	-	32-40	-	-
Marie-Paule DUPUY (France) [3]	-	-	7	3	56	-	-

Instead, there are two different types of *Zuppinger* wheels, with different inflow configurations depending on the range of head differences available. Wheels for head differences between approximately 1.2 and 2.5 m had a variable inflow

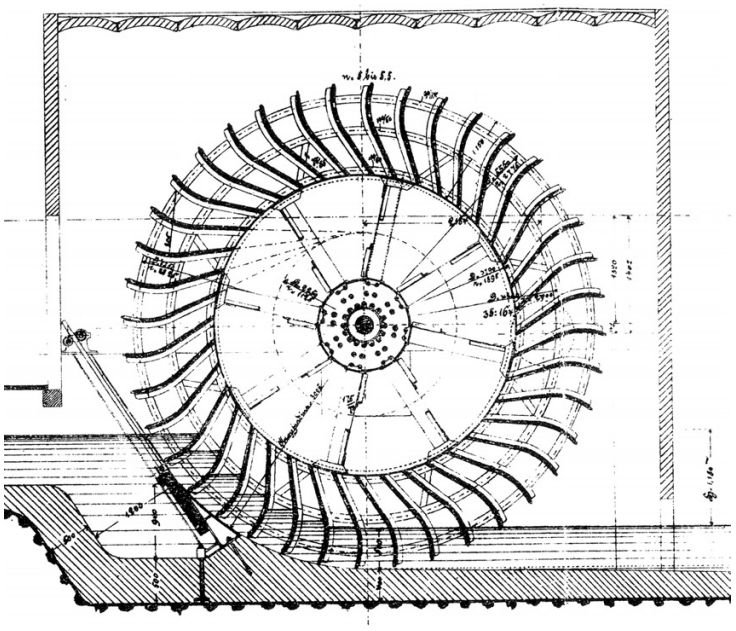

Fig. 2.6. An example of *Zuppinger* water wheel (Müller, 1899).

weir, to control the upstream water level independently of the flow volume, and therefore these wheels can work efficiently at constant rotational speed. Measurements at a full scale wheel indicated efficiencies of 72 to 75%, (Neumayer et al., 1979). This kind of wheel can be also classified as breastshot wheel, depending on the upstream water level. The *Zuppinger* low head wheels did not have an inflow weir and were employed for head differences from 0.4 m to 1.2 m. Low head *Zuppinger* water wheels had diameters of 6 to 7.5 m, 32 to 48 blades, a speed of rotation of 4-4.5 rpm and flow rates of up to 1.2 m^3/s per meter width. The efficiencies were reported as 70 to 75% (Müller, 1899). Modern tests show efficiency up to 85% for a wheel model of 1.8 m in diameter and head difference of 0.25 m (v. Harten et al., 2013).

The blades of *Zuppinger* wheels are shaped in order to minimize power losses at the exit, rather than the entry losses. Hence the blades profile at the exit should be normal to the downstream water surface, while the external edge of the blades is generally constructed in radial direction (e.g. Müller & Kauppert, 2004). As a consequence, the blades generally are almost parallel to the upstream water surface at the entry point, generating a slam effect, noise and power losses. Furthermore, there exists one example in the literature of a *Zuppinger* water wheel where the filling ratio (percentage of bucket volume filled with water) of the buckets is one, called *Zuppinger* turbine wheel. The water enters into the wheel laterally and exits underneath. Figure 2.7 shows a *Zuppinger* turbine wheel found in a German

encyclopedia from 1903. The upstream and downstream channel is wider than the wheel. This machine could operate from very low heads (1 m) up to possibly 10 m (Bozhinova et al., 2013). Preliminary tests conducted by Helmizar (2016) shows maximum hydraulic efficiency of 90%, but that is strongly affected by changes in flow rate and rotational speed.

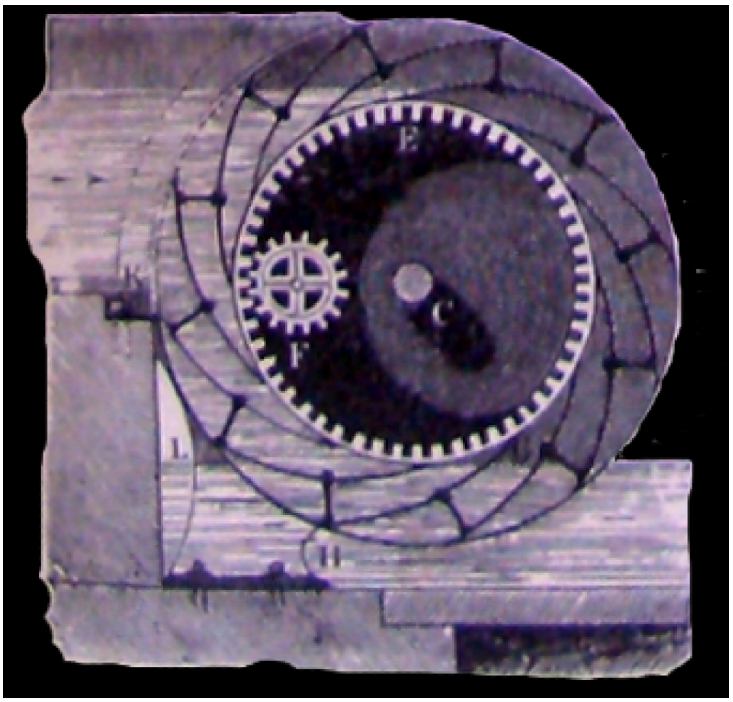

Fig. 2.7. An example of *Zuppinger* turbine water wheel (Bozhinova et al., 2013).

Nowadays, there exist some *Zuppinger* water wheels realized by the company Hydrowatt. These wheels are employed for heads H lower than 2 m, with diameters which range between $3H$ to $5H$, width between 1.2 to 4 m (depending on the flow rate). The number of blades ranges between 24 to 36 and rotational speeds between 4.5 to 6.5 rpm. Table 2.3 reports some examples of existing *Zuppinger* water wheels.

Table 2.3. Some characteristics of *Zuppinger* water wheels in operation collected by Quaranta, E., with their exploited head H, flow rate Q, diameter D, width b, number of blades n, rotational speed N and electrical power output P_{el}. Water wheels installed by: [1] German company.

Company	H [m]	Q [$\frac{m^3}{s}$]	D [m]	b [m]	n –	N [rpm]	P_{el} [kW]
Müller and Kauppert (2002)	1	-	6.5	2.3	-	-	0.7
Hydrowatt (Germany) [1]		1	6.5	1.2	36	4.5	12
Hydrowatt (Germany)	2		4.2	2.9	24	6.5	11
Hydrowatt (Germany)	1.1		5.5	4	30	5.5	26
Hydrowatt (Germany)		2	6	2	36	4.8	27
Hydrowatt (Germany)		1.5	4	2	-	-	12

2.5.2 Modern literature

Sagebien wheels are not known to have been investigated in the modern era, whereas measurements at a full scale *Zuppinger* wheel indicated efficiencies of 72 to 75% (Neumayer et al., 1979) and up to 85% for a wheel model of 1.8 m in diameter and head difference of 0.25 m (v. Harten et al., 2013). However, no detailed characteristic curves have been presented and compared with *Sagebien* ones. Therefore, in this thesis the performance of a *Sagebien* wheel will be investigated and compared with the performance of the *Zuppinger* one, testing in laboratory both of them (Quaranta and Müller, 2017).

2.6 *Poncelet* undershot water wheels

2.6.1 Historical literature

The *Poncelet* wheel was developed in France in the 1820s. It consists of a wheel with curved blades and an inflow with an undershot weir, or sluice gate. The fast water jet enters into the wheel and exchanges its impulse flowing along the blade and then falling out, performing additional work (thus also the water weight is used). This dynamic pressure, acting on the blades, drives the wheel. The blades are also designed so that the water then falls out of the cells easily and with a low horizontal velocity (Fig. 2.8).

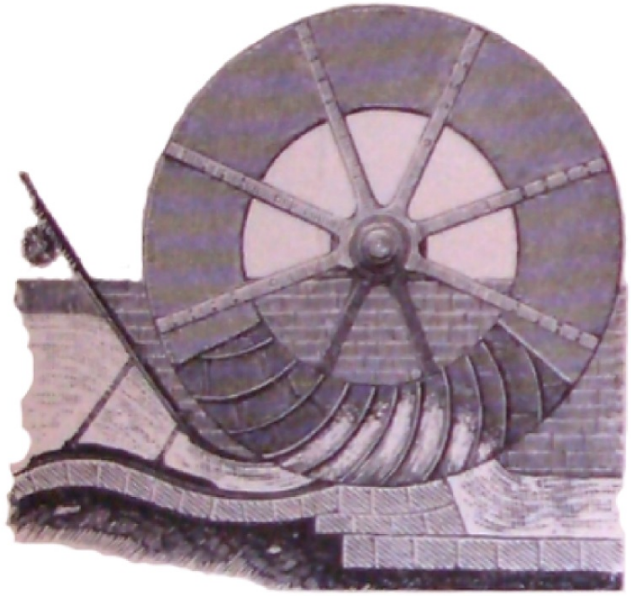

Fig. 2.8. An example of *Poncelet* water wheel (Brockhaus, 1903).

Theoretical analysis and experiments conducted by Poncelet showed efficiencies of 55–65%, whereby the efficiency reduces with increasing head difference. Head differences ranged from 0.75 to approximately 1.7 m, and efficiencies were assumed as 60–65% for $0.75 < H < 1.2$ m, and 55–60% for head differences between 1.2 and 1.7 m. A maximum mechanical efficiency of 60% is usually assumed (e.g. Müller 1899). Flow rates ranged from Q=0.3 to 1.5 m^3/s per meter width, with power outputs of $1 < P <$ 13.8 kW per meter width. Typical diameters were 3÷6 m and $u/v = 0.4 \div 0.5$ (Poncelet 1827; Weisbach 1883; Chaudy 1896).

Chaudy (1896) and Bresse (1869) suggested to adopt 36 blades for diameters of 3÷4 m, and 48 blades for diameters of 6÷7 m, while Church (1914) suggested a general number of 32÷48 blades. Weisbach (1849) and Busquet (1906) suggested a peripheral distance between two blades of l =0.20 m. Bach (1886) proposed the formula (1) $n = 12D$ with D in meters and Fairbairn (1864) proposed the equation (2) $n = 5.25D + 16$, with D in meters. The blade profile was suggested to be circular, except in Bresse (1869), who claimed that the curvature is a matter of indifference. Figure 5.5 depicts the blades numbers suggested by the previous authors as a function of the diameter.

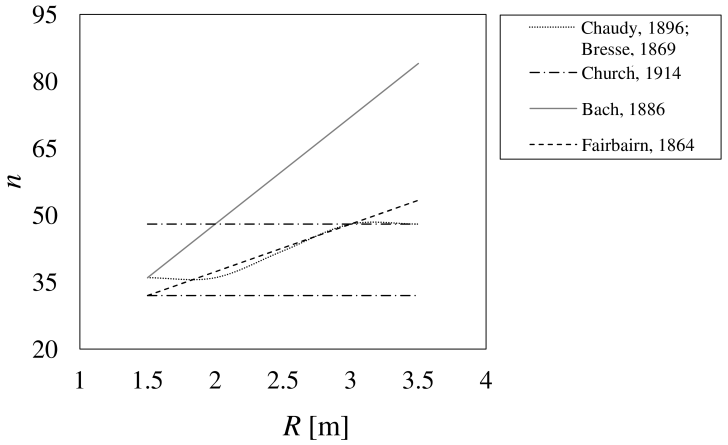

Fig. 2.9. The number of blades proposed by *Chaudy* (1896), *Bresse* (1869), *Church* (1914), *Bach* (1886) and *Fairbairn* (1864) as a function of the wheel radius. The number of blades increases with the radius of the wheel, while *Church* proposed an upper and lower limit.

2.6.2 Modern literature

In modern times, papers or reports speaking about the performance of *Poncelet* wheel have not been found. However, the company BEW Power is developing a similar design of the *Poncelet* wheel, called the *Lamella* turbine, which is constituted of two concentric stages of blades (http://www.bew-power.at).

2.7 Breastshot water wheels

As described before, there are three different kinds of breastshot water wheels: middle, low and high breastshot wheels. The middle and low breastshot water wheels have deeper buckets to deal with the higher volume of water generally available at low heads. Both the weight and impulse of the water are employed in their operation, and these water wheels are larger in diameter and wider than many other water wheels. The maximum efficiency are estimated to be 80% (Müller and Kauppert, 2004). A classical middle breastshot water wheel is represented in Fig.2.10.

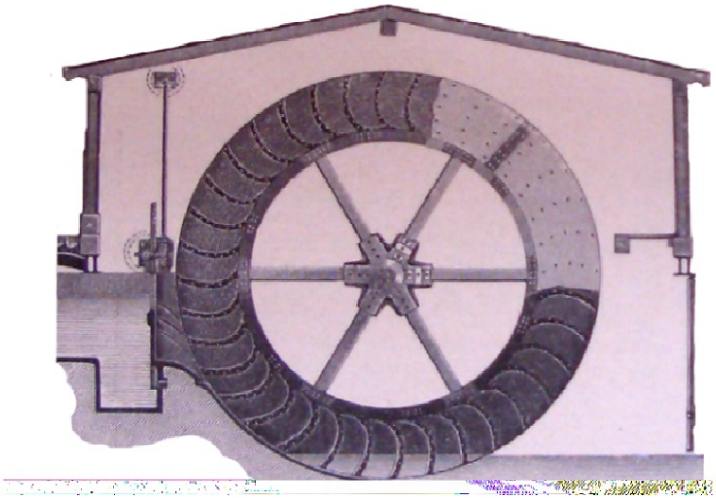

Fig. 2.10. An example of breastshot water wheel (Brockhaus, 1903).

2.7.1 Historic literature

Concerning with breastshot wheels, some design prescriptions can be found in literature. For example, the filling ratio of the buckets (water volume inside the bucket to the volume of the bucket) is well agreed in $1/3 \div 1/2$ and the tangential speed approximately one half of the absolute flow velocity, for all the kinds of breastshot wheels. The British Hydropower association recommends a rotational speed of (1) $21/D^{1/2}$ rpm, without considering the flow velocity and head (not very right considering the results of this thesis). Cullen (1871) reports a table, where the results can be summarized as optimal rotational speeds of (2) $8 \div 10.6$ rpm and diameters of $4.2 \div 5.7$ m with $30 \div 40$ blades, where the diameter can be expressed as (2) $D = 0.923H + 3.392$, where H is the hydraulic head difference.

High breastshot wheels have generally diameters of (1) $D = H + 1$ (Chaudy, 1896; Busquet, 1906), velocity ratio $u/v = 0.4 \div 0.6$ and filling ratio of $1/3 \div 1/2$.

Middle breastshot wheels have generally diameters D slightly higher than (1) $2H$, thus a radius slightly longer than the head H. Bresse (1869) suggests a diameter up to about 6 m, Bach (1886) a maximum of (2) $H + 3.5$ m, Garuffa (1897) (3) $D > 2H + 2$ m, Busquet (1906) (4) $R = D/2 = H + 0.57h_u + 2/3h_u$, with h_u the upstream water depth (over the channel bed), and Chaudy (1896) (5) $D = 3.5 \div 7$ m (Fig. 2.11).

If well designed, the blades are shaped so that an amount of kinetic energy of

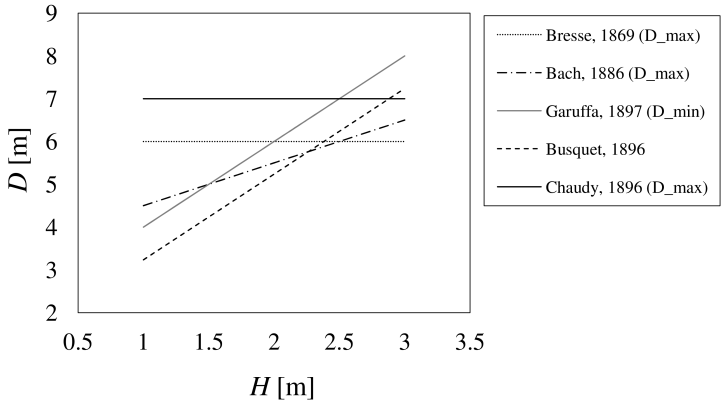

Fig. 2.11. The diameter proposed by *Bresse* (1869), *Bach* (1886), *Garuffa* (1897), *Busquet* (1906) and *Chaudy* (1896) as a function of the head H. A water depth $h = 0.5$ was adopted for *Busquet* formulation. *Bresse*, *Bach* and *Chaudy* proposed a maximum value, while *Garuffa* a minimum value.

the flow is also exploited, minimizing the entry power losses. The blades should also exit the water downstream at a right angle, to avoid losses. The cells are ventilated in order to let the air escape during inflow, and to let air into the cell when the cell starts to rise again above the lowest point. Bresse (1869) suggests a peripheral distance between two blades l of about $1.3 \div 1.5$ times the upstream water depth, while Garuffa (1897) and Chaudy (1896) $l = 0.4$ m. The depth of the cells (i.e. the length of the cell along the wheel radius) was recommended to be around (1) $d = (0.4 \div 0.5)(D/H)^{1/3}$ from Bach (1886) and (2) $d = (0.4 \div 0.5)(D/4)^{1/3}$ from Garuffa (1897).

Concerning with low breastshot wheels, Busquet (1906) suggests diameter of 3.6 to 7.2 m with a depth of the cells of $0.4 \div 1$ m, while Chaudy (1896) diameters of 6÷7 m and depth of 0.6÷0.7 m, when the inflow is realized by a sluice gate. Weisbach (1849) gives the same formula to calculate the diameter and blades number of undershot wheels, with a recommended depth of the buckets of 0.25÷0.37 m.

An example of a low breastshot wheel in operation is the wheel sited in Verolengo (Turin, Italy). It is 4 m in diameter, 1.3 m in width, 32 blades and it discharges the average flow rate of 0.55 m^3/s. The geometric head (the channel drop) is 0.7 m. This wheel is the power source of the mill where it is installed, and a scaled model will be investigated in this work.

2.7.2 Modern literature

In modern times, the performance of a middle slow breastshot wheel has been investigated in Müller and Wolter (2004), showing high efficiency of 80% and constant for a wide range of flow rates, from 0.2 Q_{max} up to Q_{max} (Q_{max} is the highest flow rate at maximum efficiency). No other study seems to exist. Therefore, in this thesis a breastshot wheel was deeply investigated by experimental tests (Quaranta and Revelli, 2015a; Quaranta and Revelli, 2016a) using different inflow configurations. The results were supported by a theoretical analysis for the estimation of the power losses (Quaranta and Revelli, 2015a), since old theoretical models are generally approximated and not applicable outside of a certain range, that sometimes is quite restrained, as it will be shown. A dimensional analysis will be developed to determine the maximum power output (Vidali et al., 2016). Further Computational Fluid Dynamic simulations (Quaranta and Revelli, 2016b) are also presented to show more evidence on the hydraulic behavior, focusing on the blades design. This work is documented in chapter 3.

2.8 Overshot water wheels

Overshot water wheels exploit mainly the potential energy of water (i.e. the weight of water), lowering the water within cells from the upstream channel to the tailrace (Fig. 2.12). Overshot water wheels are particularly suitable for sites with small flow rates (0.1÷0.2 m^3/s per meter width) and high heads (more than 2 or 3 meters). The blades of the cells are designed so that their curvature initially matches the curvature of the free jet as it falls from the upstream channel into the bucket. The fall that occurs as the water drops into the cells is one source of loss, because it constitutes unexploited head. The opening of each cell is slightly wider than the jet, so that the air can escape. The cells are kept as short as possible so that the weight of the water can become effective almost immediately. The cells retain the water inside until the lowest position possible, when they empty rapidly. No water should be carried over the lowest point. Overshot wheels are considered the most efficient type of water wheel (Müller and Kauppert, 2004).

2.8.1 Historic literature

In the historic literature, overshot wheels have a diameter which is a little smaller than the distance between the downstream water surface and the upstream channel bed. Garuffa (1897) suggests to adopt a diameter of (1) $D = [H - (1.1v^2/2g) -$

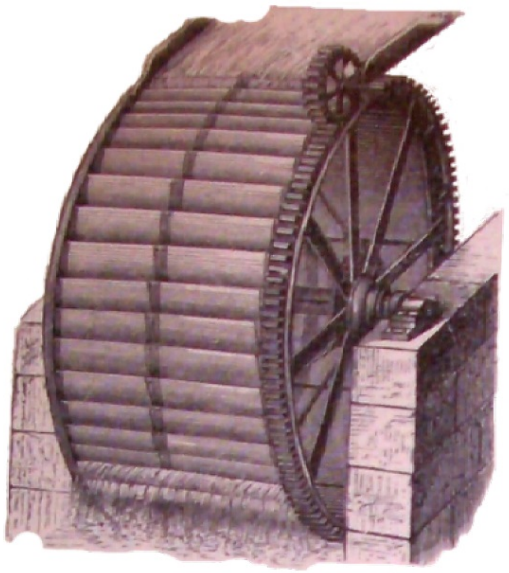

Fig. 2.12. An example of overshot water wheel (Brockhaus, 1903).

$0.1]$ m, while Weidner (1913) (2) $D = [H - (1.1c^2/2g) - (0.1 \div 0.2)]$ m, with $c = 4.54\sqrt{u}$, where u is the wheel tangential speed and v the jet velocity. A practical rule can be (3) $D = 0.85H$ (Paoli, 2006). The number of buckets can be estimated by different formulations; (1) $n = 18R$ (Pacinotti, 1851), (2) $n = 18+9R$ (Weisbach, 1849) or (3) $n = 16R$ with R in meters (Cullen, 1871). These laws are compared in Fig. 2.13.

Some authors give indications on the peripheral distance between two buckets, instead of the number of blades, which should be (1) $l = 0.32 \div 0.35$ m (Bresse, 1869), (2) $l = (4/3 \div 3/2)s$, with s the depth of the water jet (Garuffa, 1897) and (3) $l = 7(1 + 4d)$ with d the depth of the buckets in meters (Weisbach, 1849). Considering modern results, (4) $l = 1.25d$, with d the depth of the buckets (Paoli, 2006) and (5) $l = 0.75d + 0.1$ m (Nuernbergk, 2014) as in Fig. 2.14.

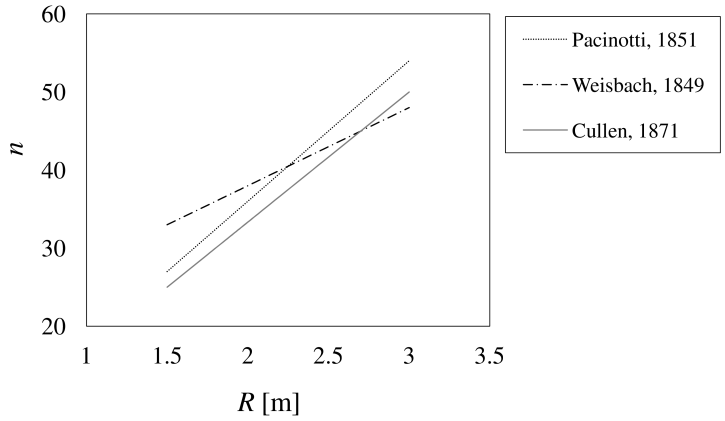

Fig. 2.13. The number of blades proposed by *Pacinotti* (1851), *Weisbach* (1849) and *Cullen* (1871) as a function of the radius R. The three Authors' laws give similar results.

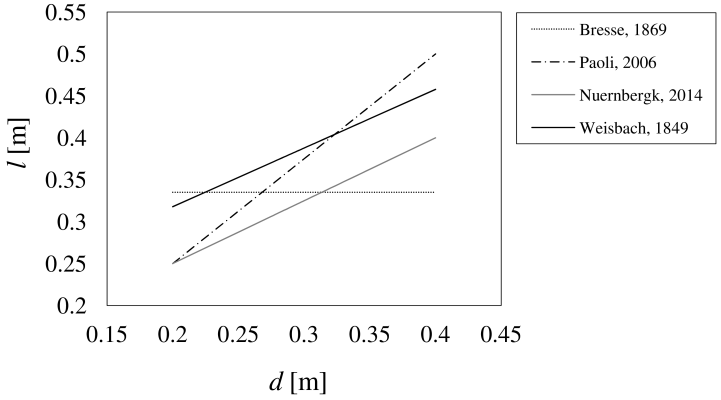

Fig. 2.14. The distance between two blades proposed by *Bresse* (1869), *Paoli* (2006), *Nuernbergk* (2014) and *Weisbach* (1849) as a function of the depth d. The length ranges between 0.25 m and 0.45 m.

The depth of the buckets can be estimated by the following rules: (1) $d = 0.2 \div 0.35$ m (Bresse, 1869; Weisbach, 1849); (2) $d = 1/6(H)^{1/3}$ (Garuffa, 1897); $0.05 < d/R < 0.26$ (Ovens 1977), thus an average of (3) $d = 0.15R$; (4) $d = (1/6 \div 1/4) \cdot 2.21H^{1/3}$ (Weidner 1913), with the dimensions in meters.

Garuffa and Weisbach propose a rotational speed (1) $u = 1.5 \div 2$ m/s, while Cullen (1871) (2) $u = 2.3D^{1/3}$ m/s, Williams (2000) (3) $u < 0.4 \cdot 42.3D^{-1/2}$ rpm and Müller and Kauppert (2002) a ratio (4) $u/v < 0.6$.

In Pelliciardi (2015) an overshot water wheel (3 m in diameter) has been designed and installed in a site with an head of 3.5 m; 32 buckets were used, with

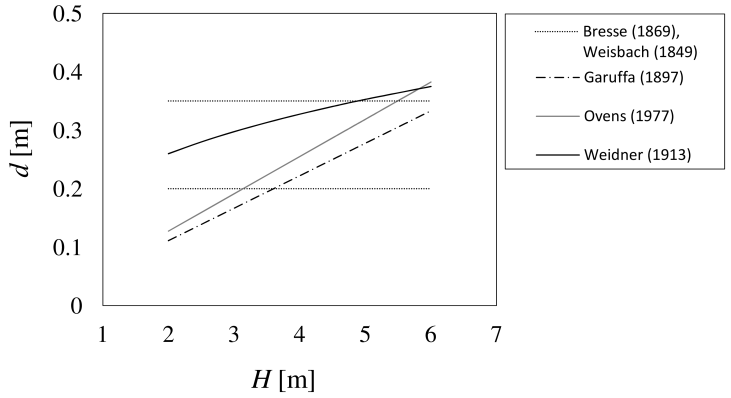

Fig. 2.15. The depth of the buckets proposed by *Bresse* (1869), *Weisbach* (1849), *Garuffa* (1897), *Ovens* (1977) and *Weidner* (1913) as a function of the head H. In the equations where the radius/diameter appears, the value $D/H = 0.85$ is adopted. The first two Authors give the same limit values, while *Weidner* proposed higher depths with respect to *Garuffa* and *Ovens*.

a depth of $d = 0.16R = 0.24$ m. The wheel is 0.84 m wide, and the cells have a filling ratio of 1/3; the wheel rotates at 10 rpm. The German company Hydrowatt has been installing overshot water wheels for heads from 3 to 5 m, with diameters 0.3÷0.4 m smaller than the head, and rotational speeds between 5.7 to 12 rpm (using the Williams formula, the rotational speed should be 7.5-9.8 rpm). Table 2.4 reports some examples of existing overshot water wheels.

Table 2.4. Some characteristics of overshot water wheels in operation collected by Quaranta, E., with their exploited head H, flow rate Q, diameter D, width b, number of blades n, rotational speed N and electrical power P_{el}. Water wheels installed by: [1] American company, [2] England company [3] German company, [4] Austrian professional office, [5] water mill in Italy, investigated in this thesis, [6] water mill in Italy.

Company/Location	H [m]	Q [$\frac{m^3}{s}$]	D [m]	b [m]	n $-$	N [rpm]	P_{el} [kW]
Smith Engineering (UK) [1]	-	-	4.1	-	24	-	-
Free flow 69 (UK) [2]	-	-	2	-	24	-	-
Free flow 69 (UK)	-	-	3.2	-	32	-	-
Hydrowatt (Germany) [3]	3		2.6	2.5	24	11	10
Hydrowatt (Germany)	3		2.7		28	11	3.5
Hydrowatt (Germany)	5.3	0.12	5		48	5.7	5
Hydrowatt (Germany)	4.6		4.2	1.5	36	7	11
Hydrowatt (Germany)	3.4		2.9	4	36	12	27
Hydrowatt (Germany)	3		2.7	1	-	-	5.5
Pelliciardi (2015), (Nepal)	3.5	0.15	3	0.84	32	10	2.5
Mitterfellner GMBH (Bauernhaus Panzer, Austria) [4]	4	0.2	-	0.5	36	-	6.44
Mitterfellner GMBH, Austria	4	0.2	4	1	36	7	5.5
Ciconio mill (Italy) [5]	-	0.058	3	2	24	-	-
Dronero mill (Italy) [6]	-	-	3	1.3	30	-	-

The most inconvenient is that the blades in the lowest part of overshot wheels rotate in the opposite direction with respect to the water in the tailrace; to avoid the impact between blades and the tailrace, the overshot wheel is usually lifted above the tailrace (but in this way the residual unexploited head represents a loss), or the pitch back water wheel is used, which rotates in the same direction of the tailrace.

2.8.2 Modern literature

Nowadays, the performance of an overshot water wheel has been investigated in Williams and Bromley (2000) using different slopes of the upstream channel; the higher the slope, the higher the efficiency, since the water was directed into the buckets better and the impact force into the blades increased. In Wahyudi et al. (2013) a new configuration has been studied for increasing the performance. The water that was lost from the buckets was recovered in tank and then squirted into

the blade under the wheel axis (the blade that is just become empty). The results will be better discussed and compared in section 4.1.2 and section 4.4.4.2, respectively. In Pelliciardi (2015) a design procedure for overshot water wheels is illustrated using the historical rules previously found, and obtaining an efficiency of 67%, including also the power losses in the channel and sluice gate. Some historic results have been presented in Müller and Kauppert (2002), but the performance was not investigated beyond the optimal efficiency point, whose efficiency was 85%.

Therefore, one objective of the present thesis will be the complete investigation of the performance of overshot water wheels. The elaboration of a theoretical model for the estimation of the power losses will be also presented, focusing on the volumetric losses at the top of the wheel, never previously considered in literature; these results have been published in Quaranta and Revelli (2015b). Computational Fluid Dynamic simulations (Quaranta and Revelli, 2016d) will be also performed with the aim of improving the performance with an alternative and more efficient method with respect to Wahyudi et al. (2013). The objective of the numerical simulations is to reduce the volumetric losses at the top of the wheel, by modifying the wheel geometry.

2.9 Conclusions and comparisons

In the previous sections, water wheel technology was described. Before discussing the performance in detail by illustrating the results of experiments and theoretical/numerical analyses conducted in this thesis, in this section a brief summary is reported.

Stream water wheels use the kinetic energy of flowing water. Stream wheels are employed in sites where discontinuity in the channel bed, i.e. geometric heads, are negligible. Stream wheels are the less efficient type of water wheel, and their diameter generally is 4-5 m. Therefore, their design should be done very carefully, by selecting appropriately the number of the blades and, especially, the wheel rotational speed. A significant attention should be devoted to the surrounding structure that includes the wheel, i.e. the bottom shroud and the inlet and outlet channel. Anyway, if a stream water wheel obstructs the channel generating a dam effect, an hydraulic head can be generated through the wheel; this leads to higher efficiencies (up to 80%), being also the hydrostatic force used.

On the other hand, gravity wheels exploit the potential energy of flow; the water weight is the force that drives the wheel. In Tab. 2.1 a summary of their operational range was reported.

Overshot water wheels exhibits maximum efficiency of 85% and constant over a wide range of flow rates. They are used in sites with less than 150 l/s of flow rate per meter width of the wheel and head up to 10 m (generally up to 6 m for practical limitations). The diameter is generally long as the vertical distance between the downstream free surface and the upstream channel bed; the number of the blades depends on the diameter.

Breastshot water wheels are used in sites with hydraulic heads less than 4 m. They exhibit maximum efficiency of 85%, that reduces at 75% using an upstream sluice gate to regulate the upstream head (results found in this thesis). The diameter of high breastshot wheel is a little higher as the analogous for overshot wheels. The diameter is more than twice the hydraulic head for middle breatshot wheels, and approximately between 3 to 10 times the hydraulic head for low breastshot and undershot water wheels, respectively. The choice of which kind of breastshot wheel to use depends on the flow rate; low breastshot wheels can be used for flow rates up to 1.2 m^3/s per meter width, while middle and high breastshot wheels up to 0.65 m^3/s per meter width.

Chapter 3

Investigation of a Breastshot water wheel

Since breastshot wheels can be employed in a wide range of hydraulic conditions, especially in irrigation canals, they seem to be the most diffused kind of water wheel in Italy, although there is not a reliable repository that demonstrate this. In the scientific literature, only in Müller and Wolter (2004) experimental tests have been illustrated, where a small prototype of a breastshot water wheel has been investigated. Instead, the historic literature generally presents theoretical models to estimate the performance and practical recommendations for the design.

In this thesis, a prototype breastshot wheel was identified in the old water mill of Verolengo (Fig.3.1), near Turin (Italy), and a physical model of it was installed and investigated in the test canal of the Hydraulics laboratory at Politecnico di Torino, with a geometric scale factor $\lambda = 0.5$. The performance of the wheel was investigated at different flow rates, hydraulic heads, water depths and wheel rotational speeds. Theoretical models to estimate the efficiency were also elaborated and compared to past ones; numerical Computational Fluid Dynamic simulations were carried out to improve the design. Fig.3.1 depicts the wheel sited in Verolengo. Its diameter is 4 m, the width is 1.3 m and the number of blades is 32.

In the next sections, the experimental setup and results will be described. These results have also been published in Quaranta and Revelli (2016a). In section 3.2 a theoretical analysis will be developed with the aim of the estimation of the power losses and the efficiency of the wheel (published in Quaranta and Revelli, 2015a), while in section 3.3 a dimensional analysis will be developed for the estimation of the maximum power output of similar breastshot wheels (published in Vidali et al., 2016, that includes the author of this thesis). Numerical

Fig. 3.1. The breastshot water wheel in Verolengo.

simulations will be presented in section 3.4, and the results have also been published in Quaranta and Revelli (2016b). The last analysis that was conducted was the experimental investigation of the same breastshot water wheel using a vertical inflow weir as inlet, and also published in Quaranta and Revelli (2016a); for a better organization and understanding, this experimental investigation will be also presented in section 3.1.

3.1 Experimental tests

3.1.1 Experimental setup

An experimental channel has been installed in the Laboratory of Hydraulics at Politecnico di Torino with the aim of testing breastshot, undershot and overshot water wheels. Glass walls were provided for the observation of the flow when the wheel was in operation (Fig.3.2).

The diameter of the wheel model is $D = 2R$=2.12 m, the width is $b = 0.65$ m and the number of the blades is $n = 32$. The channel is schematically illustrated in Fig.3.3, while Fig.3.4 depicts the water wheel. In particular, Fig.3.5 depicts the blade in correspondence of the water entry point, where the circular curb below of the wheel starts.

The flow rate Q_{in} to the wheel was set by a pump and a gate valve installed in the supply pipe of the channel. The flow rate was detected by an electromagnetic flow meter (type Promag 30, Model '99); the accuracy of the flow rate estimation was $\delta Q_{in} = \pm 0.5 \cdot 10^{-3}$ m^3/s. The pipe is connected to a tank, where two sluice gates are installed (Fig.3.3) in order to regulate the water level in the tank and the

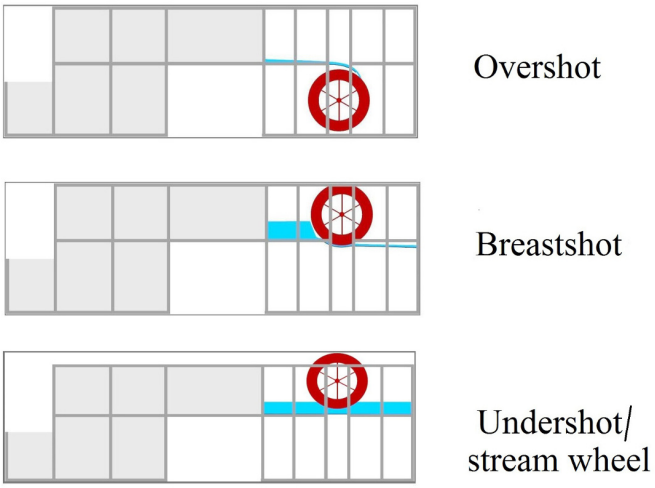

Fig. 3.2. Sketch of the experimental channel, with flow from left to right.

flow to the wheel. The leakages (Q_{lost}) through the back sluice gate (sluice gate "B" in Fig.3.3) were measured, obtaining the actual flow rate (Q) exploited by the wheel. The lost flow rate Q_{lost} was measured by a Thomson weir equipped with an ultrasonic sensor (type 100-2000 mm-4-20 mA, Italy) for the measurement of the water depth. The ultrasonic sensor accuracy was $\pm$ 1 mm, thus the error of Q_{lost} could be estimated from the weir calibration curve in less than 3% of the measure for the exploited range of flow rates. However, the lost flow rate of the system was negligible with respect to the total flow rate, since this was due only to the not perfect seal of sluice gate B. Flow rates $Q = 0.02 \div 0.1$ m^3/s were investigated.

A brake system was installed to regulate the wheel rotational speed (type GFC7, Italy); the brake was made of a generator and a resistor, connected at the wheel shaft. Between the wheel and the brake, a gearbox with gear ratio of 15.6 was installed to provide an optimum speed and torque range on the generator shaft (Fig.3.6a). An electrical energy analyzer and a control of the electrical resistance were installed to manage the electrical power output of the generator and the load on the wheel, regulating the wheel rotational speed N ($N = 2 \div 20$ rpm). The minimum rotational speed depended on the maximum braking torque that the brake could apply. The maximum rotational speed was close to the runaway velocity. The tangential speed of the wheel is defined as $u = NR$ at the tip of the blade.

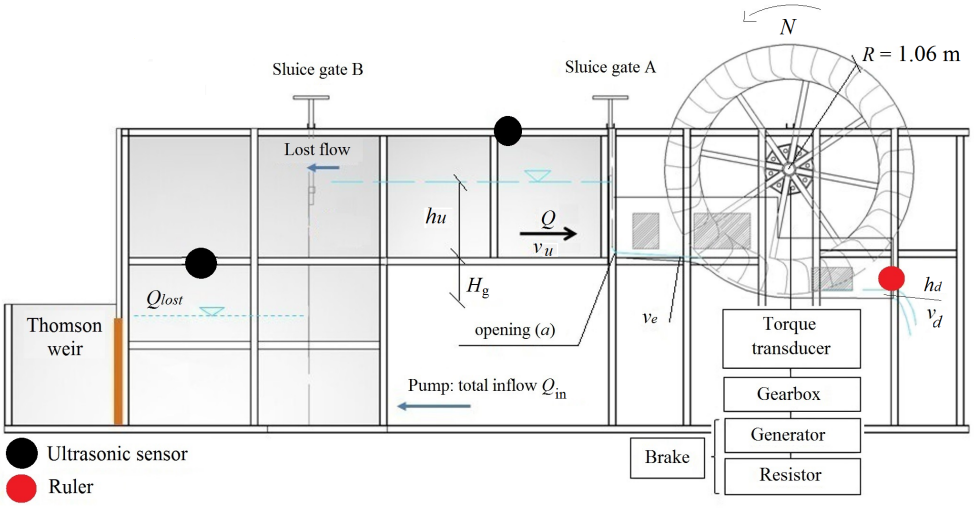

Fig. 3.3. Sketch of the experimental channel with the wheel and the variables that will be used in the experimental and theoretical results.

The rotational speed was measured by the internal clock of the acquisition board, which could discretize the output signal frequency of the inductive proximity sensor (type IME12-04BNSZC0S, Germany) till 100 MHz, with very high accuracy. A commercial torque transducer (Fig.3.6b) was installed along the transmission shaft to measure the shaft torque (C_{exp}); the precision of the torque estimation was $\delta C_{exp} = \pm 6$ Nm (type RT2.604.R6, Italy). The experimental power output $P_{exp} = C_{exp} \cdot N$ was then calculated.

In order to evaluate the power input to the wheel, the upstream and downstream water depths, h_u and h_d, respectively, were measured. The former by the ultrasonic sensor, the latter visually by the operator. The gross head difference (difference of energy head) can be expressed as:

$$H_{gr} = (H_U - H_D) = \left[\left(z_u + h_u + \frac{{v_u}^2}{2g} \right) - \left(z_d + h_d + \frac{{v_d}^2}{2g} \right) \right] \tag{3.1}$$

where H_U is the energy head upstream of the wheel (measured 2.5 m from the axle of the wheel), H_D the downstream one (energy head at the tailrace, 0.89 m from the axle of the wheel) and $H_{gr} = H_U - H_D$ is the head difference. The energy head H_x is the sum of the channel bed elevation z_x, the water depth h_x and the kinetic term ${v_x}^2/2g$, where $g = 9.81$ m/s^2 is the acceleration of gravity and v_x is the mean flow velocity (Fig.3.7).

Fig. 3.4. The installed wheel with the gearbox (blue box) and generator (black cylinder).

The mean flow velocity is calculated as $v_u = Q/B_u h_u$ and $v_d = Q/B_d h_d$, where $B_u = 1.5$ m and $B_d = 0.67$ m are the widths of the tank (upstream sluice gate A) and the channel (downstream if the wheel) in the points were the measures were made. In this case, the geometric head difference is $H_g = z_u - z_d = 0.35$ m, thus $H_g/D = 0.165$. The water depth h_u was monitored by an ultrasonic sensor with a precision of $\delta h_u = \pm 0.004$ m and the downstream depth h_d by a classical ruler, with the operator precision of $\delta h_d \simeq 0.002$ m. The downstream water depth was not regulated by any hydraulic structure, and a free falling jet into a downstream tank was generated at the end of the downstream channel. The upstream water depth depended on the opening of the sluice gate or the height of the inflow weir.

The power input of the hydroelectric plant was calculated as:

$$P_{gr} = \rho g Q H_{gr} \tag{3.2}$$

where Q is the flow rate and $\rho = 1000$ kg/m^3 is the density of water.

The global efficiency of the installed hydroelectric plant can be defined as:

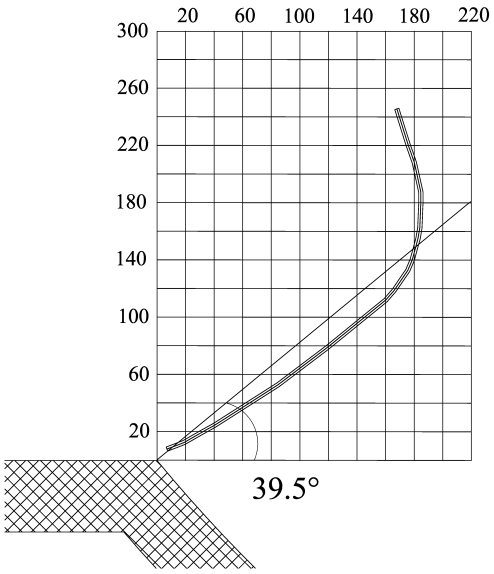

Fig. 3.5. The shape of the blade. The grid units are mm. The inclined line indicates the radial direction.

$$\eta = \frac{P_{exp}}{P_{gr}} = \frac{C \cdot N}{P_{gr}} \tag{3.3}$$

and it is a function of the flow rate, rotational speed and inflow configuration.

The first experiments dealt with the breastshot wheel equipped with a sluice gate at the inflow, as illustrated in Fig.3.7. In the figure, point E identifies the water entry point to the wheel. The sluice gate was installed 0.7 m upstream of point E and its opening a was varied between 0.050 to 0.150 m. The opening of the sluice gate allowed the regulation of the upstream water depth h_u, hence the flow velocity to the wheel. Therefore, while the flow velocity was often negligible upstream of the sluice gate (especially at small sluice gate openings), it was significant just upstream of the wheel, because of the flow acceleration passing under the sluice gate. The total number of experiments was: 39 for the sluice gate opening $a = 0.05$ m, 53 for $a = 0.075$ m, 59 for $a = 0.100$ m, 55 for $a = 0.125$ m, 48 for $a = 0.150$ m. The experimental procedure was the following: the flow rate was set by the pump, the sluice gate adjusted to the requested opening and, at the end, the rotational speed was regulated by the brake.

After the first set of experiments, the sluice gate was removed, and the channel was equipped with a vertical weir (as illustrated in Fig.3.8), changing the water entry point to the wheel.

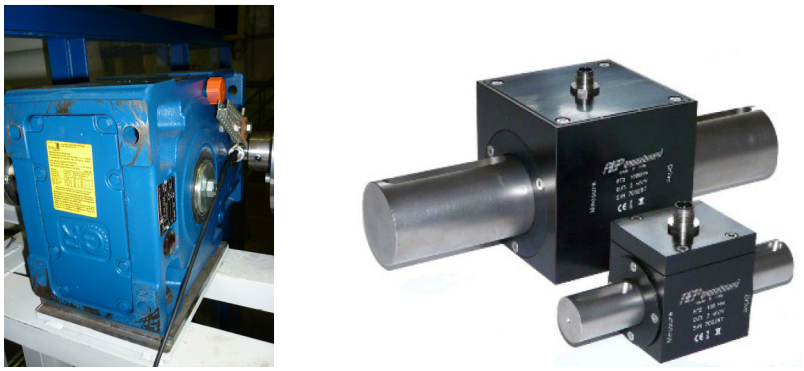

(a) *Gearbox* (b) *Torque transducer*

Fig. 3.6. Gearbox and torque transducer

Weirs of $h_s = 0.18$ m and $h_s = 0.28$ m high were investigated. Only one weir was installed at a time. Each weir was located just before the wheel, ensuring a gap of about 0.01 m between the top edge of the weir and the blades, as illustrated in Fig.3.8, in order to avoid any contact between the wheel and the weir. The first weir was 0.18 m high, and it was installed 0.12 m upstream of the water entry point (E in Fig.3.8). The second weir was 0.28 m high, and it was installed 0.17 m upstream of the entry point.

In this case, the weir was a vertical wall; the advantage of a vertical weir is its simplicity and facility of regulation. As a consequence, its downstream profile did not fit the circular shape of the wheel. This led to volumetric losses (see Fig.3.8), because a portion of water flows from the buckets toward the space V. This lost water is not definitively lost, since it re-enters into the buckets. In order to contain the volumetric losses (consider that the higher the weir, the more distant it has to be installed from the wheel), the height of the weir should be $< 1 \div 1.5$ times the external distance between two blades (l). This recommendation justifies the investigated heights; considering the diameter of the wheel of 2.12 m and 32 blades, the depth of the buckets is about 0.2 m.

A total of 42 experiments for the configurations with the weir $h_s = 0.18$ and 36 experiments for the configurations with the weir $h_s = 0.28$ m, respectively, were carried out. When the weir was in operation, the water flow did not accelerate like it did when passing under the sluice gate and it entered into the wheel from an higher elevation and at lower velocity. Therefore, considering a certain flow rate, the torque contribution of the water weight increases with the weir, whereas the torque contribution due to the kinetic energy of the flow reduces.

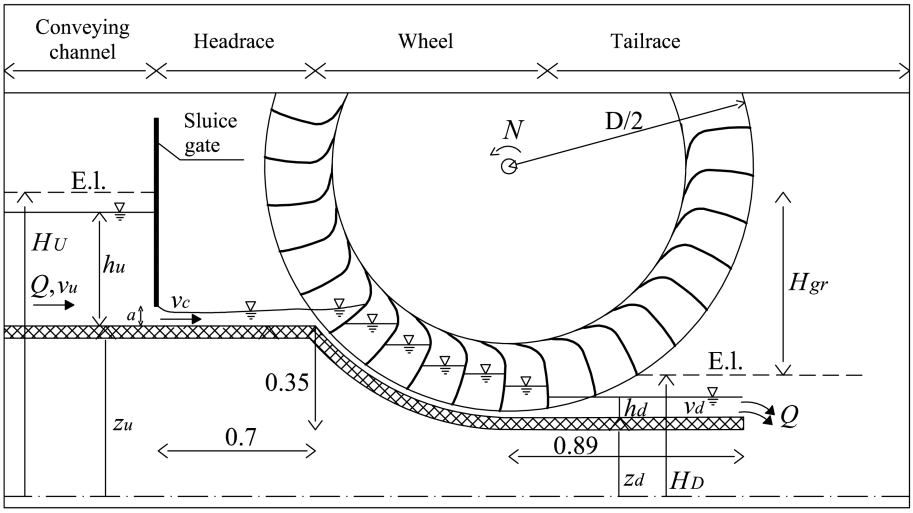

Fig. 3.7. Sketch of the experimental wheel, which is the scale model of the wheel in Verolengo. E.l. = energy line. Units in meter.

3.1.2 Error analysis

Scope of this section is to estimate the error δ on each quantity derived from the experimental measurements, applying the error propagation laws.

The width of the channel b, the wheel radius R and the geometric head H_g are considered known, thus without error.

As mentioned before, the error of the measurements is $\delta Q = \pm 0.5 \cdot 10^{-3}$ m^3/s for the flow rate and $\delta C_{exp} = \pm 6$ Nm for the torque, $\delta h_u = \pm 0.004$ m for the upstream water depth and $\delta h_d = \pm 0.002$ m for the downstream one.

The estimated error of the power output can be calculated as:

$$\delta P_{exp} = \pm P_{exp} \cdot \frac{\delta C_{exp}}{C_{exp}} = \pm 6 \cdot N \tag{3.4}$$

since the rotational speed N was measured by the internal clock, the accuracy was very high and not significant for the error analysis.

Considering the generic velocity $v_x = Q/(Bh_x)$, the error of the velocity measurement can be calculated as:

$$\frac{\delta v_x}{v_x} = \frac{\delta Q}{Q} + \frac{\delta h_x}{h_x} \tag{3.5}$$

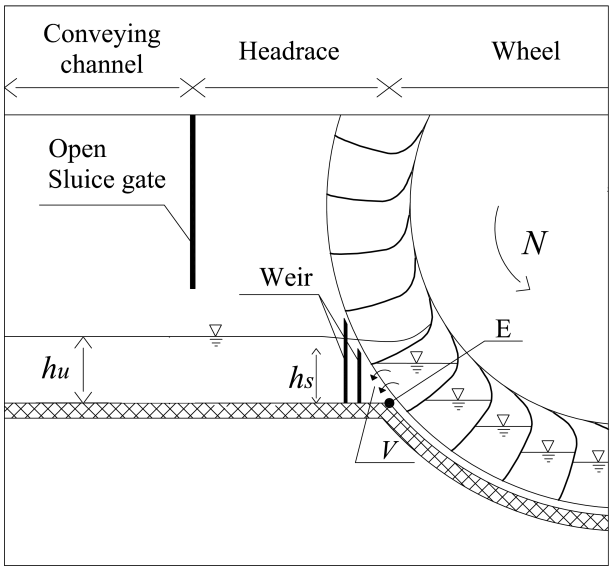

Fig. 3.8. The configuration with the sluice gate totally opened and the vertical overflow weirs just before the wheel. In the figure, h_s refers to the shortest weir.

where the subscript x can refer both to the upstream quantities (water depth h_u and flow velocity v_u), and to the downstream ones (h_d and v_d). The error of the velocity to the second power (the kinetic term) is:

$$\frac{\delta {v_x}^2}{{v_x}^2} = 2\frac{\delta v_x}{v_x} \rightarrow \delta {v_x}^2 = 2v_x \delta v_x \tag{3.6}$$

where δv_x can be calculated by eq.3.5.

The error of the head difference (eq.3.1) estimation can be calculated as:

$$\delta H_{gr} = \delta h_u + \frac{1}{2g}\delta {v_u}^2 + \delta h_d + \frac{1}{2g}\delta {v_d}^2 \tag{3.7}$$

where $\delta {v_x}^2 = 2{v_x}^2 \left(\frac{\delta Q}{Q} + \frac{\delta h_x}{h_x}\right)$.

The error of the measurement of the power input $P_{gr} = \rho g Q H_{gr}$ can be quantified in:

$$\delta P_{gr} = \rho g(\delta[QH_{gr}]) = \rho g Q H_{gr}\left(\frac{\delta Q}{Q} + \frac{\delta H_{gr}}{H_{gr}}\right) \tag{3.8}$$

The error of the efficiency estimation ($\eta = P_{exp}/P_{gr}$) can be expressed as:

$$\delta\eta = \eta \left(\frac{\delta P_{exp}}{P_{exp}} + \frac{\delta P_{gr}}{P_{gr}} \right) \tag{3.9}$$

Consider a representative case with $Q = 0.05$ m^3/s, $h_u = 0.5$ m, $h_d = 0.1$ m (hence $H_{gr} = 0.72$ m and $P_{gr} = 354$ W), $N = 1$ rad/s, and $\eta = 0.7$ (hence $P_{exp} = 248$ W). The accuracy of the head difference estimation is $\delta H_{gr} = 0.0078$ m, $\delta P_{gr} = 7.35$ W for the power input, $\delta P_{exp} = 6$ W for the power output and $\delta\eta = 0.031$ for the efficiency. These values are lower if compared to their respective measured quantities, hence they can be considered acceptable.

Experimental results

3.1.2.1 Experimental results and discussion

Scope of the present section is to compare the performance of the breastshot water wheel using the two inflow configurations.

Figure 3.9 depicts the efficiency trends for selected flow rates versus the rotational speed in revolutions per minute. In the sluice gate configuration the efficiency increases up to a maximum, and then it decreases (the maximum efficiency occurs in correspondence of the maximum power output). Instead, in the weir configuration the efficiency trend is quite constant. This difference can be justified in this way. The kinetic energy of the flow entering into the wheel is lower in the case with the weir with respect to the kinetic energy of the flow when the sluice gate is installed (in the latter case the flow accelerates passing under the sluice gate). Thus the contribution of the kinetic energy of the flow to the torque (as well as to the efficiency) is lower in the weir configuration. Since the wheel rotational speed affects the transfer of kinetic energy from the flow to the wheel (i.e. the relative flow velocity and the impact power losses), it is reasonable that the efficiency trend is less affected by the wheel rotational speed when the weir is installed.

For each flow rate, the opening (a) of the sluice gate influences significantly the efficiency, whereas the height of the weir is not so important. The lower the opening the higher the flow velocity to the wheel, hence the lower the efficiency, due to the larger power losses generated. The efficiency reduction with the lowering of the sluice gate is worsened with the increase of the flow rate, since the water velocity also increases with the flow rate. High water velocities generate significant power losses both during the filling process (the impact against the blades) and in the conveying channel (Quaranta and Revelli, 2015a). It can be

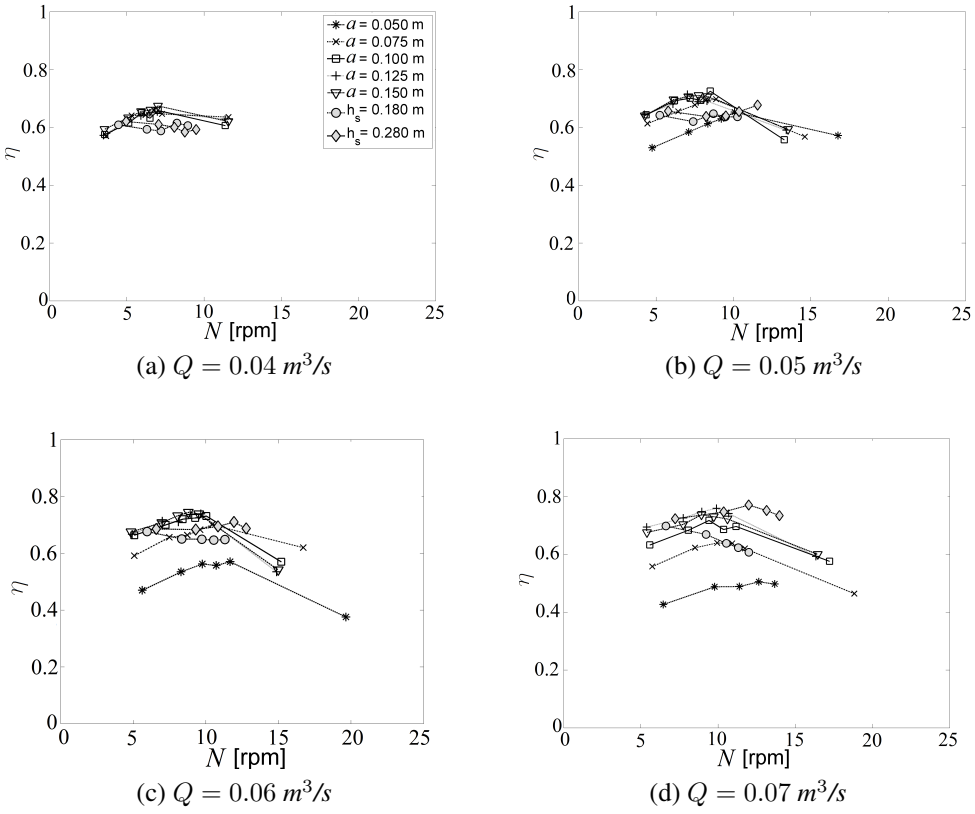

(a) $Q = 0.04\ m^3/s$ (b) $Q = 0.05\ m^3/s$

(c) $Q = 0.06\ m^3/s$ (d) $Q = 0.07\ m^3/s$

Fig. 3.9. Efficiency versus the wheel rotational speed for different inflow configurations and flow rates. The legend is shown in the figure at the top left corner. a is the opening of the sluice gate and h_s the height of the weir.

also observed that, for the sluice gate, the higher the flow rate the higher the optimal rotational speed (which is the speed at the maximum efficiency). This can be justified considering that the higher the flow rate (and, as a consequence, the upstream water level), the faster the flow velocity to the wheel, thus the higher the value that the rotational speed can assume for optimizing the impact conditions. However, although the optimal rotational speed increases with the the flow rate (thus with the entry flow velocity), the ratio u_v/v_e initially increases with the flow rate, and then decreases, with $u_v = u \cdot cos(\alpha)$ the tangential wheel speed (at the edge of the blade) in the direction of the entry flow velocity v_e (α is the angle between u_v and v_e, hence the angle between the tangential speed and the horizontal). In Tab.3.1 the ratios u_v/v_e are reported. u_v is the tangential speed component in the direction of the entry flow velocity v_e.

Table 3.1. Ratio u_v/v_e for each sluice gate opening and flow rate.

Inflow case (m)	Q (m^3/s)								
	0.02	0.03	0.04	0.05	0.06	0.07	0.08	0.09	0.10
a =0.05	0.10	0.25	-	0.31	0.28	0.27	0.28	-	-
a =0.075	0.22	0.29	0.34	0.37	0.36	0.30	0.35	0.33	0.26
a =0.10	0.27	0.51	0.38	0.45	0.45	0.37	0.37	0.31	0.30
a =0.125	0.31	0.43	0.61	0.45	0.53	0.43	0.48	0.37	0.35
a =0.15	-	0.51	0.61	0.60	0.54	0.47	0.47	0.40	0.46

The results in Tab.3.1 can be summarized by the following equations:

$$u_v/v_e = (-26.74a + 0.419)Q + (4.196a + 0.128) \tag{3.10}$$

excluding the flow rates lower than 0.04 m^3/s.

Using dimensionless terms, the previous equation becomes:

$$u_v/v_e = (-1.239a^* - 0.216)Q^* + (1.726a^* + 0.193) \tag{3.11}$$

where $Q^* = Q/(u \cdot H_g^2)$, as defined in Vidali et al. (2016) (see section 3.3), and $a^* = a/H_g$. Equation 3.11 can be solved iteratively.

Figure 3.10 shows the maximum experimental power output (power output at maximum efficiency) versus the flow rate. Over a certain flow rate and at small sluice gate openings, the power output trend becomes non linear, due to the fact that the power generated by the impact becomes significant, that depends on the square of the flow rate.

For the cases with the sluice gate, the power output P_{exp} increases with the reduction in the sluice gate opening, because of the higher entry flow velocity. When the weir is installed, the power output increases with the height of the weir, because of the increase in the elevation of the entry point of water, hence in the potential energy. The power output at maximum efficiency for the weir configuration is generally higher at a certain flow rate. This is due by the fact that when the weir is installed, the water weight starts to push the paddles from higher elevations, although the torque due to the kinetic energy of the flow is lower, compared to what happens with the sluice gate. Since the weir leads to higher power output, this means that the increase in the torque due to the water weight is more important than the decrease in the kinetic contribution. This confirms the fact that gravity water wheels (which exploit the water weight, thus the potential energy)

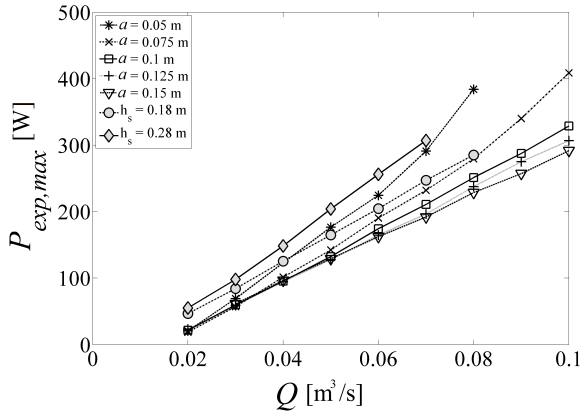

Fig. 3.10. Maximum measured experimental power output versus the flow rate. a is the sluice gate opening and h_s the weir height.

are more efficient than stream water wheels. However, at flow rates bigger than 0.08 m^3/s the trend of the power output for sluice gate openings lower than 0.075 m seems to overcome the trend for the cases with the weir, due to the non linearity of the power output (Fig.3.10).

Figure 3.11 depicts the maximum efficiency versus the flow rate and normalized flow rate Q/Q_{max} (Q_{max} is the highest flow rate at maximum efficiency). The term maximum efficiency η_{max} means the maximum efficiency value over the investigated range of rotational speed, at a certain flow rate and inflow geometric configuration (sluice gate opening and inflow weir). The flow rate Q_{max} is the highest flow rate that, for a certain inflow geometric configuration, gives the maximum value of η_{max}.

The first observation that can be made is the difference between the efficiency trends in the two geometric inflow configurations. Considering the cases with the sluice gate, the efficiency increases up to a maximum value. Then, when $a > 0.10$ m the maximum value remains almost constant at 75%; the range of constant efficiency is included between $Q = 0.05$ to $Q = 0.08 \div 0.09$ m^3/s. The constant range corresponds to $(0.56 \div 0.6) \cdot Q_{max}$ and Q_{max}, where Q_{max} is the maximum flow rate in the range of constant efficiency for each geometric inflow configuration (Fig.3.11). For sluice gate openings $a \leq 0.10$ m there is not a constant efficiency range, and, for a certain sluice gate opening, Q_{max} corresponds to the flow rate at the maximum efficiency. The efficiency starts to decrease from $Q = 0.05 \div 0.06$ m^3/s. The smaller the sluice gate opening, the lower Q_{max}. This is justified by the fact that at a certain flow rate, the smaller the sluice gate opening, the higher the upstream water depth and the flow velocity to the wheel, thus the more significant are the power losses upstream of the wheel. Hence, the

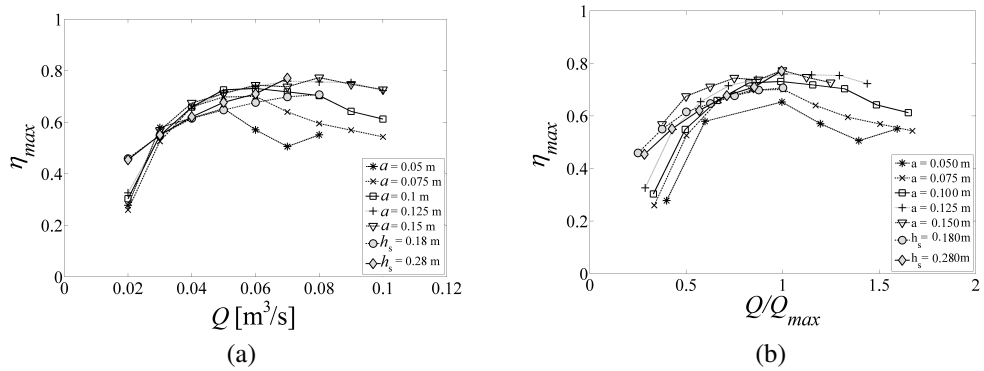

Fig. 3.11. (a) Maximum efficiency versus the flow rate. (b) Maximum efficiency versus the normalized flow rate. The dimension of the channel limited the exploitable flow rate to 0.08 m^3/s at very low sluice gate openings. h_s the weir height and a is the sluice gate opening. Q_{max} is 0.05, 0.06, 0.07, 0.08 and 0.08 m^3/s for a= 0.05, 0.075, 0.100, 0.125 and 0.150 m.

smaller the sluice gate opening, the lower the maximum flow rate should be in order to avoid excessive flow velocities to the wheel and energy losses.

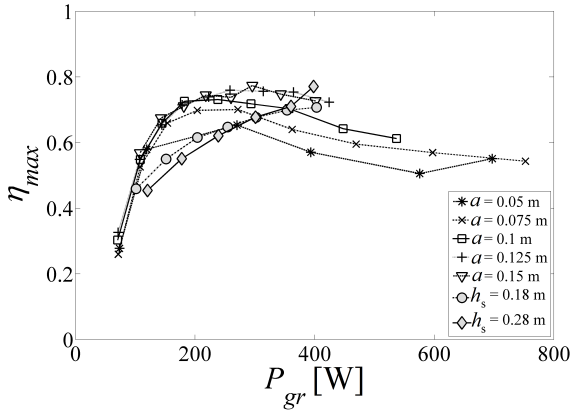

Fig. 3.12. Maximum efficiency versus power input.

Considering the inflow weirs, the efficiency trend is instead increasing and more regular (Fig.3.11). This observation suggests that the optimal flow rate is higher in the weir configuration (due to the geometric limitations of the experimental channel -the height of the glass walls-, it was not possible to investigate higher flow rates). Hence the configuration with the weir allows to exploit efficiently larger flow volumes, i.e. flow rates $Q > 0.08$ m^3/s in the present case. The efficiency of the plant equipped with the weir improves also at flow rates of $Q = 0.02$ m^3/s, increasing from $\eta = 0.25 \div 0.30$ with the sluice gate to $\eta = 0.45$

using the weir. This occurs because at very low flow rates the contribution of the kinetic energy is negligible; therefore, it is more convenient to use a weir in order to enhance the water elevation, and not exploiting the kinetic energy of the flow by the reduction of the sluice gate opening.

These results show that the efficiency with the sluice gate depends significantly on the flow rate, while this dependency is less appreciable using the inflow weir. This result is confirmed in Müller and Wolter (2004), where a breastshot water wheel equipped with an inflow weir has been investigated: its efficiency was constant already from flow rates of $0.2 \cdot Q_{max}$, while the present breastshot wheel with the sluice gate exhibits constant efficiency in the range $(0.56 \div 0.6) \cdot Q_{max}$ and Q_{max}.

In Fig.3.12 it can be observed that in the range $P_{gr} = 150 \div 400$ W the efficiency with the weir is lower, probably due to the volumetric losses occurring downstream of the weir, as explained in section 3.1.1, while the efficiency is higher for power inputs higher than 400 W ($P_{gr} > 400$ W). The efficiency at power inputs higher than 400 W ($P_{gr} > 400$ W) decreases with the reduction of the sluice gate opening. Such situation corresponds to high flow rates and upstream water depths h_u, leading to high flow velocities downstream of the sluice gate. As a consequence, this generates larger power losses in the impact of water against the paddles and in the headrace, due to turbulence and bed friction (Quaranta and Revelli, 2015a). Hence the use of the weir becomes more advisable than the sluice gate in these conditions.

Concluding, the power output with the weir at 0.28 m is generally higher than the power output with the weir at 0.18 m in height (Fig.3.10); however, the efficiencies in both cases are similar (Fig.3.11).

3.1.2.2 Discussion: practical applications

The previous sections have showed the different optimal hydraulic conditions where the inflow weir and the sluice gate should operate. The weir works better at low and high flow rates, and low and high power inputs. Therefore, the sluice gate and the weir can be used as a function of the external hydraulic conditions to optimize the efficiency of breastshot water wheels.

The regulation of the sluice gate opening can be also a way to guarantee always the optimal operative conditions for a constant speed of operation N_c, at variable flow rate. When the flow rate changes, also the optimal speed of the wheel changes, since the optimal rotational speed depends on the flow rate. But if also the inflow conditions are changed N_c can continue to be the optimal one.

Fig.3.13 depicts the rotational speed at the maximum efficiency versus the sluice gate opening at different flow rates, for the tested wheel, in order to shed light on what has been just said.

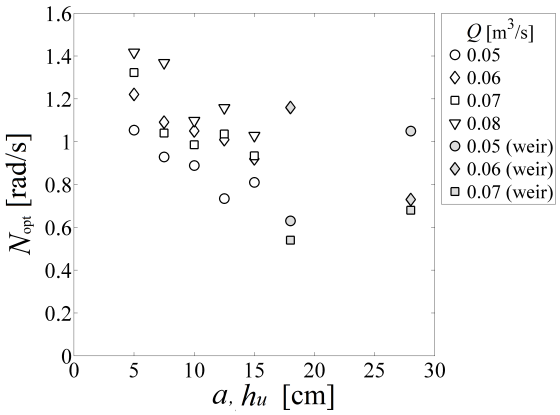

Fig. 3.13. Optimal rotational speeds of the wheel versus the sluice gate openings and weir heights (full color symbols). Some representative flow rates are considered.

Using Fig.3.13, at a fixed sluice gate opening and flow rate, the wheel rotational speed required to obtain the maximum efficiency is determined. The lower sluice gate openings (a) (thus the higher the flow velocity to the wheel), the higher the wheel rotational speed required for the maximum efficiency (refer also to Fig.3.9). When it is needed that the wheel operates at a constant rotational speed with variable flow rates, it is possible to determine for each flow rate the sluice gate opening which guarantees that the same rotational speed N_c remains optimal (using a graph similar to Fig.3.13). Furthermore, the optimal efficiency is also guaranteed, since the graph is conceived using the maximum efficiency data. The use of the sluice gate can also cooperate with the weir, that should be used at very low and big flow rates. Otherwise, if the variable speed of operation is preferred, and the geometric configuration is fixed (fixed sluice gate opening in this case), a costly rectifier/control/inverter system and expensive gearboxes (Müller and Kauppert 2004) are necessary to change the wheel rotational speed, depending on the flow rate.

3.1.2.3 Discussion: practical applications in dimensionless terms

Some results are now discussed as a function of dimensionless parameters. The theory that leads to these dimensionless parameters will be explained in detail in section 3.3 (Vidali et al., 2016).

The normalized power input is defined as follows (Vidali et al. 2016):

$$P_{gr}^{*} = \frac{P_{gr} \cdot {H_g}^4}{\rho Q^3} \tag{3.12}$$

whose error (considering the representative case, section 3.1.2, $P_{gr}^{*} = 42.5$) can be estimated as:

$$\delta P_{gr}^{*} = \frac{{H_g}^4}{\rho}\delta\left[\frac{P_{gr}}{Q^3}\right] \rightarrow \frac{{H_g}^4}{\rho}\frac{P_{gr}}{Q^3}\left(\frac{\delta P_{gr}}{P_{gr}} + 3\frac{\delta Q}{Q}\cdot Q^3\right) = 0.88\text{W} \tag{3.13}$$

which is 2% of P_{exp}.

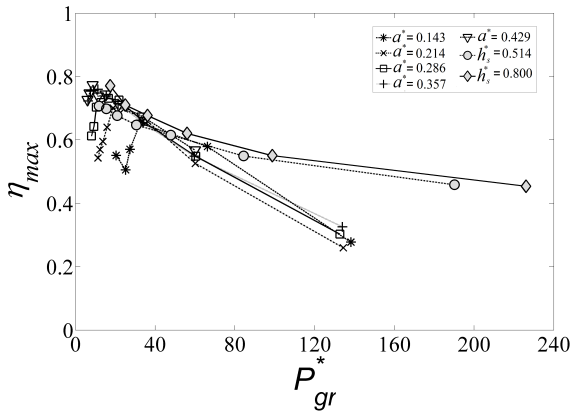

Fig. 3.14. Maximum efficiency (i.e. the maximum efficiency considering the trend of efficiency versus the rotational speed for each sluice gate opening and power input, as well as flow rate) versus the normalized power input. In the legend, the inflow configurations (a is the sluice gate opening and h_s is the height of the weir) are normalized to the geometric head difference $H_g = 0.35$ m, obtaining a^* and ${h_s}^*$.

Figure 3.14 can be used to determine the optimal inflow condition as a function of the normalized power input (in order to ensure the maximum efficiency). The normalized power input depends on the geometric head difference at full scale and on the operative flow rate. Since the power input depends on the inflow configuration, which is not known yet, an iterative process has to be adopted. In Fig.3.14, the normalized sluice gate opening a^* and weir height ${h_s}^*$ are scaled with the geometric head difference H_g (which is 0.35 m in our case). The graph can also be used as useful generalized tool to estimate the wheel efficiency as a function of the hydraulic conditions. In Fig.3.14, the lower the flow rate, the higher the dimensionless power input for each configuration. Observing the trends starting

from the highest power inputs, hence for increasing flow rates, the trends with the sluice gate initially increase. After reaching a maximum, which occurs at the optimal P^*_{gr} (thus the optimal flow rate), the trends decrease considerably for sluice gate openings $a \leq 0.10$ m or $a^* \leq 0.286$. The smaller the sluice gate opening the higher the optimal dimensionless power input at the maximum efficiency, thus the lower the optimal flow rate (as discussed in the description of Fig.3.11). Considering the weirs, the trends do not exhibit a maximum, because the experimental channel did not allow to explore higher flow rates. For $P^*_{gr} > 70$ it is more advisable to use the weir, while for $P^*_{gr} < 70$ the efficiency trends of the two inflow configurations are very close together; this does not happens for $a^* \leq 0.286$ when the efficiency trends decrease at normalized power input lower than the optimal ones.

Once the inflow configuration is determined using Fig.3.12, by Tab.3.2 the optimal rotational speed can be estimated.

Table 3.2. Normalized tangential speed u^* of the wheel at the optimal efficiency for each inflow case and flow rate.

Inflow case (m)	Q (m^3/s)								
	0.02	0.03	0.04	0.05	0.06	0.07	0.08	0.09	0.10
a =0.05	0.06	0.21	-	0.34	0.36	0.35	0.36	-	-
a =0.075	0.10	0.18	0.27	0.34	0.38	0.34	0.42	0.41	0.34
a =0.1	0.10	0.22	0.29	0.35	0.40	0.36	0.39	0.35	0.36
a =0.125	0.12	0.19	0.29	0.29	0.39	0.40	0.44	0.37	0.38
a =0.15	-	0.22	0.29	0.32	0.36	0.36	0.40	0.37	0.45
h_s =0.18	0.099	0.24	0.29	0.30	0.21	0.23	0.25	-	-
h_s =0.28	0.13	0.18	0.16	0.37	0.38	0.39	-	-	-

Table 3.2 shows the optimal normalized tangential speeds u^* of the wheel at the highest efficiency for each inflow case and flow rate ($u = N \cdot R$).

$$u^* = \frac{N \cdot R}{\sqrt{2gH_{gr}}} \tag{3.14}$$

whose error (for the same previous representative case to which corresponds $u^* = 0.266$) can be estimated as:

$$\delta u^* = \frac{R}{\sqrt{2g}} \frac{N}{\sqrt{H_{gr}}} \left(\frac{\delta N}{N} + \frac{1}{2} \frac{\delta H_{gr}}{H_{gr}} \right) = 0.0014 \tag{3.15}$$

that leads to $\delta u^*/u^* = 0.5\%$.

The wheel tangential speed was normalized to the term $\sqrt{2gH_{gr}}$, in order to make the results applicable in a general case and to consider the whole hydraulic conditions.

Considering flow rates $Q > 0.03$ m^3/s for the cases with the sluice gate, the normalized tangential speeds are approximately included in the range $u^* = 0.3 \div 0.4$. For a certain flow rate, these values are almost constant at different sluice gate openings; instead they slightly increase with the flow rate (at a constant sluice gate opening). This means that the optimal tangential speed is mainly affected by the square root of the head difference. The higher the flow rate, the higher the upstream water depth and the hydraulic head, thus the higher the required rotational speed for the optimal efficiency. Instead, for the weir it was obtained $u^* = 0.16 \div 0.4$; the height of the weir affects noticeably u^* (anyway, from Fig.3.9, the efficiency was not strongly affected by the wheel velocity, thus the efficiency at the optimal speed is not so higher than the efficiency at different wheel speeds).

The last examined parameter is the filling ratio, defined as the ratio of the water volume inside the bucket to the bucket volume; the bucket volume is delimited by two blades, the root of the blades and the channel bed. Table 3.3 reports the filling ratio of the buckets at the highest efficiency for each inflow case and flow rate.

Table 3.3. Filling ratio at the optimal efficiency for each inflow case and flow rate.

Inflow case (m)	Q (m^3/s)								
	0.02	0.03	0.04	0.05	0.06	0.07	0.08	0.09	0.10
a =0.05	0.72	0.31	-	0.28	0.29	0.31	0.33	-	-
a =0.075	0.45	0.38	0.33	0.32	0.32	0.39	0.34	0.37	0.47
a =0.1	0.46	0.32	0.32	0.33	0.33	0.42	0.43	0.51	0.53
a =0.125	0.40	0.37	0.32	0.40	0.35	0.40	0.41	0.53	0.55
a =0.15	-	0.32	0.32	0.36	0.38	0.44	0.46	0.55	0.49
h_s =0.18	0.40	0.24	0.27	0.32	0.57	0.59	0.62	-	-
h_s =0.28	0.29	0.30	0.45	0.24	0.28	0.33	-	-	-

The optimal filling ratio is included in the range $0.3 \div 0.45$ for the sluice gate and $0.27 \div 0.6$ for the weir. In a practical application, Tab.3.3 can be used to determine the width of the wheel, which should ensure that the optimal filling ratio is respected, while ensuring a water depth in the buckets higher than the tailrace water depth, avoiding adverse hydrostatic forces. When these tables are used in practical applications for similar wheels, the actual flow rate and inflow

dimensions have to be scaled in Froude similarity to the conditions investigated in this work.

3.2 Theoretical model

Scope of the present section is to elaborate a theoretical model able to estimate the power losses inside the wheel, in order to determine the efficiency. This is justified by the fact that during the centuries, theoretical models were developed separately from experimental tests, thus they were not validated, and not all the power losses were generally considered. Therefore, in the following sections, the power losses will be estimated, determining the efficiency and the power output for different hydraulic conditions. The predicted power output will be then compared with the experimental one.

3.2.1 General theory

The breastshot water wheel depicted in Fig. 3.15 is considered; the diameter of the wheel is D, the width is b, the number of blades is n and the angular distance between two blades is $\beta = 2\pi/n$. In Fig. 3.15 the localization of the power losses L is also illustrated.

The angle θ is the angular position of the gravity center of each bucket; it is the angle between the line linking the gravity center with the axle of the wheel, and the horizontal. When the downstream blade of the bucket is under the rotation axle, the corresponding configuration can be called *final position* f. The rotational speed of the wheel is N. The wheel is installed inside an open channel; the sluice gate increases the water depth in the conveying channel upstream of it, enhancing the water velocity to the wheel in the headrace. In the conveying channel the flow velocity is v_u and v_c is the contracted velocity after the sluice gate. The water flows into the wheel at velocity v_e and moves then with the buckets at a tangential velocity which is function of N; the tailrace velocity is v_d. The theoretical model supposes the flow field in the wheel and in the channels to be one-dimensional and the water in the buckets to be at rest, with an horizontal free surface. As it will be shown in the numerical results, the water volume in the buckets oscillates. Nevertheless, the rest water (relative to the bucket motion) assumption is suggested to approach theoretically the problem.

The gross head available to the wheel depends on the geometric and hydraulic boundary conditions and it is expressible by eq.3.1. The power input for the laboratory hydroelectric plant is defined as:

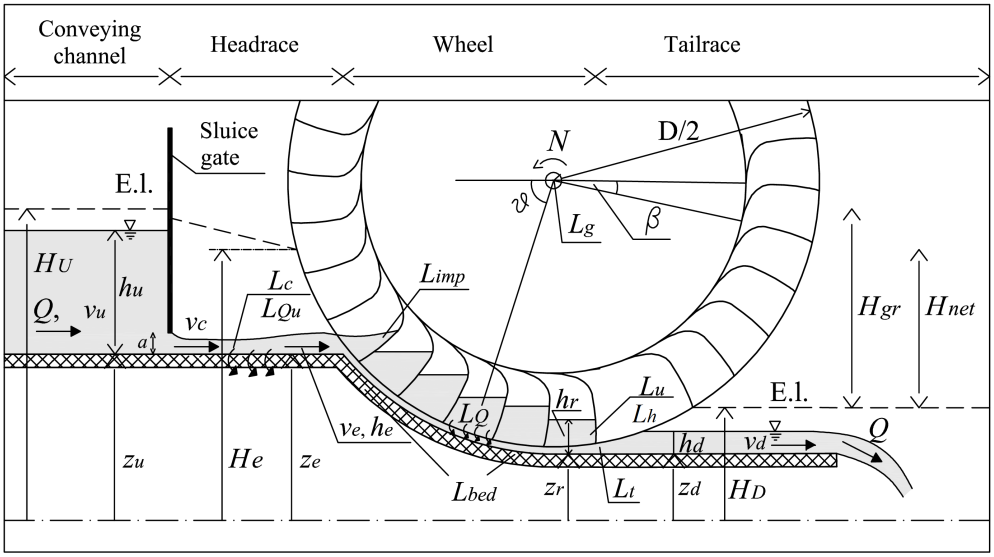

Fig. 3.15. General scheme of the breastshot wheel and power losses (L): L_c, L_u and L_h are the hydraulic losses, L_{Q_U} and L_Q the volumetric and leakage losses, L_{imp} and L_t the impact losses and L_g and L_{bed} the friction losses. Q is the flow rate, v_c the contracted velocity under the sluice gate and v_e the flow velocity just before the wheel. $H_{gr} = H_U - H_D$ is the gross head and H_{net} the net head available to the wheel. The wheel rotational speed is N. E.l. is the energy line.

$$P_{gr} = \rho g \cdot Q \cdot H_{gr} \tag{3.16}$$

where Q is the total flow rate and $\rho = 1000$ kg/m^3 is the density of water.

In general, the net head H_{net} available to the wheel is lower than the gross head H_{gr}, as a consequence of friction bed, turbulent losses and local energy losses in the headrace. For example, when the conveying channel is larger than the width of the sluice gate, lateral stream contractions may arise in the headrace, determining an increase in vorticity, friction bed and turbulence, as it occurs in the examined case. We call these power losses L_c; their effect is the reduction of the energy head from H_U to H_e (H_e is the flow energy head just upstream of the wheel).

Therefore, the net head available to the wheel is:

$$H_{net} = H_{gr} - (H_U - H_e) = H_e - H_D \tag{3.17}$$

and, considering also possible volumetric losses in the headrace, the power

input P_{net} for the wheel is calculated by:

$$P_{net} = \rho g \cdot Q_{net} \cdot H_{net} \tag{3.18}$$

where $Q_{net} = Q - Q_U$ and Q_U is the flow rate which is lost between upstream of the wheel, as a consequence of leakages through the gaps. We call this volumetric power loss L_{Q_U} (see section 4.2.2.3).

The mechanical power output P_{out} at the shaft of the wheel is lower than P_{net}, because additional *power losses* occur in the wheel, thus not the entirety of P_{net} is exploitable as useful work (Fig. 3.15). Four main kinds of power losses may occur in the wheel: $impact\ losses$ (1) include the impact of the entry water on the blades (L_{imp}) and the impact of the blades on the tailrace (L_t), $leakage\ losses$ (2) include water losses through the gaps between the buckets and the channel (L_Q), $friction\ losses$ (3) are due to mechanical friction at the bearings (L_g) and to drag effect of the water (contained in the buckets) on the channel bed (L_{bed}) and further *hydraulic losses* (4) may occur when the blades uplift water downstream (L_u). The buoyancy force on the blades is neglected in our case, since the steel blades are very thin.

The power output P_{out} can be expressed by:

$$P_{out} = P_{net} - L_{imp} - L_Q - L_g - L_{bed} - L_t - L_u \tag{3.19}$$

where

$$P_{net} = P_{gr} - L_c - L_{Q_U} \tag{3.20}$$

with L_c and L_{Q_U} the hydraulic and leakage losses in the headrace between the sluice gate and the wheel, respectively.

The wheel efficiency η_w is defined as:

$$\eta_w = \frac{P_{out}}{P_{net}} = 1 - \frac{(L_{imp} + L_Q + L_g + L_{bed} + L_t + L_u)}{P_{net}} \tag{3.21}$$

The conveying channel efficiency is defined as η_c:

$$\eta_c = \frac{P_{net}}{P_{gr}} = 1 - \frac{(L_c + L_{Q_U})}{P_{gr}} \tag{3.22}$$

The global efficiency of the installed hydroelectric plant is defined as η:

$$\eta = \eta_c \cdot \eta_w = \frac{P_{out}}{P_{gr}} = 1 - \frac{(L_c + L_{Q_U} + L_{imp} + L_Q + L_g + L_{bed} + L_t + L_u)}{P_{gr}} \tag{3.23}$$

3.2.2 Power losses estimation

The scope of the following sections is to explain in detail the power losses which may generally occur in a breastshot water wheel. A wide and complete overview on the exchanging power mechanism between the water and the wheel is also presented, in order to facilitate the reader in the understanding and interpretation of some historic models found in literature (section 4.2.3). In the following sections the rotational speed of the wheel will be expressed in rad/s.

3.2.2.1 Impact losses

Impact losses are due to the impact of the entry water against the blades (L_{imp}) and to the impact of the blades against the tailrace (L_t).

The latter kind of impact loss (L_t) is the simplest to analyze. In order to quantify it, the method used to calculate the drag force of immersed moving bodies is used. In this case the body is the blade with the water volume in the bucket, that is assumed to be a flat plat normal to the flow. Hence L_t can be expressed by:

$$L_t = \frac{1}{2} C_d \rho A_d (u_m - v_d)^2 u_m \tag{3.24}$$

where $C_d \simeq 2$ is the drag coefficient (flat plate normal to water flow), $A_d = b \cdot h_d$ is the downstream wet area, u_m is the mean wet blade tangential speed (the tangential speed at the center of the wet blade), v_d is the flow velocity in the downstream canal. L_t occurs if the blades are submerged in the tailrace and $u_m > v_d$, as well as $h_d > h_r$ (h_r is the water depth in the bucket).

In order to solve eq.3.24, the water depth of the tailrace in correspondence of the blade which is in the final position needs to be know, while the water depth in the buckets can be calculated knowing its water volume and the bucket geometry. In this work we assume that the water depth in the channel downstream of the wheel is constant (the channel slope is zero), and equal to the water depth measured at the end of the tailrace.

The second kind of impact loss (L_{imp}) is the impact between the water flow

and the blades. Referring to Fig. 3.16, at step 1 the flow fills into the bucket and it provides a pressure on blade 1; while the wheel continues its rotation, blade 1 reaches the position represented at step 2 and the pressure profile on it changes. When at step 3, after a time $T = \frac{\beta}{N}$ blade 2 reaches the same position of blade 1 at step 1, the cycle restarts.

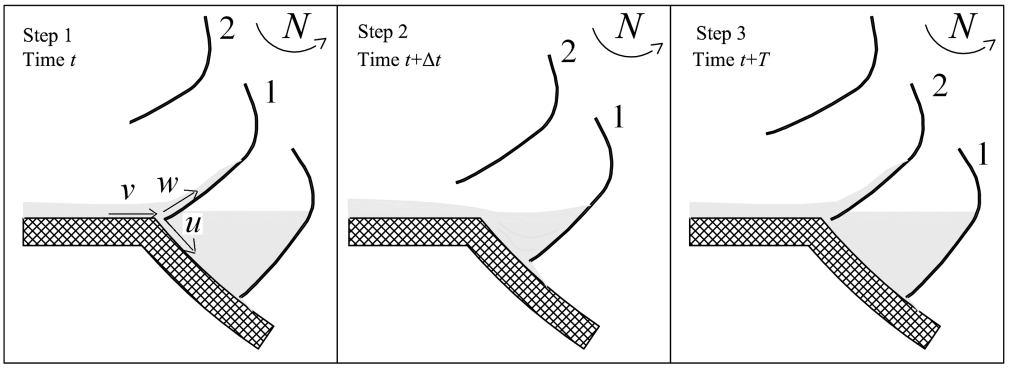

Fig. 3.16. The figure focuses the attention on three blades of the wheel; observing blade 1 and blade 2, after $T = \beta/N$ s, the impact conditions change and repeat.

The power exchanged between the flow and the blade, as well as the blade reaction force (which provides the torque at the shaft), are not simple to estimate. The blade reaction force depends on the total pressure the water exerts on the blade surface, due to the running up and impact effects; the process is affected by the hydraulics (velocity, turbulence) and the geometric configuration. The accumulated water volume in the bucket has a dissipative effect, dissipating the kinetic energy of the flow: in step 1, when the bucket is empty, the kinetic impact torque is bigger than that provided in step 2. This aspect will be further investigated in section 3.4. When the filling process completes, the torque is totally due to the water weight and, when the final position is reached, the buckets empty.

Called $\vec{w} = \vec{v} - \vec{u}$ the relative velocity of the flow with respect to the moving blade, the impact loss can be expressed considering that a portion of the relative kinetic energy is dissipated, which is a common approach used in turbomachines.

$$L_{imp} = \xi \rho g \cdot Q \left(\frac{w^2}{2g} \right) \tag{3.25}$$

where ξ is a coefficient to determine between 0 and 1. Due to the fact that the impact conditions change during rotation (the blade changes its orientation, the water volume cumulates in the bucket, etc.) ξ is not constant during T. The

average value of ξ will be determined by an optimization process applying the theoretical model on experimental data, considering the situation with the blade in correspondence of the water entry point.

3.2.2.2 Friction losses

Friction losses are related to power dissipation by friction forces, both at the supports of the shaft, due to the wheel weight, and on the channel bed, due to the drag effect of the water which is contained in the buckets, that move from upstream to downstream.

The power loss due to the friction at the bearings can be expressed by considering the friction force between the shaft and the wheel that weighs on it:

$$L_g = M \cdot N = W \cdot f \cdot r \cdot N \tag{3.26}$$

where M is the opposing torque due to friction, N the rotational speed of the wheel (rad/s), $W = W_{wh} + W_{ww}$ the weight of the wheel and the weight of the water inside the buckets (that pushes downward on the blades), respectively, f the friction coefficient (0.0015, ball bearings) and r the shaft level arm (0.075 m).

The friction loss L_{bed} is due to the drag effect of the water contained in the moving buckets on the channel bed. The power loss can be expressed by means of the Chezy formulation:

$$L_{bed} = \rho g \cdot Q \cdot H_{loss} = \rho g \cdot Q \cdot \left[\frac{u^2}{{\chi_C}^2 \cdot R_h} \cdot l_{bed} \right] \tag{3.27}$$

where χ_C is the Chezy coefficient, Citrini and Noseda, 2012 (depending on the roughness of the bed surface and on the average hydraulic radius R_h of the water in the buckets) and l_{bed} is the length of the channel bed from the water entry point until the point where the blade exits the water flow downstream.

3.2.2.3 Volumetric and leakage losses

Volumetric losses happen when water is lost through the gaps. The volumetric power losses in the headrace are called L_{Q_U} (eq.4.8); the power loss due to the water flowing through the gaps between the wheel and the channel bed, when the water is already inside the buckets, is called L_Q. These gaps are necessary to avoid any contact and friction between the wheel and the bed of the channel.

The power losses L_{Q_U} occur just upstream of the wheel. They affect the effi-

ciency of the total installation and not directly that of the wheel. The power losses L_{Q_U} can be expresses by:

$$L_{Q_U} = \rho g \cdot Q_U \cdot (H_Q - H_D) \tag{3.28}$$

where Q_U is the water which is lost, H_Q is the energy head of Q_U (in this case $H_Q = H_e$) and H_D the downstream one (see Fig. 3.15); Q_U can be measured or estimated once the gaps geometry and the hydraulic conditions are known (by assuming the velocity of the flow entering into the gap is the same of the velocity in the headrace).

The other leakage losses occur through the gaps inside the wheel (during rotation), and they affect directly the estimation of the wheel efficiency. The blades are fixed to the lateral shrouds and the water volume is confined between two consecutive blades and the lateral shrouds (the shrouds rotate inside the curb). Therefore, a portion of water (Q_l) exits from the buckets through the lateral gaps between the shrouds and the channel bed, and a portion (Q_f) through the gaps between the blades and the bed of the channel (Fig. 3.17 and Fig. 3.18). The total gap flow is $Q_{gap} = Q_l + Q_f$ In the estimation of L_Q, it is essential to underline that the positions of a bucket at time t and $t+T$ can be interpreted as the positions of two adjacent buckets at time t.

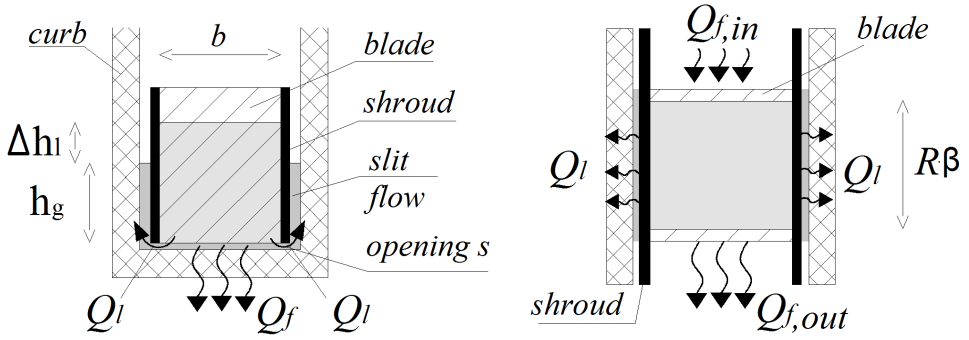

(a) *Transversal section.* (b) *Plan view.*

Fig. 3.17. The figure depicts the water exiting/entering from/into a bucket. The arrows represent the direction of the outflow; Q_l exits the bucket through the lateral gaps between the shrouds and the channel bed and Q_f through the gaps between the blades and the bed of the channel. In the experimental wheel, the gap was s=0.01 m wide.

The outflow Q_f depends on the water level difference Δh_f between two adjacent buckets (Fig. 4.3) and Q_l depends on the difference of energy head Δh_l between the water in the buckets and the receiving *slit flow*: the slit flow is the water flow which is already running through the gaps between the two lateral shrouds of the wheel and the lateral walls (Fig. 3.17).

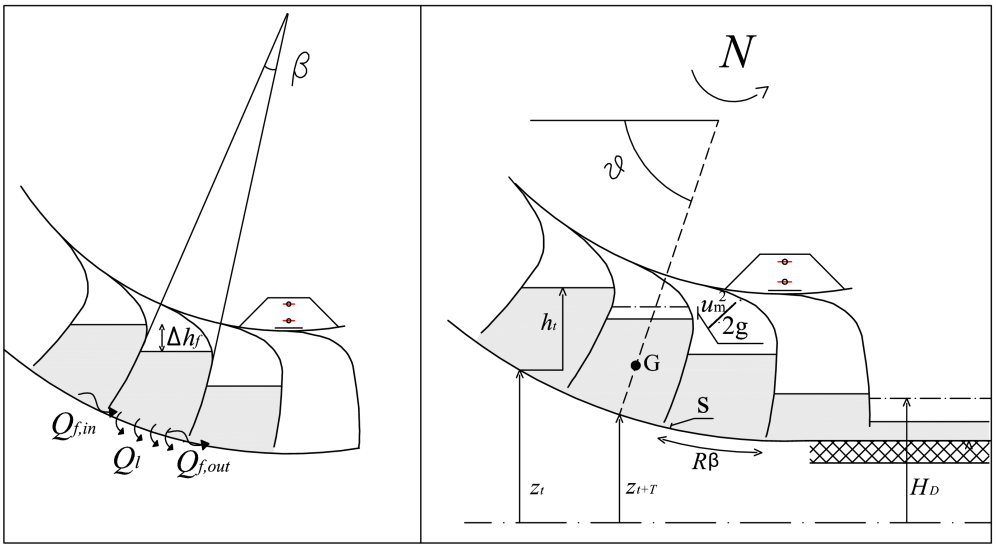

Fig. 3.18. The figure depicts the outflows Q_f and Q_l from the buckets. The point G is the center of gravity of each bucket and Δh_f the water level difference used to calculate Q_f. The hydraulic head of the water inside the generic bucket is $H_t = z_t + h_t + {u_m}^2/2g$, where u_m is the mean tangential velocity of the water in the bucket.

The equation used to estimate Q_f is the sluice gate equation:

$$Q_f = C_v A_f \sigma \sqrt{\frac{2g\Delta h_f}{1 + \sigma \frac{s}{\Delta h_f}}} \tag{3.29}$$

where $C_v \simeq 0.98$ is the velocity coefficient, σ is the efflux coefficient (σ is 0.61 when $s/\Delta h_f$ approaches zero), $A_f = s \cdot b$ is the section of the gap through which the leakages occur (with s the height of the opening and b its width, Fig. 3.17 and Fig. 3.18) and Δh_f is the water level difference between the buckets. In each bucket there is an outflow $Q_{f,out}$ and an inflow $Q_{f,in}$.

The instantaneous energy loss dE_{Qf} at time t for a generic bucket i is expressible by eq. 3.30:

$$dE_{Qf} = \rho g \cdot Q_f \frac{d\theta}{N} \cdot (H_i - H_D) = \rho g \cdot (Q_{f,out} - Q_{f,in}) \frac{d\theta}{N} \cdot (H_i - H_D) \tag{3.30}$$

where $Q_f \frac{d\theta}{N}$ is the water volume which is globally lost from the bucket i during the infinitesimal time $dt = d\theta/N$, with θ the angular coordinate of the bucket and

H_i the energy head of the water inside it. The outflow Q_f for a bucket at time t is an inflow at the same time t for bucket $i+1$, or at time $t+T$ for the same bucket i.

The equation used to estimate Q_l is again:

$$Q_l = 2 \cdot C_v A_l \sigma \sqrt{\frac{2g\Delta h_l}{1+\sigma\frac{s}{\Delta h_l}}} \tag{3.31}$$

where Δh_l is the energy head difference between the water in the buckets and the *slit flow* and $A_l = s \cdot (R \cdot \beta)$ is the area of a lateral gaps. The water which is lost does not re-enter into the next bucket, but begins to flow in the gap. However, if in some points the energy head of the gap flow is bigger than the energy head of the water in the respective buckets, Q_l re-enters into them, becoming an inflow. The hydraulics of the slit flow is not uniform; it is unsteady and it is affected by the outflowing process of Q_l. Therefore, its energy head, which depends on its water level and velocity, is not simple to determine. For the sake of simplicity, the slit flow is assumed to be composed of two parts; the lowest layer of the flow, which flows on the channel bed and against which Q_l impacts, with an height s (the same of the opening through which Q_l exits the bucket, eq. 3.31) and a velocity $u = NR$; over the previous layer, the flow is with an height h_g to be determined (Fig. 3.17). This part is also considered to be locally uniform and its energy slope equal to the bed slope in each point of the channel. With these hypothesis, the slit flow velocity, its water level h_s and the energy head difference can be calculated; $\Delta h_l = h_g + s - h$, where h is the water level in the considered bucket.

The infinitesimal energy loss dE_{Ql} at time t for the generic bucket i can be expressed by:

$$dE_{Ql} = \rho g \cdot Q_l \frac{d\theta}{N} \cdot (H_i - H_D) \tag{3.32}$$

where $Q_l < 0$ if it enters into the buckets.

Finally, the mean value of L_Q during the period T is:

$$L_Q = \frac{\int_t^{t+T} \sum_{i=1}^{n_b} dE_{Ql} + dE_{Qf}}{T} = \frac{\int_{\theta_s}^{\theta_e} [(Q_f + Q_l) \cdot (H_i - H_D)] \cdot \rho g \cdot \frac{d\theta}{N}}{\beta/N} \tag{3.33}$$

where θ_s is the position where the bucket finishes his filling process, θ_e that where the bucket passes under the rotation axle and n_b the number of the filled buckets.

3.2.2.4 Hydraulic losses

Hydraulic losses occur as a consequence of the power losses during the transformations between the kinetic and the potential/pressure energy, or vice-versa, of the flow. Hydraulic losses include also the impact losses of the entry water against the blades; because of their bigger complexity, the impact losses have been explained separately in section 3.2.2.1.

The hydraulic loss L_c is due to friction bed and turbulent dissipation in the headrace; the energy head reduces from H_U to H_e. In our investigated case, the hydraulic jump after the sluice gate determines power losses and a further increase in turbulence.

Therefore, the estimated power loss L_c is:

$$L_c = \rho g \cdot Q \cdot (H_U - H_e) \tag{3.34}$$

where $H_e = z_e + h_e + \frac{{v_e}^2}{2g}$. In our case, the water level h_e was measured and the velocity estimated as $v_e = Q/(h_e \cdot B)$.

The last hydraulic loss is L_h, and it occurs downstream. After the water has filled the buckets, the water volume in the bucket is carried to the outlet and its free surface loses elevation; therefore, a water depth difference arises between two consecutive buckets, generating the hydrostatic force which pushes against the blade and which drives the wheel. In this case, the sum of the water depth differences equals the drop in the channel bed elevation, thus $H_g = \sum_i \Delta h_{r,i}$ where $\Delta h_{r,i}$ is the difference in water elevation in correspondence of each active blade i. The power generated by each hydrostatic force equals the term $\rho g Q \Delta h_{r,i}$, with $\gamma = 9810$ N/m^3. This is the way through which the power input due to the geometric head difference (the channel drop) is transferred to the wheel. In addition to these hydrostatic forces, there are two additional hydrostatic forces: one in correspondence of the first blade (due to the water level difference between the first filled bucket and the headrace) and the second in correspondence of the last blade (due to the water level difference between the tailrace and the last filled bucket).

For example, consider a difference $\Delta h_{r,f}$ between the water level in the tailrace and the water level in the last bucket, when the downstream blade of the bucket is under the rotation axle. This configuration can be called *final position* f. When $\Delta h_{r,f} < 0$, the free surface at the tailrace is lower than that in the last bucket; in this condition, the water in the bucket continues to push the blade, although there is not a drop in the channel bed elevation. Therefore, the energy difference between the water in the last bucket and the tailrace is still employed to

push the wheel. The contrary occurs when $\Delta h_{r,f} > 0$, which represents a power loss. This situation sometimes occurs when the flow is regulated downstream by a weir, through which a fixed water depth in the tailrace is imposed. Furthermore, when $\Delta h_{r,f} > 0$, the downstream water velocity is lower than the wheel velocity, and additional power losses due to the impact of the blades against the tailrace has to be considered, as discussed in section 3.2.2.1. However, these hydrostatic forces have not to be considered, since they are already implicitly included in eq.3.22 and eq.3.23. Indeed, in eq.3.22 and eq.3.23, we have considered not only the geometric head difference H_g, but the hydraulic head H_{net}. The power input associated to H_g is transferred to the wheel by the hydrostatic force between the filled buckets, as explained before. The additional power input associated to the difference between the hydraulic head and the geometric one, is transferred to the wheel (or subtracted when it represents a power loss) by the hydrostatic forces generated in on the first and final blade, as previously explained. Therefore, using the hydraulic head, the model is already considering the hydrostatic force on the first and final blades.

Anyway, $\Delta h_{r,f}$ is not constant during T, because it is zero when the bucket exits the tailrace. We assume that $\Delta h_{r,f}$ varies from $\Delta h_{r,f}$ to zero during T linearly. With this assumption, during T, the average head difference that pushes against the considered blade is $\Delta h_{r,f}/2$. Therefore, the other portion $\Delta h_{r,f}/2$ is a power loss, due to the emptying of the bucket. As a consequence, the power loss to consider is:

$$L_h = \rho g Q_f \frac{\Delta h_{r,f}}{2} \tag{3.35}$$

Finally, further power losses may be related to the residual water which is uplift by the blades over the water surface at the tailrace (L_u); in the present case the blades are shaped in order to avoid L_u, thus they are considered negligible.

3.2.3 Interpretation of past formulations

In the past, other scientists proposed theoretical models to estimate the power output of breastshot water wheels. Some of them proposed quite detailed formulations with power losses estimation (Chaudy, 1896 and Garuffa, 1897); these expressions can be generally adopted to different cases. Other scientists proposed shorter and easier formulations (Morin and Morris, 1843 ; Church, 1914), using empirical correction factors applied to experimental results; these laws are generally too much approximated if used outside of their experimentation hydraulic range. In this section, these formulations are reinterpreted and compared to the

general theory previously exposed.

In 1843 *Morin* made experiments on different breastshot wheels and summarized his results in eq.3.36:

$$P_{out,M} = \delta \cdot \rho g \cdot Q \cdot \left[\frac{(v_e \cdot cos\alpha - u)u}{g} + \Delta H_g \right] \tag{3.36}$$

finding as mean values $\delta = 0.77$ and $\delta = 0.8$ for breastshot wheels with inflow sluice gate or an inflow weir, respectively. The water depth difference is $\Delta H_g = (h_e + z_e) - (h_d + z_d)$ and α is the angle between the tangential wheel velocity u and the entry velocity v_e.

Five decades later, in 1896, *Chaudy* proposed eq.3.37:

$$P_{out,Ch} = P_{gr} - L_c - L_{imp} - L_{bed} \tag{3.37}$$

The terms on the right hand side of eq.3.37 are $L_c = 0.1 \cdot \rho g Q \frac{v_e^2}{2g}$, $L_{imp} = \rho g Q \frac{w^2}{2g}$ and $L_{bed} = \frac{u^2}{2g} \cdot 0.0016 \frac{\rho g Q l_{bed}(b+2h)}{b \cdot h}$, where b is the width of the wheel, h the mean water depth in the buckets and l_{bed} the channel length.

In general, eq.3.37 overestimates L_{imp} (the coefficient ξ was assumed equal to 1) and it has a lower level of detail respect to eq.3.19.

One year after, in 1897, *Garuffa* proposed the following equation:

$$P_{out,G} = P_{gr} - L_{imp} - L_g - L_{bed} - L_Q - L_t \tag{3.38}$$

The terms on the right hand side of eq.3.38 are $L_{imp} = (0.15)\rho g Q \frac{w^2}{2g}$ and $L_c = \frac{1}{4000} \cdot \rho l_{bed} p_{wet} u^3$ (the coefficient 1/4000 is for concrete channels, with p_{wet} the wet perimeter around the bucket). For T_t and T_g, tailrace and friction losses, *Garuffa* proposed the same formulations explained in section 3.2.2.1 for L_t and L_g (but with a friction coefficient of 1/16).

Garuffa did not validate eq.3.38 by means of experimental analyses, and four main appreciable differences arise in eq.3.38 with respect to the new proposed model. (1) *Garuffa* did not consider L_c and L_{Q_U} in the headrace, adopting $P_{gr} = P_{net}$. (2) Equation 3.38 underestimated L_{imp}, suggesting $\xi = 0.1 - 0.2$, or $\xi = 0.15$. Although in eq.3.38 the residual loss L_h is not considered (3), *Garuffa* said that some residual power losses at the tailrace could occur, but he did not estimate them. *Garuffa* proposed a simple method to evaluate T_Q (4): a thin water sheet has been supposed flowing through the gaps between the curb and the buckets, with a constant velocity w_q. Since at that time, in general, there were

not lateral shrouds fastened to the blades, the gap geometry was composed of a U transversal frontal section, with two vertical lateral gaps and one horizontal gap; the formers were located between the blades and the lateral curb and the latter between the buckets and the channel bed. With these assumptions, in the present case $Q_f = (2h_r + b)sw_q\phi$ and $Q_l = 0$, where h_r is the water level in the bucket downstream of the wheel, b the width of the buckets, s the gap opening and ϕ a resistance coefficient which may be taken as equal to one. The term $w_q = \sqrt{\frac{2g\Delta H_r}{m}}$ is the velocity of the slit flow Q_f; $\Delta H_r = (h_e + z_e) - (h_r + z_d)$ is the difference between the water level in the last bucket (under the rotation axle) and the water level just before the wheel, and $m = 1 + \frac{w_q - u}{R \cdot \beta} \cdot \frac{l_{bed}}{w_q}$ the number of blades which are interested to the slit flow in its relative flowing respect to the wheel. In our case, the shrouds are fastened to the blades and there is not a vertical gap between the blades and curb, but the gap is located between the shrouds and the curb (see fig.3.17a, where it is clear that the vertical gaps are between the shrouds and the curb). Therefore, to rearrange this formulation to our case, $h_r = 0$. *Garuffa* also reported a more sophisticated method proposed by other authors (Bach 1886), which is similar to that proposed in section 4.2.2.3.

Later, in 1914 *Church* (Church, 1914) expressed the power output by:

$$P_{out,C} = \rho g \cdot Q \cdot \left[\frac{(v_e \cdot cos\alpha - u)u}{g} + \delta \cdot \Delta H_g \right] \tag{3.39}$$

where δ is 0.93 if the space between the wheel and the curb is lower than $\simeq 1.2$ cm.

3.2.4 Theoretical results: errors of the different models

Scope of the theoretical model was the estimation of the power output of a breastshot water wheel. The power losses occurring during the wheel operation were modeled, with the aim of the estimation of the impact coefficient ξ in eq. 3.25 by an optimization process.

The global average error $\bar{er}$ among the experimental and theoretical powers is:

$$\bar{er} = \frac{1}{n_p} \sum_{j=1}^{n_p} er_j = \frac{1}{n_p} \sum_{j=1}^{n_p} \frac{|P_{out_j} - P_{exp_j}|}{P_{exp_j}} \tag{3.40}$$

where n_p is the total number of experiments, P_{exp} is the experimental power output and P_{out} the theoretical one. For each case, the value of ξ was determined in order to minimize $\bar{er}$; the average value corresponds to $\xi = 0.76$, with a stan-

dard deviation of 0.29. The average error is $e\bar{r}_1 = 19\%$ and if the cases of $Q = 0.02 \div 0.03$ m^3/s are excluded (which do not correspond to usual working conditions), $e\bar{r}_2 = 8.0\%$ (Fig. 3.19). The impact coefficient includes all the approximations, uncertainties, simplifications and not perfect assumptions of the model, such as the one dimensional approximation and the resting water inside the buckets. It is the only free parameter, hence it has to managed with care, and its obtained average value represents what happens in a general mean case. It can be used to estimate the impact power losses in geometrically similar water wheels. Unfortunately, the identified ξ value was determined experimentally, and it may not be valid for different sized water wheels. Anyway, it can still be considered reliable in water wheels whose blades are oriented parallel to the relative flow velocity in the impact point, and when the water flow enters into the wheel under the axle. The quantification of impact losses by the presented theoretical model may not be valid if the water entry point is close to the wheel axle. In this case, although the blades could be well designed, the level arm would approach zero, and the generated impact force would be used to compress the wheel onto the shaft, instead of generate torque.

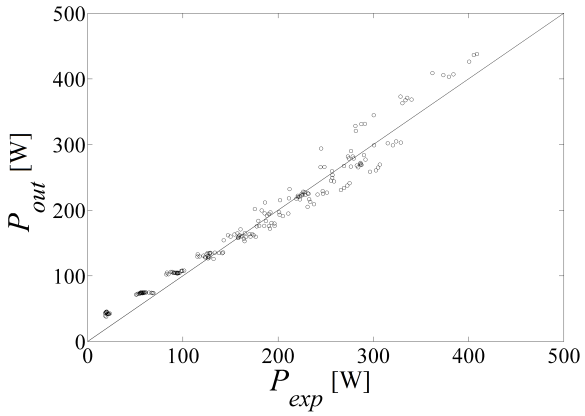

Fig. 3.19. The analytical calculated power versus the experimental one. The average error is 19%, which reduces to 8.0% if the cases where $Q < 0.03$ m^3/s are excluded.

The biggest errors occur at flow rates lower than 0.03 m^3/s, which do not correspond to usual working conditions, since the flow rate is too low. Indeed, such very low discharges are extreme and uncommon working conditions for this breastshot water wheel, that would be oversize. In these conditions, the slits dimension is comparable with the water depth in the buckets, thus the actual volumetric losses are higher with respect to the estimated ones.

Instead, concerning the past formulations, the errors $e\bar{r}$ are higher than the new presented model. *Morin* and *Church* equations (eq. 3.36 and eq. 3.39, respec-

tively), the simplest and shortest ones, fit the results well only for experimental power $100 < P_{exp} < 250$ W and $200 < P_{exp} < 300$ W, respectively (Fig. 4.15a and Fig. 4.15d).

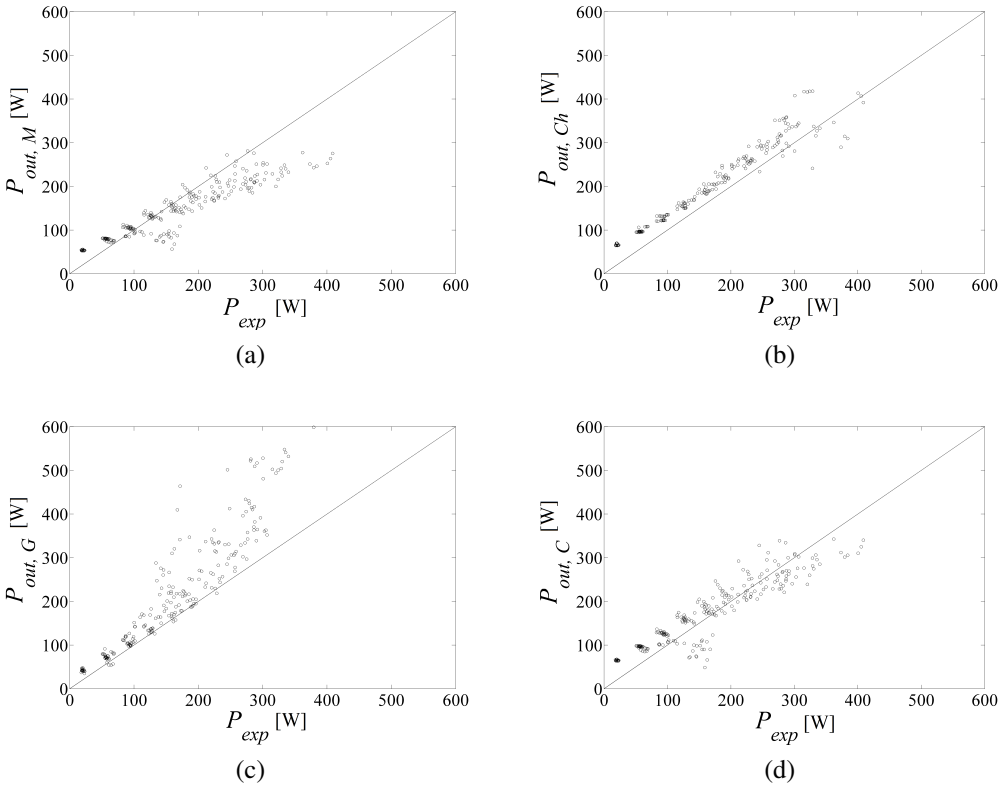

Fig. 3.20. The analytical power output versus the experimental one. *(a) Morin, (b) Chaudy, (c) Garuffa and (d) Church*. Average error $\bar{er}$: *(a)* 33%, *(b)* 49%, *(c)* 38% and *(d)* 42%. Average error excluding flow rates lower than 0.03 m^3/s: *(a)* 18%, *(b)* 25%, *(c)* 32% and *(d)* 19%.

Chaudy equation (eq. 3.37) always overestimates the power output, since it neglects several kinds of power losses (Fig. 4.15b), while *Garuffa* equation (eq. 3.38) gives good results for $P_{exp} < 250$ W (Fig. 4.15c). The formulation proposed by *Garuffa* underestimates L_{imp} and overestimates slightly L_Q with respect our theoretical model, and it does not include all the possible power losses, included those in the headrace. The average errors $\bar{er}$ are 33% *(Morin)*, 49% *(Chaudy)*, 38% *(Garuffa)* and 42% *(Church)*. The average errors excluding the flow rates lower than 0.03 m^3/s become 18% *(Morin)*, 25% *(Chaudy)*, 32% *(Garuffa)* and 19% *(Church)* (Tab. 3.4).

Table 3.4. Global average errors between the power output estimated by the theoretical equations and the measured experimental one. er_2 is calculated excluding flow rates lower than 0.03 m^3/s.

Author	er_1 [%]	er_2 [%]
Morin, 1843	33	18
Chaudy, 1896	49	25
Garuffa, 1897	38	32
Church, 1914	42	19
Present work	19	8

3.2.5 Theoretical results: power losses

With the goal of giving a wider overview on the wheel behavior, in Tab. 3.5 some theoretical results (power output and power losses (eq.3.19) are shown.

In general, the higher the flow rate Q the bigger the power losses, since a larger amount of flow rate is lost. The increase of the entry flow velocity (with Q and N constant) enhances L_{imp} and L_c, without affecting appreciably the other power losses. These are quite intuitive results, since power losses increase with the turbulence intensity and the energy of the flow. The increase in the wheel rotational speed (with v_c and Q constant) enlarges L_{imp}, L_g and L_{bed}. The higher the rotational speed, the higher the friction effects at the shaft's supports and on the channel bed, and the more difficult for the entry flow to perform useful work on the blade, since it has to chase the blade. L_{bed} is always negligible, because it is two orders lower than other terms (and it increases with N and Q). A quite interesting result is depicted in Fig. 3.21, where the leakage losses L_Q are plotted versus the rotational speed of the wheel. Predicted leakage losses are almost constant with N and Q and they seem to increase for very low rotational velocities.

The highest predicted power losses in absolute terms are $L_c = 192$ W for $a = 0.05$ m and $Q = 0.08$ m^3/s, and $L_{imp} = 119$ W for $a = 0.05$ m, $N = 0.8$ rad/s and $Q = 0.08$ m^3/s (the highest investigated flow rate for $a = 0.05$ m). If compared with the accuracy of the measurements (the power accuracy depends mainly on the torque transducer accuracy that is $\pm$6 Nm), it is possible to claim that the previous values are not significantly affected by the accuracy of the measurements. These results show that the critical points for breastshot water wheels are the upstream power losses. Similar results will be also confirmed in section 5 for *Sagebien* and *Zuppinger* wheels.

Normalizing the power losses with the power input, L_{imp}/P_{net} increases with

Table 3.5. Investigated conditions, with the measured and calculated mechanical power output (P_{exp} and P_{out}), experimental efficiency (η_{exp}) and the theoretical results for some selected cases; the table shows a wide overview on different experimented cases.

Q [m^3/s]	N [rad/s]	P_{exp} [W]	P_{out} [W]	L_c [W]	L_{Q_U} [W]	L_{imp} [W]	L_Q [W]	L_{bed} [W]	$L_t + L_u$ [W]	L_g [W]	η_{exp} [-]
(1)	(2)	(3)	(4)	(5)	(6)	(7)	(8)	(9)	(10)	(11)	(12)
0.04	0.4	87	107	10	4	9	20	0.1	0.0	0.06	0.57
0.04	0.8	99	110	10	4	7	19	0.4	0.0	0.12	0.65
0.04	0.4	85	103	0	3	11	20	0.0	0.0	0.06	0.59
0.04	0.7	96	107	0	4	8	19	0.4	0.0	0.12	0.67
0.06	0.5	147	162	6	5	15	20	0.1	0.0	0.08	0.68
0.06	1.0	161	162	6	5	15	19	0.8	0.0	0.16	0.74
0.06	0.6	186	201	81	9	86	18	0.1	0.0	0.10	0.47
0.06	1.2	225	217	80	9	65	19	1.3	0.0	0.19	0.57
0.07	0.8	187	186	19	6	16	20	0.4	0.0	0.13	0.73
0.07	1.1	191	176	19	6	25	20	1.1	0.0	0.18	0.74
0.07	0.9	192	200	7	6	14	20	0.7	0.0	0.15	0.74
0.07	1.1	188	195	7	6	19	20	1.1	0.0	0.18	0.72
0.08	1.0	229	226	9	7	17	20	0.9	0.0	0.16	0.77
0.08	1.2	223	219	8	7	24	20	1.4	0.0	0.19	0.76
0.08	1.0	274	270	59	10	107	18	0.7	0.0	0.16	0.58
0.08	0.7	249	253	59	10	123	18	0.2	0.0	0.11	0.53
0.10	1.0	290	286	44	10	26	19	0.9	0.0	0.17	0.72
0.10	1.3	287	273	45	10	38	19	1.8	0.0	0.21	0.71
0.10	0.8	301	292	132	12	76	18	0.3	0.0	0.13	0.56
0.10	1.3	324	301	133	12	65	18	1.6	0.58	0.20	0.60

Q and N and L_c/P_{gr} increases with Q and v_c, as explained before. L_g/P_{net} and L_h/P_{net} increase with N, while L_t/P_{net} is important only at high N ($N > 1.25$ rad/s), due to the fact that, at slow rotational speeds, the tangential velocity of the blade is smaller than that of the tailrace. However, L_g is negligible, as observed in Tab.3.6. The biggest dimensionless power losses are $L_Q/P_{net} = 0.32$ (which occurs at low flow rates, when the dimension of the gaps is comparable with the water depth in the headrace and in the buckets), and $L_{imp}/P_{net} = 0.50$ (for the highest entry velocity). Tab. 3.6 summarizes the magnitude of the power losses, showing the minimum, average and maximum value of each power loss with respect to the power input.

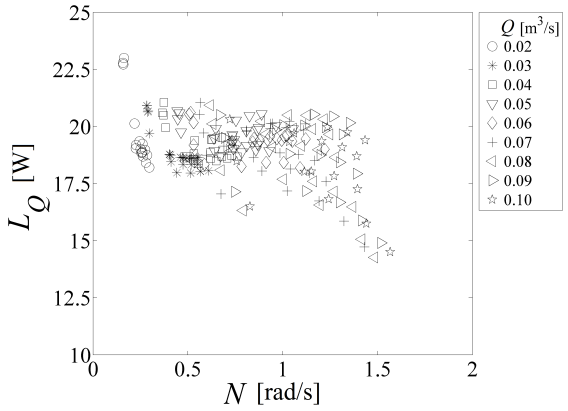

Fig. 3.21. The leakage losses L_Q during wheel rotation at different flow rates Q and wheel rotational speeds N.

Table 3.6. Minimum, average and maximum values of the power losses. L_{imp}, L_Q, L_g, L_{bed}, $L_t + L_u$ are normalized to P_{net} (since they occur inside the wheel), while L_{Q_U} and L_c are normalized to P_{gr}. The maximum normalized value of L_Q refers to a working situation (very low flow rate) out of the operative conditions, thus it is very large.

	L_{imp}	L_{Q_U}	L_Q	L_g	L_{bed}	$L_t + L_u$	L_c
Min [%]	0	1.8	2	0	0	0	0
Average [%]	13.5	2	11	0.07	0.6	1.1	8
Max [%]	50	2.5	32	0.15	2	14	26

3.3 Dimensional analysis

The scope of this section is to develop a dimensionless predictive law for breastshot water wheels (which are geometrically similar to the tested wheel), in order to predict the maximum power output.

3.3.1 Dimensional analysis procedure

The power generated at the shaft of the wheel is mainly due to the hydrostatic pressure exerted by the water on the blades; a smaller contribution is also provided by the kinetic energy exchanged between the flow and the blades during the impact. The mechanical power output (P_{out}) produced by the wheel depends on the wheel and channel geometry and on the hydraulics. It is a function of the flow

rate (Q), the flow velocity upstream of the wheel (v_e) (which depends on the sluice gate opening and flow rate), the wheel tangential velocity (u), the geometric head (H_g), the channel width (B), water density (ρ) and water dynamic viscosity (μ):

$$P_{out} = f(Q, a, v_e, u, H_g, B, \rho, \mu) \tag{3.41}$$

Using Q, ρ and H_g as independent variables, the dimensional analysis applied to Eq. 3.41 leads to:

$$\frac{P_{out} {H_g}^4}{\rho Q^3} = f\left(\frac{a}{H_g}, \frac{\mu H_g}{\rho Q}, \frac{v_e {H_g}^2}{Q}, \frac{u {H_g}^2}{Q}, \frac{B}{H_g}\right) \tag{3.42}$$

Since in the present case the term B/H_g is constant, it is possible to exclude it from Eq. 3.42. Equation 3.42 then becomes:

$$\frac{P_{out} {H_g}^4}{\rho Q^3} = f\left(\frac{a}{H_g}, \frac{\mu H_g}{\rho Q}, \frac{v_e {H_g}^2}{Q}, \frac{u {H_g}^2}{Q}\right) \tag{3.43}$$

which is valid for channels with similar values of B/H_g. Therefore, Eq. 3.43 can be expressed using Ne, G, Re, V_e and U, which are five dimensionless numbers with a specific physical meaning.

The first term is the Newton number *Ne* and it is the ratio of the pressure to the product of fluid density and squared velocity. It represents the dimensionless mechanical power output and it is expressed by:

$$Ne = \frac{P {H_g}^4}{\rho Q^3} \tag{3.44}$$

The second term is a geometric similarity number G:

$$G = \frac{a}{H_g} \tag{3.45}$$

This geometric number is defined as the ratio of the opening of the sluice gate to the (geometric head) and it gives information on the dimension of the depth of the water stream before entering into the wheel, with respect to the geometric head difference.

The third parameter in eq.3.43 is the inverse of the Reynolds number, that is the ratio of inertial forces to viscous forces.

$$Re = \frac{\rho Q}{\mu H_g} \tag{3.46}$$

The last two terms are flow rate numbers expressed by (Logan, 2003):

$$U = \frac{u {H_g}^2}{Q} \tag{3.47}$$

$$V_e = \frac{v_e {H_g}^2}{Q} \tag{3.48}$$

Here, the flow rate numbers are defined as the ratio entry flow velocity v_e (in case of V_e) and wheel tangential velocity u (in case of U) to the flow rate, multiplied by the square of the geometric head. The dimensionless expression can be finally written as:

$$Ne = f(G, Re, U, V) \tag{3.49}$$

3.3.2 Dimensionless results

The dimensional analysis was extended to the experimental results, in order to estimate the maximum mechanical power output ($P_{out,,max}$) generated for each configuration characterized by a value of Q and a. Since the maximum power output is calculated for a fixed configuration (Q and a), it is not necessary to consider the dependency of P_{max} from the dimensionless flow rate numbers, i.e. the dimensionless parameters U and V_e. Considering the plot of Ne versus Re based on experimental data (Fig.3.22), the Newton number is assumed to be a power function of the Reynolds number.

Therefore, the relationship between the two parameters is:

$$Ne = \psi_1 Re^{\psi_2} \tag{3.50}$$

In order to obtain an expression for ψ_1 and ψ_2, Eq.3.50 was applied to experimental data for each sluice opening configuration (i.e. for each value of the parameter G), determining ψ_1 and ψ_2 for each configuration of $G = a/H_g$. The values of ψ_1 and ψ_2 were then plotted versus the parameter G and interpolated by the ordinary least squares method. Therefore, expressing ψ_1 and ψ_2 as a function of G, Ne can be easily calculated.

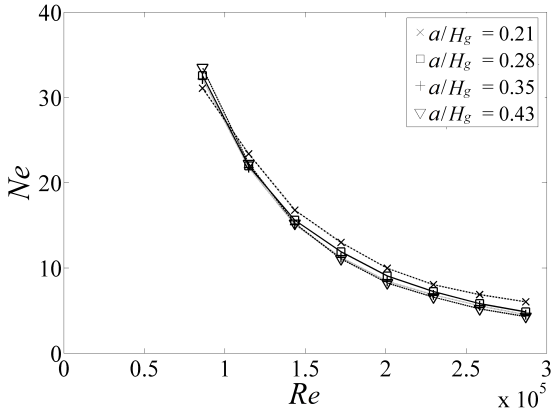

Fig. 3.22. Dimensionless representation of the Newton number (Ne) and Reynolds number (Re) calculated from experimental data.

$$\psi_1 = 7.95 \cdot 10^{11} G^{4.95} \tag{3.51}$$

$$\psi_2 = -0.43 ln(G) - 2.09 \tag{3.52}$$

In Fig.3.22 the Newton number is plotted versus the Reynolds number. Since P_{max} is made dimensionless dividing it by Q^3 (obtaining Ne), while the Reynolds number (Re) is linearly dependent on Q, Fig.3.22 shows an expected decreasing curve. It can be also observed that the decrease in the sluice gate opening increases the mechanical power output, due to the fact that the entry flow velocity increases, providing a higher impact force against the blades. Figure 3.23 shows the maximum estimated mechanical power output ($P_{out,max}$) calculated by eq. 3.50 versus the measured experimental one ($P_{exp,max}$). The calculated data are close to the bisecting line, proving that the dimensional law is appropriate to predict the power production for the breastshot water wheel. It can be also applied to fast breastshot water wheels with similar dimensions with respect to the investigated wheel.

3.4 Numerical analysis

The main purpose of the present section is the investigation of the effect of the blades number on the performance of the breastshot water wheel and to study more in detail the fluid dynamic interaction with the flow. Then, the performance of the wheel will be compared with the performance achieved using an improved

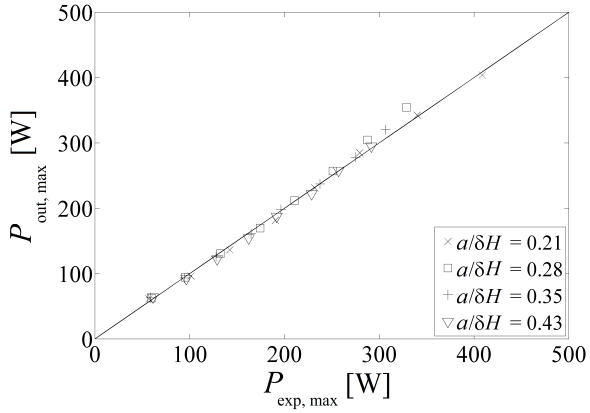

Fig. 3.23. Linear regression between the maximum mechanical power output calculated from dimensional analysis ($P_{out,max}$) and from laboratory tests ($P_{exp,max}$). Continuous line is $y = x$

blades shape, using the original number of the blades. In order to achieve these goals, Computational Fluid Dynamic simulations will be carried out.

In the last decades, the employment of CFD tools for solving fluid dynamic problems has been developing more and more, since CFD tools enable to access to local flow properties with relative low costs and with a substantial reduction in the experimental expenditure. For these motivations, fluid dynamic simulations may represent a suitable and efficient method also to investigate the hydraulic behavior of water wheels, obtaining useful information for their design. The involved phenomena in a breastshot water wheel are generally quite complex, since they involve an unsteady 3D turbulent regime, a bi-phases formulation (a primary and a secondary phase, air and water, respectively), the gravity external force and the moving and curved body of the wheel.

CFD simulations for the optimization of the blade shape of horizontal water wheels (Pujol et al., 2010; Pujol et al., 2015) and for the optimization of deep stream wheels by inclined plates under the wheel (Liu and Peymani, 2015; Akinyemi and Liu, 2015a; Akinyemi and Liu, 2015b) have been already presented in scientific journals, while to the best of our knowledge CFD results for gravity water wheels were not previously available in the literature. In the present work, the suitability of fluid dynamic simulations will be demonstrated also for breastshot water wheels, using a commercial code, and for overshot water wheels (in section 4.4). The numerical results are validated with the experimental ones. In the next sections, the numerical method will be described, and the effect of the number of blades and their shape will be investigated, acting in the geometry of the CFD model.

3.4.1 Numerical setup

Numerical transient RANS simulations, three dimensional and two-phases were carried out. The numerical set up is described in the following sections.

CFD model: geometry and mesh

The computational domain is constituted of three subdomains; the stationary domain of the channel, which conveys water to the wheel, the rotating domain of the wheel, which interacts with the channel, and the stationary domain outside of the wheel, filled only with air. A sliding mesh approach was used. The stationary air domain is subdivided in an internal domain, in contact with the wheel, and an external domain. The latter has the scope to locate the boundary conditions sufficiently far away from the wheel and to stabilize the solution (Fig.3.24).

The channel and the wheel are meshed with tetrahedral elements, whose dimensions range between 0.01 and 0.02 m (a mesh size of 0.02 m in the buckets ensures a mesh independent solution, as illustrated in section 4.4.4.1. The stationary air domain is meshed with tetrahedron and cubic elements, whose dimensions range between 0.02 m near the wheel and the channel, up to 0.1 m at the boundaries of the external domain. The air domain is subdivided in different regions with different mesh sizes, in order to create numerical dissipation and stabilize the solution. The coarse mesh near the boundaries of the external domain does not affect the interaction between water and wheel. In order to reduce computational time without losing accuracy in the solution, it is not necessary to simulate the whole domain of the wheel (2π rad); only half a wheel can be simulated to capture the hydraulic interaction (Barstad 2012), and the remaining half portion of the wheel is simulated with a coarser mesh and without blades (reducing the domain complexity). The final mesh has 1.3 million of cells (Fig.3.25).

3.4.1.1 CFD model: simulation setup

The 3D equations for solving the flow field in the computational domains are the Reynolds Averaged Navier–Stokes (RANS) equations, which include three momentum equations (one equation for each cartesian coordinate) and the continuity equation. The pressure and the velocity variables y are decomposed in the time averaged value $\bar{y}$ and the fluctuating component y'; the latter represents the difference between the instantaneous value of variable y and the time averaged value $\bar{y}$.

An additional continuity equation is added to solve the multiphase problem,

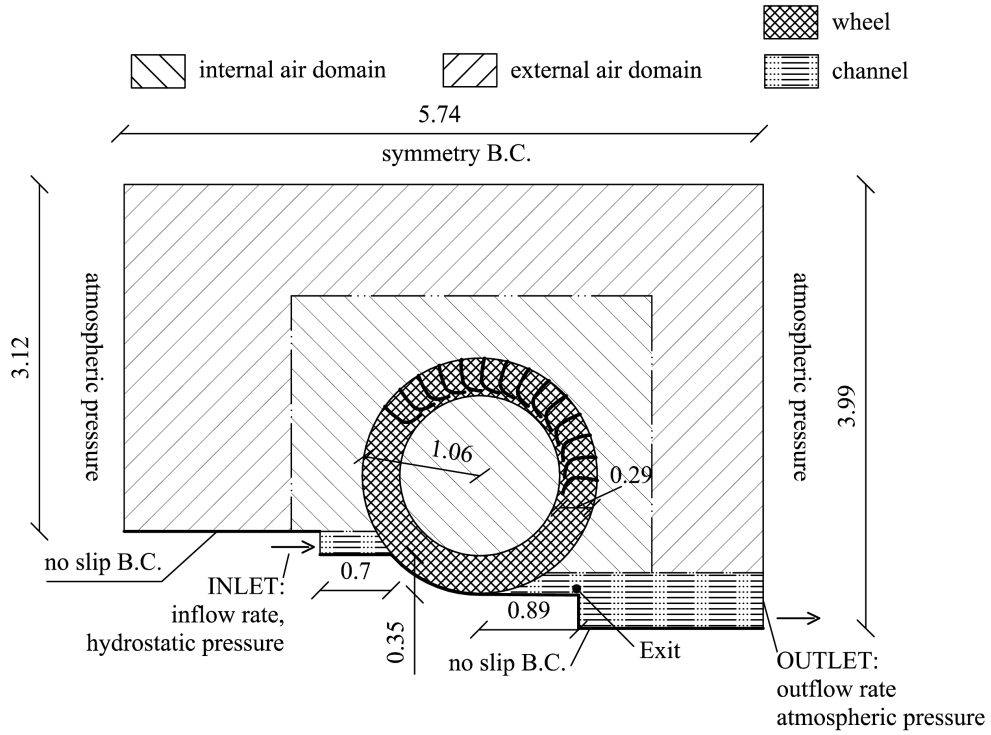

Fig. 3.24. The computational domain and the boundary conditions (B.C.) of the numerical model. The figure represents a longitudinal section, on the vertical symmetry plane. Some representative dimensions are reported (m). Downstream of the wheel, at the exit, the flow falls as a free jet into a tank.

since two phases (air and water, separated by a free surface) are involved. The additional continuity equation allows to determine in each cell of the domain the fraction volume of water and air. Once the volume fraction of each phase in all the cells of the domain is known, the physical properties (viscosity and density) of the mixture can be estimated (eq.3.54 and eq.3.55) to solve the RANS equations of the mixture. The Volume of Fluid model (VOF) was used to solve the multiphase problem, because it can be used with two or more immiscible fluids, where the continuity equation for a phase q is solved, tracking its volume fraction α_q throughout the domain (eq.3.53).

$$\frac{\partial \alpha_q}{\partial t} + \frac{\partial(\alpha_q \bar{u_i})}{\partial x_i} + \frac{\partial(\alpha_q \bar{u_j})}{\partial x_j} + \frac{\partial(\alpha_q \bar{u_w})}{\partial x_w} = 0 \tag{3.53}$$

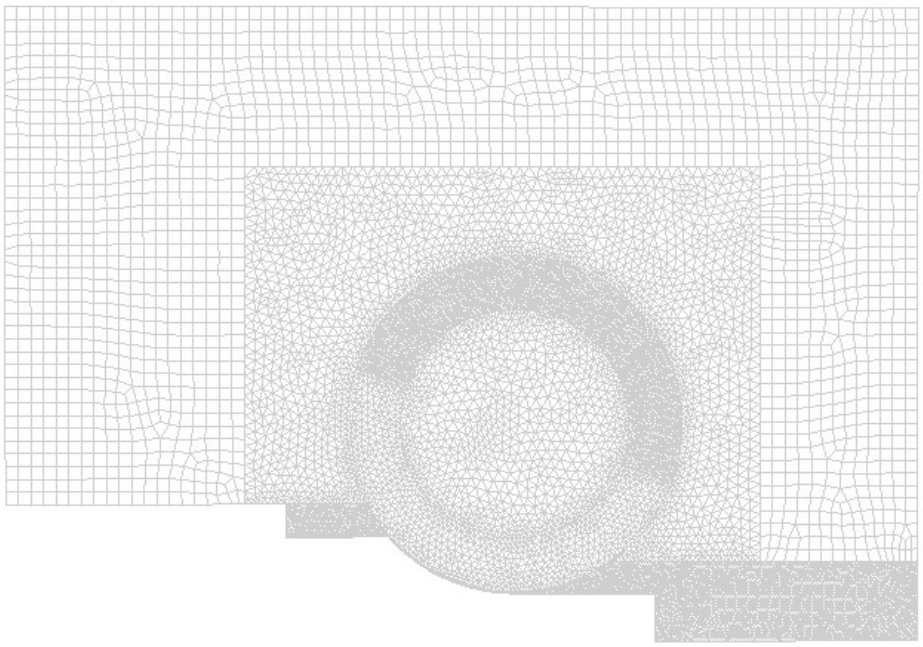

Fig. 3.25. The computational meshed domain. The figure represents a longitudinal section, on the vertical symmetry plane. The portion of the wheel with the blades is meshed with finer elements, which after about 1 s begins to interact with the stream.

where α_q represents the volume fraction of phase q (the so called secondary phase, that in our case is represented by water) in each cell. When $\alpha_q = 1$ the cell is filled of water, when $\alpha_q = 0$ the cell is filled of air, and when $0 < \alpha_q < 1$ the cell is near the free surface. Once the volume fraction of phase q is identified, the volume fraction of phase p (air) is calculated by $\alpha_p = 1 - \alpha_q$. In eq.3.53, x_i, x_j and x_w are the directions of the cartesian reference coordinate system and the generic $\bar{u_y}$ is the time averaged velocity of the mixture (see eq.3.57) in the x_y direction.

For the solution of the VOF equation, an implicit interpolation scheme was used, coupled with the level-set method. This method is a well established interface-tracking method for computing two-phases flows with topologically complex interfaces. The level-set function is smooth and continuous (Osher and Sethian 1988), thus its spatial gradients can be accurately calculated. Therefore, the interface curvature and surface tension forces due to the curvature are estimated accurately. However, the level-set method is not efficient in ensuring volume con-

servation (Olsson et al. 2007). On the other hand, the VOF method is naturally volume-conserved; indeed it calculates and tracks the volume fraction of a particular phase in each cell, instead of the interface itself. The weakness of the VOF method is the calculation of its spatial derivatives, since the volume fraction of a particular phase is discontinuous across the interface. To overcome the deficit of the level-set method and the VOF method, a coupled level-set and VOF approach was used.

After the determination of fraction volume α_q and α_p of the phases in each cell, the mixture properties can be calculated:

$$\rho = \alpha_q \rho_q + \alpha_p \rho_p \tag{3.54}$$

$$\mu = \alpha_q \mu_q + \alpha_p \mu_p \tag{3.55}$$

where ρ and μ are the density and dynamic viscosity of the mixture and ρ_y and μ_y are the properties of the generic phase y.

The RANS continuity and momentum equations for the mixture are then solved. For an incompressible fluid the continuity equation is:

$$\frac{\partial \bar{u_i}}{\partial x_i} + \frac{\partial \bar{u_j}}{\partial x_j} + \frac{\partial \bar{u_w}}{\partial x_w} = 0 \tag{3.56}$$

The momentum equation for the mixture in direction x_i is:

$$\rho \left(\frac{\partial \bar{u_i}}{\partial t} + u_i \frac{\partial \bar{u_i}}{\partial x_i} + u_j \frac{\partial \bar{u_i}}{\partial x_j} + u_w \frac{\partial \bar{u_i}}{\partial x_w} \right) = \rho g_i - \frac{\partial \bar{p}}{\partial x_i} + \mu \nabla^2 \bar{u_i} + \\ \frac{\partial}{\partial x_i}(-\rho \overline{u_i' u_i'}) + \frac{\partial}{\partial x_j}(-\rho \overline{u_i' u_j'}) + \frac{\partial}{\partial x_w}(-\rho \overline{u_i' u_w'}) \tag{3.57}$$

where ρ and μ are the density and dynamic viscosity of the mixture, g is the gravitational acceleration, $\bar{p}$ is the time averaged pressure and $\bar{u_i}$ is the mixture time averaged velocity along the direction x_i. An analogous momentum equation is solved for the direction x_j and x_w.

The terms $\rho \overline{u_i' u_j'}$ are the Reynolds turbulent stresses, and they can be expressed as:

$$\tau_{i,j} = -\rho \overline{u_i' u_j'} = \mu_t \left(\frac{\partial \bar{u_i}}{\partial x_j} + \frac{\partial \bar{u_j}}{\partial x_i} \right) - \frac{2}{3} \rho k \delta_{ij} \tag{3.58}$$

where μ_t is the turbulent viscosity, k is the turbulent kinetic energy and δ_{ij} is the Kronecker delta.

The turbulence viscosity is modeled using the shear-stress transport (SST) $k-\omega$ model (Menter, 1994), where the turbulent viscosity is expressed as a function of the turbulent kinetic energy k and the specific dissipation rate $\omega = \epsilon/k$, where ϵ is the turbulence dissipation. The solution of two evolution equations (for predicting k and ω) determines the turbulent viscosity μ_t, that resolves the closure problem of the RANS formulation.

$$\mu_t = \rho \frac{k}{\omega} \frac{1}{\max\left[\frac{1}{\alpha^*}; \frac{SF}{a_1 \omega}\right]} \tag{3.59}$$

where α^* damps the turbulent viscosity causing a low-Reynolds number correction, a_1 is a constant, S is the strain rate magnitude and F is a blending function (Menter, 1994). The SST turbulence model performs better than the $k-\epsilon$ model when adverse pressure gradients and separations occur and at the walls (Menter, 1994). It has been successfully used in Pujol et al. (2010) and Pujol et al. (2015).

The $k-\omega$ equations are, respectively:

$$\begin{aligned} &\frac{\partial(\rho k)}{\partial t} + \frac{\partial(\rho k \bar{u_i})}{\partial x_i} + \frac{\partial(\rho k \bar{u_j})}{\partial x_j} + \frac{\partial(\rho k \bar{u_w})}{\partial x_w} = \\ &\frac{\partial}{\partial x_i}\left(\Gamma_k \frac{\partial k}{\partial x_i}\right) + \frac{\partial}{\partial x_j}\left(\Gamma_k \frac{\partial k}{\partial x_j}\right) + \frac{\partial}{\partial x_w}\left(\Gamma_k \frac{\partial k}{\partial x_w}\right) + G_k + Y_k + S_k \end{aligned} \tag{3.60}$$

$$\begin{aligned} &\frac{\partial(\rho \omega)}{\partial t} + \frac{\partial(\rho \omega \bar{u_i})}{\partial x_i} + \frac{\partial(\rho \omega \bar{u_j})}{\partial x_j} + \frac{\partial(\rho \omega \bar{u_w})}{\partial x_w} = \\ &\frac{\partial}{\partial x_i}\left(\Gamma_\omega \frac{\partial \omega}{\partial x_i}\right) + \frac{\partial}{\partial x_j}\left(\Gamma_\omega \frac{\partial \omega}{\partial x_j}\right) + \frac{\partial}{\partial x_w}\left(\Gamma_\omega \frac{\partial \omega}{\partial x_w}\right) + G_\omega + Y_\omega + S_\omega + D_\omega \end{aligned} \tag{3.61}$$

where G is the generation of turbulent kinetic energy (or generation of dissipation), Γ represents the effective diffusivity, Y is the dissipation of k (or ω), D represents the cross diffusion term and S represents the eventual user-defined source term, which is zero in the present case.

The modified High Resolution Interface Capturing scheme (HRIC) was used for computing the volume fraction. The pressure-velocity coupling was solved by

the Piso scheme and the spatial discretizations were made by the Presto scheme for pressure and the Second Order Upwind scheme for momentum and turbulent kinetic energy.

The time step chosen for the unsteady simulation was $8 \cdot 10^{-4}$ s; during some simulations it was necessary to reduce it to $5 \cdot 10^{-4}$ s. A Second Order Implicit scheme in time was used for the temporal discretization; 20 inner iterations were carried out between two consecutive time steps for the pressure-velocity solving, in order to ensure a residual less than 0.001.

3.4.1.2 Boundary conditions

The mass flow rate was imposed at the inlet of the channel, specifying the free surface level and the entry flow rate (kg/s). At the inlet a fixed value of the turbulence intensity $I = 0.05$ was chosen: a turbulence intensity less than 0.01 is generally considered low and turbulence intensity greater than 0.1 is considered high. A fixed value of the turbulent viscosity ratio $\mu_t/\mu = 10$ was also imposed, where μ is the dynamic viscosity of water. These values are generally fixed by default and a literature review confirms them (Pujol et al. 2010). At the outlet of the channel and at the external surfaces of the external air domain, the atmospheric pressure was adopted. At the top of the external domain the symmetry boundary condition was imposed (although this condition is not physical, it gives more stability to the solution, and it does not affect the interaction between water and wheel). Because of the wheel symmetry with respect to a vertical plane perpendicular to the rotation axle passing for the axle center, the symmetry boundary condition was imposed on this surface, thus only one half of the wheel was simulated, in order to save computational time. At the walls of the blades, channel bed and wheel, the no slip boundary condition was imposed (Fig.3.24). The fraction volume of water and mixture velocity were imposed equal to zero throughout the domain, except than at the inlet.

In the numerical simulations, a sluice gate opening was fixed and three particular cases were chosen, each one with a defined flow rate and wheel rotational speed. An opening of 0.075 m was adopted (1) in order to achieve high velocity of the jet interacting with the blades (the power output increases with the reduction in the sluice gate opening and for this sluice gate opening a wider range of flow rates has been experimentally investigated with respect to the sluice gate opening $a = 0.05$ m); (2) flow rates of 0.05 m^3/s (case 1), 0.06 m^3/s (case 2) and 0.07 m^3/s (case 3) were adopted and wheel rotational speeds (3) were chosen in order to investigate optimal working conditions of the breastshot water wheel (0.78, 0.79, 0.89 rad/s, respectively). These velocities are similar also to compare the

performance at different flow rates and approximately constant rotational speed. In these conditions, the water depth at a location 0.27 m upstream of the wheel was 0.05 m (Tab.3.7).

3.4.2 Numerical results

Post processing of the results

Using the described CFD model, the effect of the number of blades on the efficiency of the breastshot water wheel was investigated, in order to determine the optimal one and to illustrate further details on the hydraulic behavior. In particular, 16, 32, 48 and 64 blades were investigated. Once the numerical model with 32 blades is validated (32 is the original number of blades), it is possible to obtain a performance optimization by changing the number of blades in the geometry setup. Then, an improved blade shape was also investigated.

For each geometric case (different number and shape of the blades), three flow rate cases were simulated (case 1, case 2 and case 3); the flow rate cases are reported in Tab.3.7. During the simulations, each time step took approximately 2 min in a processor at 2.40 Ghz with 8 Gb RAM; the total time of each simulation was approximatively $7 \div 10$ days.

The shaft torques due to the water-blades interaction (exerted by the water on the blades of the wheel) were monitored during the simulations, hence chosen as control parameter of the simulation. The shaft torque (the friction at the bearings is negligible, as found in the theoretical results) is called C_j, where j is the suffix that distinguishes each geometric case (blade shape and number). Figure 3.26 depicts the trend of the torque during the time; when the blades start to interact with the flow, the torque increases and, after the transitory time, the torque trend oscillates periodically around its average value (called $\overline{C_j}$); due to the wheel radial symmetry, the period of oscillation is $T = \beta/N$. The average torque becomes constant after about 3 seconds of simulation and the period of the oscillations decreases with the blades number, since the period T is smaller for bigger blades numbers. The average value ($\overline{C_j}$), after the first three seconds, is the control parameter used to evaluate the mesh independence of the solution, to test the accuracy of the numerical model (comparing it with the experimental torque C_{exp}); in this way it is possible to estimated how the performance of the wheel is affected by the blades number and shape.

A mesh sensitivity analysis was carried out to check that the solution was independent from the mesh. The finer the mesh, the more detailed the results, but the higher the computational costs (PC storage capacity and time of simulation);

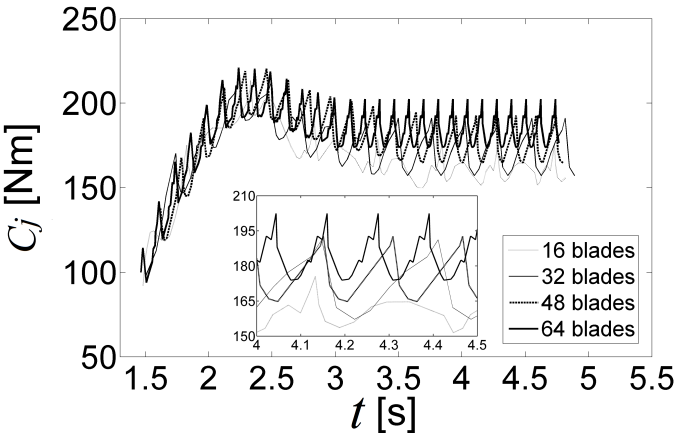

Fig. 3.26. Numerical shaft torque during the time for different numbers of blades (case 1: $Q = 0.05$ m^3/s).

it is thus essential to find the optimal compromise between computational cost and accuracy of the solution. Two different meshes were used to calculate the numerical torque, for the three cases with 32 blades, evaluating the effect of the mesh size on the numerical solution. The first mesh was made by elements of 0.02 m in the buckets ($\overline{C_{32,a}}$), while the second mesh was made by elements with dimension of 0.01 m size at the blades surface, ($\overline{C_{32,b}}$). In Tab. 3.7 it is shown that the differences in the results using the two meshes are extremely low; hence the best compromise between accuracy and computational cost is obtained using the first mesh, with element of dimension 0.02 m (the finer mesh was instead used when the shape of the blades was investigated).

Table 3.7. Investigated operative conditions, numerical torque results for the wheel with 32 blades and original shape (two different meshes were investigated - the "$32, a$" is the coarser-), torque from experimental tests (C_{exp}) and efficiency obtained by the numerical simulations and experiments. Each line corresponds to a certain investigated configuration (case); for each case, two meshes were tested.

case	Q (m^3/s)	N (rad/s)	$\overline{C_{32,a}}$ (Nm)	$\overline{C_{32,b}}$ (Nm)	C_{exp} (Nm)	$\eta_{32,a}$ (-)	η_{exp} (-)	$\frac{\overline{C_{32,a}}-C_{exp}}{C_{exp}}$ (%)
1	0.05	0.78	173	173	175	0.670	0.678	-1.16
2	0.06	0.79	212	211	226	0.615	0.656	-6.19
3	0.07	0.89	238	239	253	0.586	0.623	-5.9

The discrepancies between the numerical and the experimental solution were

then calculated, determining the accuracy of the numerical model. The accuracy of the numerical shaft torque prediction for the cases with 32 blades is very good, with the average discrepancy between the numerical and experimental torque lower than 5% (Tab.3.7). The numerical model generally underestimates the torque. For case 1 (flow rate 0.05 m^3/s), the discrepancy is -1.16%, while the discrepancy settles around -6% for case 2 and case 3. An additional validation was made on the water depths. The water depths 0.27 m upstream of the wheel were quantified in 0.053 m in the numerical models, with a discrepancy of 6% with the experimental value of 0.05 m. The higher the flow rate, the higher the turbulence intensity due to the higher flow velocity, thus the more complex is the problem. Due to the good accuracy of the results, it is hence possible to investigate how the performance of the wheel is affected by the blades design, investigating typical blades numbers of similar water wheels (16, 48 and 64), and one additional blades shape.

In the following sections the results are illustrated and discussed in detail.

3.4.3 Number of the blades

Introduction to the results

In literature, the blade number effects on the performance of other kinds of water wheels have been already investigated. In Luther et al. (2013) the efficiency of a stream wheel with straight blades increased from 4 to 8 paddles, whereas in Tevata and Chainarong (2011) a stream water wheel with straight blades has been tested and the efficiency decreased passing from 6 to 12 blades. Moreover, in Müller et al. (2010) it is illustrated that the efficiency of a stream water wheel increased from 8 to 24 blades, with a substantial improvement from 8 to 12.

Therefore, for stream wheels an optimum blade number can be identified. Hence an optimal one may also be identified for the breastshot wheel under consideration.

3.4.3.1 Description of the hydraulic behavior of the wheel

Before discussing the results, it is essential to illustrate some useful concepts about the impact/filling process, and briefly illustrated in section 3.2.2.1.

If eq. 3.19 in section 3.2 is solved for different blades numbers n (or different β) and for each investigated experimental case, it is possible to understand the effect of n on the performance characteristics of the wheel. Investigating 24, 28,

36, 40 and 48 blades, the power do not change significantly (Quaranta and Revelli (2015a).

For example, if the difference e_{LQ} is defined as:

$$e_{LQ} = \frac{L_{Q,n} - L_{Q,32}}{P_{net}} \tag{3.62}$$

where $L_{Q,n}$ are leakage losses estimated for a number of blades different from 32 and $L_{Q,32}$ that estimated in our case ($n_b = 32$), $e_{LQ} < 2\%$ (excluded the uncommon cases for $Q = 0.02$ m^3/s, where $e_{LQ} < 8\%$).

Therefore, the one dimensional theoretical model says that reasonable changes in the blades number do not affect significantly the power losses, while the effect of the blades number on the impact losses can not be quantitatively investigated (in that model an optimization process was carried out to determine the impact power losses for the wheel with 32 blades). Therefore, accordingly with it, the changes in the wheel performance with the blades number that will be discussed in these sections, should be mainly attributed to the consequences on the impact and filling processes.

When the tip of the blade is coincident with the channel bed just upstream of the wheel (step 1 in Fig.3.16), the impact configurations are in their optimal conditions. In this situation, the water jet flows along the blade without falling as a free jet and without generating substantial turbulent impact losses (as long as the jet velocity relative to the blade is approximatively parallel to the blade inclination, as a correct design should provide). If in step 1 there are not other blades directly interacting with the jet (as an optimal design for this kind of breastshot wheels also should guarantee), the exerted impact torque on the considered blade in this configuration is not affected by the blades number. After the blade rotates, the impact conditions become not optimal any more; the relative entry velocity is not parallel to the blade inclination and the water may also fall into the buckets as a free jet (step 2). In this step, the buckets are already partially filled; the water flow impinges against a water volume (dissipating a portion of its kinetic energy), instead of performing useful work directly interacting with the blades. Hence the impact power losses are very sensitive to the instantaneous configuration, and they are significantly affected by the wheel rotation.

Therefore, the temporal trend of the torque experiences a peak value (step 1), and, after the peak, a decrease. When a new blade begins to interact with the flow, the impact torque increases again. As a consequence, the lower the blades number the longer the decreasing part of the trend. Thereby, considering the peak values reasonably coincident (since in the optimal configuration -step 1- the kinetic energy of the flow transferred to the blade is not affected by the blades

number), the average torque decreases with the decrease in the blades number. Moreover, the lower the blades number, the bigger the water which cumulates inside each bucket and which interferes with the approaching water flow, thus the higher the dissipation of the water kinetic energy. The previous conjecture is confirmed observing Fig.3.26.

Considering the numerical results for 32, 48, 64 blades, the monitored torque trend corresponds to the expected trend described previously. The amplitude of the oscillations decreases with the blades number and the peak values are close together (the zoom reported in Fig.3.26 clarifies this aspect, at the temporal instant t=4.12 s). Instead, the torque trend for 16 blades is quite flat and the torque peak is significantly lower. These differences of the trend have to be attributed to the different water behavior inside the filled buckets, which now moves with pronounced oscillations.

Indeed, observing Fig.3.27, the water surface in the buckets can be considered practically horizontal and at rest only in the range from 32 to 64 blades, while in the case of 16 blades the water inside the buckets moves with bigger oscillations.

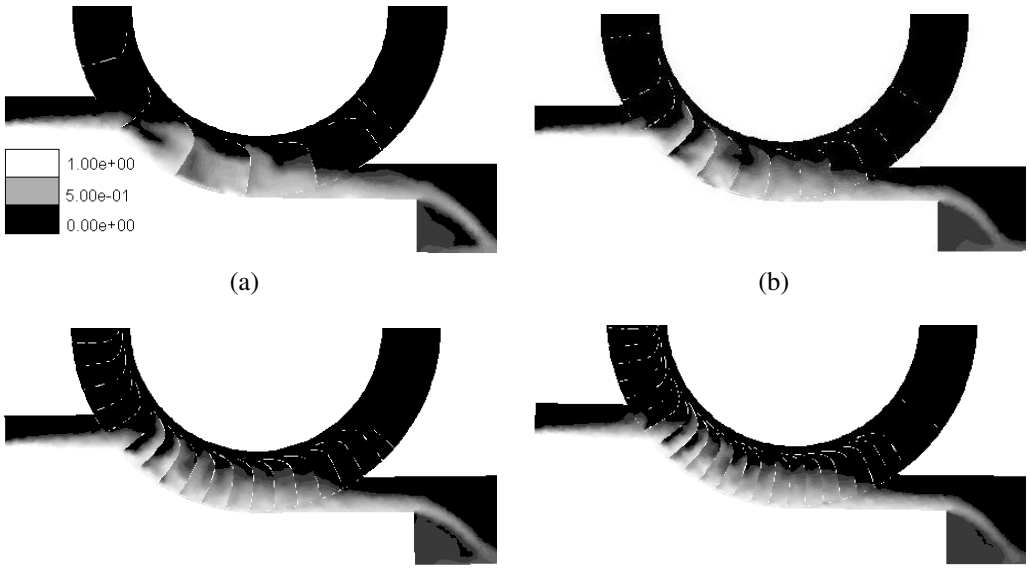

Fig. 3.27. Contour of volume fraction for case 1: 16 (a), 32 (b), 48 (c) and 64 (d) blades. White corresponds to the cells with only water present and black those with only air. The transition between the two colors indicates the free surface and that the two fluids are mixed.

This is a consequence of the longer interaction (due to the larger distance between the blades) between the water jet and the bigger volume of water which

is already in the buckets; the water inside the buckets is also less confined for the cases with 16 blades. Fig.3.28 confirms what can be seen in Fig.3.27; for the cases of 16 blades, the turbulent viscosity inside the buckets, as well as the turbulence intensity, is higher ($\mu_t \simeq 0.23$ kg/(m· s) at 16 blades and $\mu_t \simeq 0.08$ kg/(m· s) at 64 blades), since a large amount of kinetic energy of the entry flow leads an increase in the turbulence of the water volume in the bucket, in spite of performing useful work on the blades.

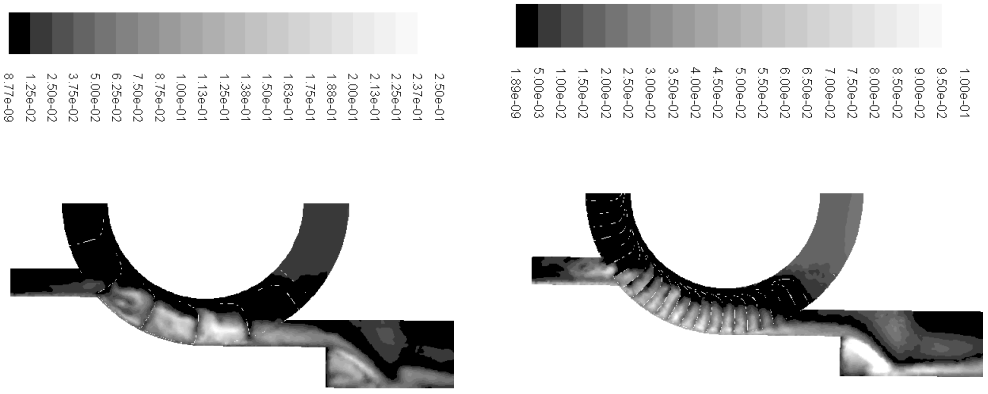

(a) *16 blades* (b) *64 blades*

Fig. 3.28. Contour of turbulent viscosity (Kg/m·s) for case 2: 16 (a) and 64 (b) blades.

Therefore, in the range from 32 to 64 blades it is reasonable to attribute the changes in the wheel performance (due to different blades number) mainly to the blades number effects on the impact and filling process; this process affects the transfer process of kinetic energy between the water jet and the paddles. At 16 blades, additional power losses are also generated by the water oscillations in the buckets (kinetic energy that is never transferred to a useful form) and by the sooner release of water into the tailrace.

3.4.3.2 Practical results and performance

Scope of the present section is to show how the efficiency of the wheel is affected by the blades number and to suggest some practical recommendations.

In Fig.3.29 and Tab.3.8 the shaft torque from numerical simulations is reported versus the blades number, while in Fig.3.30 and Tab.3.9 the results are reported in terms of efficiency.

The trend equation of the efficiency versus the blades number which interpolates the data in Fig.3.30 and Tab.3.9 is assumed to be:

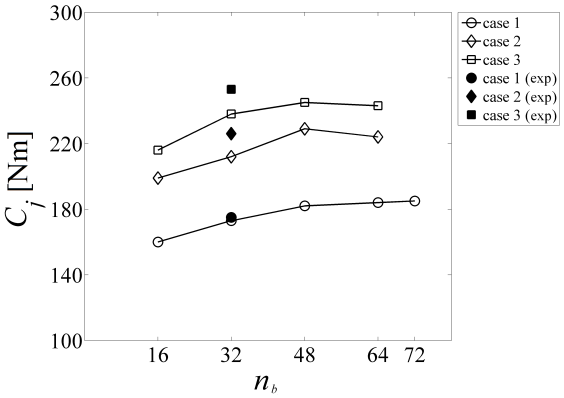

Fig. 3.29. Shaft torque from numerical simulations and experimental tests (exp) versus the number of blades.

$$\eta_{num} = a_y n_b^2 + b_y n_b + c_y \tag{3.63}$$

where the subscript y refers to each investigated case and:

$[a_1, b_1, c_1] = [-3.7 \cdot 10^{-5}, 5.0 \cdot 10^{-3}, 0.55]$; $[a_2, b_2, c_2] = [-6.0 \cdot 10^{-5}, 6.3 \cdot 10^{-3}, 0.49]$; $[a_3, b_3, c_3] = [-5.7 \cdot 10^{-5}, 5.9 \cdot 10^{-3}, 0.45]$.

The number of blades affects the efficiency of the wheel. The maximum increase in performance passing from 16 blades to the optimal blades number is quantified between 12 to 16%, depending on the flow rate. For case 2 and case 3 ($Q = 0.06$ and $Q = 0.07$ m^3/s, respectively) the optimal blades number among the investigated ones is 48, since the efficiency then begins to decrease. In case 1 ($Q = 0.05$ m^3/s) the torque trend does not exhibit a maximum in the explored range. Therefore, an additional simulations was added for 72 blades to understand the performance for higher blades numbers.

Table 3.8. Investigated operative conditions, numerical torque results for the wheel with 16 blades, 32 blades (two different meshes were investigated), 48 blades and 64 blades. A simulation for 72 blades was added for practical reasons to case 1, as explained in the *Practical results* section.

case	Q (m^3/s)	N (rad/s)	$\overline{C_{16}}$ (Nm)	$\overline{C_{32,a}}$ (Nm)	$\overline{C_{32,b}}$ (Nm)	$\overline{C_{48}}$ (Nm)	$\overline{C_{64}}$ (Nm)	$\overline{C_{72}}$ (Nm)
1	0.05	0.78	160	173	173	182	184	185
2	0.06	0.79	199	212	211	229	224	-
3	0.07	0.89	216	238	239	245	243	-

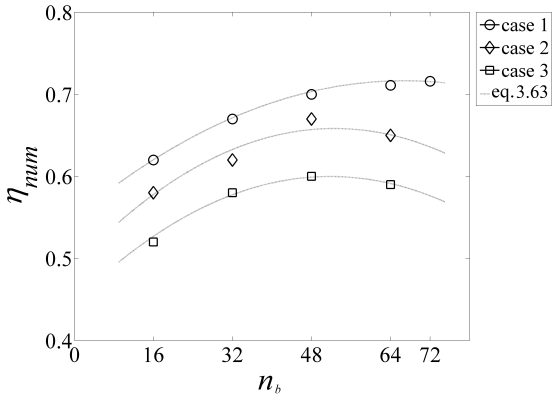

Fig. 3.30. Efficiency from numerical simulations versus the number of blades and trend equations.

Table 3.9. Investigated operative conditions and efficiency for the wheel with 16 blades, 32 blades, 48 blades and 64 blades. For case 1, 72 blades were also investigated for practical reasons, as explained in the *Practical results* section.

case	η_{16}	$\eta_{32,a}$	η_{48}	η_{64}	η_{72}
1	0.62	0.67	0.70	0.71	0.72
2	0.58	0.62	0.67	0.65	-
3	0.53	0.58	0.60	0.59	-

Observing the trend lines in Fig.3.30 for case 2 and case 3, the theoretical maximums are close to 48 blades, whereas for case 1 the maximum is close to 64. This is a reasonable result, since the higher the flow rate, the bigger the buckets dimension can be. Anyway, since in case 1 the performance practically does not change after 48 blades, $n = 48$ is also suggested as optimal number of blades.

The existence of an optimal blades number is justified by the following practical motivations. When the blades number is too small, only few blades interact with the water. When the water enters into the cells, higher power losses occur as the water jet loses potential energy with respect to at bigger numbers of blades, because of the larger distance between two blades. Furthermore, the jet dissipates a bigger amount of kinetic energy impacting on the water volume in the cells and the water downstream is released into the tailrace sooner. When the blades number is too high, the space between two blades becomes very small, generating obstructions and additional power losses in the filling process; as a consequence the efficiency does not increase any more and generally the effi-

ciency decreases. Therefore, also in this work an optimal number of blades is identified, as for stream water wheels. Finally, considering a water depth of h=5 cm just upstream of the wheel and the peripherical distance l between two blades (at the optimal number of blades) it is possible to recommend for these wheels a maximum ratio $l/h = 2.5$.

Equation 3.63 can be used as practical and simple tool to determine optimal blades numbers for geometrically similar breastshot water wheels in similar working conditions. We also recommend the optimal rotational wheel speed be included in the range $0.3 < u^* < 0.4$ (Quaranta and Revelli, 2016). In general terms, it is possible to recommend for fast breastshot wheels a maximum ratio $l/h = 2.5$.

While the present results illustrate that the number of blades affects the performance of the wheel, the blades number does not affect significantly the upstream and downstream conditions. This means that it is possible to change the blades number of similar breastshot water wheels without significant consequences on the exploited channel.

3.4.4 Shape of the blades

Introduction and geometry

Although the general criteria that should be taken into account in the blades design of breastshot water wheels are well established, numerical or experimental investigations on the optimal profile of breastshot wheels blades can be rarely found.

Specifically, the general design criteria for the blades profile are:

(1) the relative entry flow velocity in the impact point should be directed as the blade surface, in order to reduce the inflow power losses;

(2) the uplift of water downstream of the wheel and the outflow power losses should be minimized. Hence the blades should exit at a normal angle with respect the free surface at the tailrace, or with a backward inclination in order to reduce the drag;

(3) the blades length should be long enough or curved in order to avoid losses of water at the root of the blades.

However, it is not so clear if the blades profile generates significant effects on the performance of this kind of wheel. Similar uncertainty has also been found for *Poncelet* wheels: in Weisbach (1849) and Faibairn (1864) the circular shape

is suggested, while in Bresse (1869) the Author says that the blades curvature is a matter of indifference.

More in detail, the scope of the present section is to understand if the blades profile affects the performance of the wheel, and to improve it. This work has been published in Quaranta and Revelli (2016c). Therefore, a circular modified profile (profile 2) is simulated, in addition to the original profile (profile 1). The modified profile is designed with the same tip inclination of profile 1, which is 16° on the horizontal in the entry point, in order to compare objectively the effect of different profiles. This tip inclination of the profiles is already almost parallel to the relative flow velocity, minimizing the impact power losses. In this case, the profiles are also well designed considering the outflow conditions, since the blades exit from the tailrace approximately normally, without uplifting water. The angle between the tangent at the tip and the tailrace water surface is 83° in the final position; it is good to be smaller than 90°, since the slight backward inclination at the tip allows to reduce the drag downstream.

The original profile (profile 1) is 0.40 m long, and it can be considered as composed of three parts. The first part of the profile (which immediately starts to interact with the flow) is a circular arc 0.22 m long and 0.60 m in radius. This part of the profile seems to be quite flat. The third part (the internal one) is flat and 0.1 m long. The previous two parts are connected by a circular arc 0.08 m long and 0.11 m in radius. The external part of the profile, which is the part that interacts with the flow mostly, is similar to the profile that would be obtained following the design procedure described in Weisbach (1849) for *Poncelet* wheels.

In order to determine the blade profile following the design procedure described by Weisbach (1849), it is necessary to know the tip inclination of the blade in the impact point and the depth of the blades as input parameters. These are 16° and 0.29 m, respectively, as it can be seen in Fig.3.5; the tip inclination on the horizontal is 62° under the wheel axis. The circular profile that would be obtained using the *Weisbach* procedure (Weisbach, 1849) would have a radius of 0.62 m, very close to the real one (profile (1)) of 0.60 m. However, in our case we do not deal with an original *Poncelet* water wheel, because *Poncelet* wheels are generally installed in straight channels, with no geometric heads or channel's bed drops through the wheel. Therefore, the radius of curvature of the procedure suggested by Weisbach (1849) for the blades design, which is similar to the existing profile, may not be the optimal for this breastshot water wheel. Also for this motivation a new profile was investigated.

Profile (2) is a circular profile; such profile was chosen both to make the manufacture process easier, and because also Weisbach (1849) and Faibairn (1864) suggested a circular shape. The shorter the radius of curvature, the more the de-

viation that the jet, flowing along the blade, undergoes, to which corresponds a change in its momentum. The change in momentum leads to a force on the blade, pushing the wheel more than what would occur using a straight blade or a bigger radius of curvature. But if the radius of curvature is too short, the jet may not be able to flow along the blade, since it would separate from the blade surface. Furthermore, the blade may uplift water from the tailrace, generating power losses. For example, in the present case, and considering the configuration in the entry point, a curvature radius of 0.2 m (1/5 R, with R the wheel radius) would have a portion of the profile that would be vertical. This would generate separation of flow and resistance; the flow would tend to fall down during the filling process, with power losses. Therefore, we considered as optimal blade radius $r = \frac{1}{4}R$=0.25 m, where $R = D/2$ is the wheel radius (Fig.3.31).

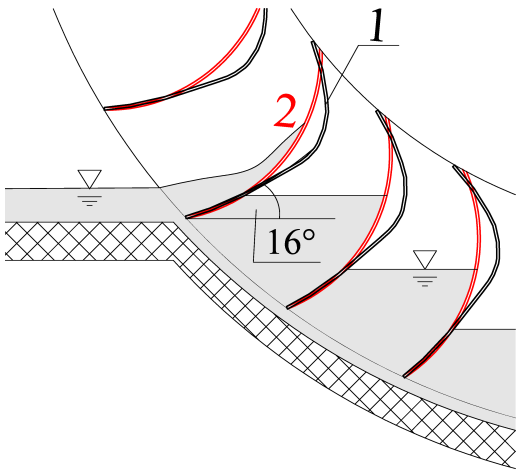

Fig. 3.31. The two blades shapes investigated in our work.

3.4.4.1 Numerical results

Table 3.10 illustrates the torque results for the original profile and the improved shape of the blades.

Table 3.10. Torque results (Nm) for the original profile (C_1) and the improved one (C_2). Flow rate Q in m^3/s and rotational speed N in rad/s.

case	Q	N	C_1	C_2	$\frac{C_2-C_1}{C_1}$
1	0.05	0.78	173	180	+4%
2	0.06	0.79	212	226	+6.6%
3	0.07	0.89	238	244	+2.5%

As it can be seen, the second profile is better. The circular profile allows to reduce the power losses at the inflow, since the momentum of the flow is better exploited. It is also optimal for the downstream conditions, since a circular profile can exit the free surface at a better angle during its rotation. Therefore, the shape of the blades affects the performance of the wheel, thus the efficiency can be improved acting also on the shape of the blades, in addition to their number. Therefore, for the blades design, it is recommended to design them satisfying the suggestions reported in section 3.4.4, and adopting a radius of curvature that does not generate counterforces, hence that in no points it is with a vertical inclination.

3.5 General design suggestions

In order to design a breastshot water wheel, firstly the dimensionless results of eq.3.50 and Fig.3.14 can be used to determine the maximum efficiency and the optimal inflow configurations, in order to obtain preliminary results concerning with the productivity and suitability of the water wheel. Then, knowing the inflow configuration, i.e. the flow velocity at the entry point and its water depth, the number of the blades can be chosen using the maximum ratio obtained in section 3.4.3.2. The tangential speed can be chosen by using Tab. 3.1, and the shape of the blades designed considering the suggestions reported in section 3.4.4. The wheel width can be estimated knowing the flow rate, wheel rotational speed and optimal filling ratio.

At this point, the theoretical model could be applied to estimate the power losses and the real efficiency (considering that using the improved blades shape the real efficiency improves). The estimated impact coefficient can be considered reliable in water wheels whose blades are oriented parallel to the relative flow velocity in the impact point, and when the water flow enters into the wheel substantially under the axle. The quantification of impact losses by the presented theoretical model may not be valid if the water entry point is close to the wheel axle. In this case, although the blades could be well designed, the moment arm of

the impact force would approach zero, and the generated force would be used to compress the wheel onto the shaft, instead of generating torque.

When the upstream water level is controlled using inflow weirs, the flow kinetic energy becomes small, and even if the impact coefficient would be not accurately representative of the reality, the error that would be committed would not be appreciable. Instead, when using a sluice gate and a significant inflow velocity to the wheel, the right estimation of the impact power losses would become determinant. Therefore, in order to apply the impact coefficient here found, the wheel should be as much possible similar as that here investigated. If it would not be similar (for example ratio between channel drop and diameter too different) the impact coefficient would be appreciably different. Anyway, for the motivations explained before, it is not advisable to have higher values of such geometric ratio. Smaller ratios are possible; in this way, the power output would increase, but, simultaneously, the higher diameter would imply higher costs.

Chapter 4

Investigation of an Overshot water wheel

Overshot water wheels are generally employed in hill and mountain regions, where heads higher than 3 m and small flow rates are available.

Scope of the present chapter is to investigate a 1:2 scale model of an existing overshot water wheel sited in Ciconio (Turin, Italy, Fig.4.1), in order to determine the performance as a function of flow rate and wheel rotational speed. A theoretical analysis will be presented for the estimation of the power losses and power output, supported also by a dimensional approach. These results have been published in Quaranta and Revelli (2015b). Numerical simulations will be also presented with the aim of increase the efficiency.

Fig. 4.1. The overshot water wheel in Ciconio, with diameter 3 m and width 2 m.

Similarly to the work on the breastshot water wheel, the present work aims to fill the gap of engineering information on overshot water wheels. Indeed, although a large number of overshot water wheels were in operation in the last century, only few series of tests were performed. Most of the test results were never published in hydraulic engineering textbooks or journals and they are only available in not widely known reports and articles (Müller and Kauppert, 2004), such as Weidner (1913) and Meerwarth (1935). In modern times, the performance of overshot water wheels has been investigated in Williams and Bromley (2000) while in Wahyudi et al. (2013) a new configuration has been studied for increasing the performance. The results will be better illustrated and compared in the following sections, where the experimental results achieved in this thesis will be described.

4.1 Experimental tests

4.1.1 Experimental setup

A 1:2 steel model of an overshot water wheel was installed in the Laboratory of Hydraulics at Politecnico di Torino (Fig. 4.2). The wheel external diameter is D=1.46 m and the width is b=1 m, while the conveying channel width is B=0.96 m, narrower than the wheel to allow for ventilation. The number of the curved blades, fastened to the lateral shrouds, is 24 and the weight of the wheel is $W_{wh} \simeq 4300$ N. The depth of the cells is $d = 0.153$ m.

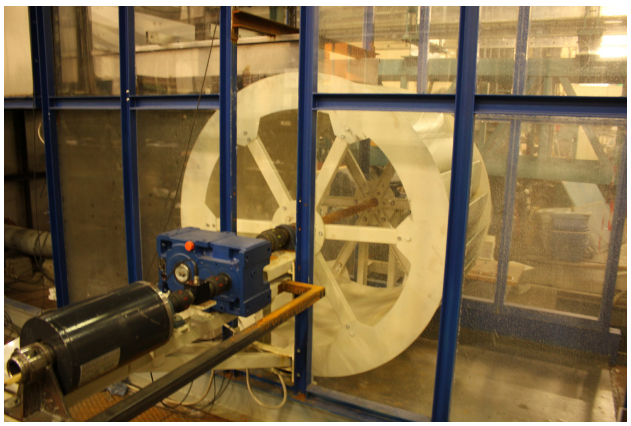

Fig. 4.2. The investigated overshot water wheel, with diameter 1.46 m and width 1 m.

256 operative conditions were investigated, by varying the entry flow rate ($Q = 0.01 - 0.137$ m^3/s, using 0.01 m^3/s steps) and the wheel rotational speed

($N = 5 \div 35$ rpm). The total discharge Q was imposed acting on a pump and detected by an electromagnetic flow meter, which accuracy was $\pm 0.5 \cdot 10^{-3}$ m^3/s. The water level h_u just upstream the wheel was measured by an ultrasonic sensor, with an accuracy of ± 0.002 m. Starting from the water level h_u and the flow rate Q, the stream velocity $v_u = Q/(Bh_u)$ and the total head H_u of the stream could be determined (see eq. 4.1). The empirical relation between the flow rate and the upstream water depth was $h_u = -1.45Q^2 + 0.78Q + 0.013$ (valid for the investigated water depth range, $h_u > 0.015$ m). The water depth h_u at the end of the conveying channel (at the top of the wheel) varied from 0.02 m to 0.09 m, and the stream velocity v_u varied between 0.5 and 1.5 m/s, depending on the flow rate. Therefore, the entry jet velocity v_e ranged between 1.5 and 2.4 m/s. The torque and the rotational speed were detected by the same procedure illustrated for the breastshot water wheel (section 3.1.1).

4.1.2 Experimental results

An error analysis was conducted using the method presented in section 3.1.2. A representative case was defined with $Q = 0.06$ m^3/s, $h_u = 0.09$ m (hence $H_{gr} = 1.55$ m and $P_{gr} = 912$ W), $N = 2.5$ rad/s, and $\eta = 0.8$ (hence $P_{exp} = 730$ W). The accuracy of the head difference estimation is $\delta H_{gr} = 0.0076$ m, $\delta P_{gr} = 12$ W for the power input, $\delta P_{exp} = 15$ W for the power output and $\delta\eta = 0.027$ for the efficiency. These values are lower if compared to their respective measured quantities, hence they can be considered acceptable.

Figure 4.3, Fig. 4.4a and Fig. 4.4b show the experimental power output and efficiency. First of all, two particular rotational speeds can be identified: the *runaway velocity* N_r, when the power output approaches zero ($N_r \simeq 4 - 4.5$ rad/s, or 38-43 rpm); this corresponds to the free wheeling velocity, when no braking torque (except friction) is applied. The second important velocity is the *critical velocity* N_{cr}, when the power output and efficiency begin to decrease almost linearly ($N_{cr} \simeq 2.7$ rad/s, or 26 rpm, or $u_{cr} = 1.8$ m/s). This is due by the sudden increase in volumetric losses at the top of the wheel. However, the critical velocity can only be observed at flow rates bigger than 0.03 m^3/s, to which correspond entry velocity of the jet $1.8 < v_e < 2.4$ m/s, or $0.75 < v_{cr}/v_e < 1$ (the maximum investigated flow rate was 0.137 m^3/s, with an entry absolute jet velocity of 2.4 m/s). Therefore, the power losses increase dramatically and the efficiency reduces once the blade speed approaches 75% of the inflow velocity.

In Williams and Bromley (2000), the maximum limit for the rotational speed of overshot water wheels was identified in $N_{max} = /\sqrt{D}$ (rpm), with the diameter D in meters, obtained equaling the weight of water to the centrifugal force on the

top bucket. This velocity is the approximation of the runaway velocity. Applying this formulation to our case, $N_{max} = 34.9$ rpm or 3.7 rad/s, which is similar to $N_r = 4 \div 4.5$ rad/s. N_{max} is included between N_{cr} and N_r, which is reasonable. N_{max} is a maximum limit for the rotational speed in ideal conditions. It is higher than N_{cr} because in real cases there are also additional power losses and not all the flow rate can enter into the cells. N_{max} is lower than the actual runaway speed N_r: when the intensity of centrifugal force is equal to the gravitational one (that occurs at N_{max}), only in the top bucket the resultant force is zero, since the two forces are parallel. In the other buckets the resultant force is bigger than zero, and the water weight can push the blades.

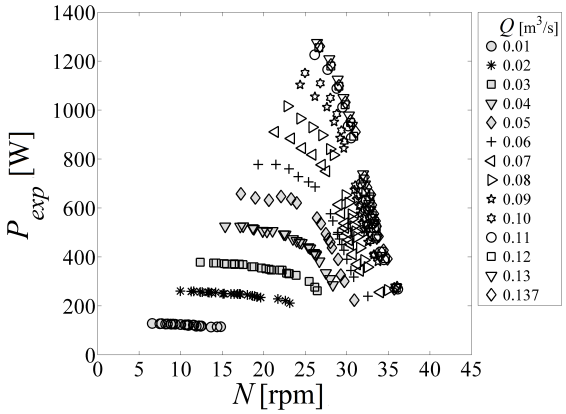

Fig. 4.3. Power output P_{exp} at different flow rates Q and wheel rotational speeds N.

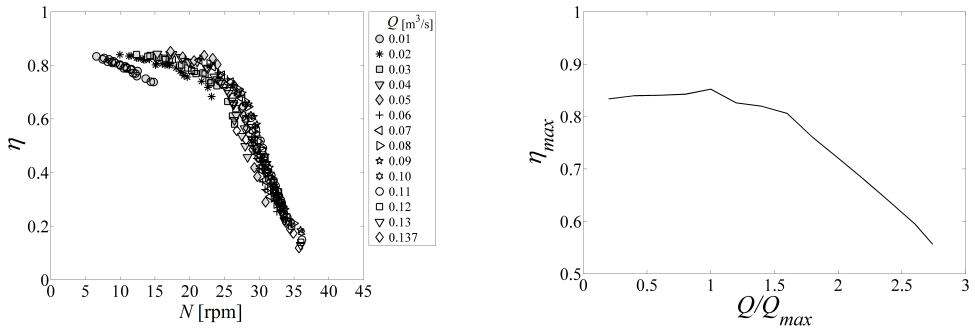

(a) *Efficiency*. (b) *Maximum efficiency*.

Fig. 4.4. (a) The efficiency η versus the rotational speed N, at different flow rates Q. (b) The maximum efficiency versus the dimensionless flow rate Q/Q_{max}, where $Q_{max} = 0.05$ m^3/s is the maximum efficiency flow rate.

In Fig. 4.3 it can be observed that the power output decreases with the increase in the wheel rotational speed; for higher Q and N, most of the water cannot fill

into the buckets, it slips around the external part of the blades and L_{Q_u} increases (as illustrated in Fig. 4.5).

Figure 4.4a shows a constant efficiency of $\simeq 80\%$ with the rotational wheel speed, over a wide range of flow rates (0.01-0.07 m^3/s). In this range the optimal filling ratio (the water volume to the bucket volume) is included between 0.23 to 0.5. The efficiency tends to decrease for $N > N_{cr} = 2.7$ rad/s as a consequence of the increase in volumetric losses at the top of the wheel (that will be estimated in the next section). Figure 4.4b depicts the maximum efficiency versus the dimensionless flow rate, where $Q_{max} = 0.05$ m^3/s is the flow rate corresponding to the maximum efficiency. Figure 4.4b clearly shows that overshot wheels are very suitable hydraulic machines in sites with small and variable water flow, with constant efficiency for a wide range of flow rates. The maximum efficiency is 85% for $Q = 0.05$ m^3/s and then it decreases, due to the increase in the volumetric losses, mainly those at the top of the wheel.

In Müller and Kauppert (2004) a complete and detailed review of old work for overshot water wheels is reported; similar curves of those shown in Fig. 4.4 are illustrated, where the efficiency begins to reduce when the cell speed approaches 80% of the inflow velocity. Therefore, the uppermost wheel tangential velocity should be about 0.75 of the jet absolute velocity. Moreover, Müller and Kauppert (2004) show constant efficiency $\eta > 80\%$ for a wide range of flow rates, up to the flow rate corresponding to the maximum efficiency Q_{max}. The efficiency trend for flow rates higher than Q_{max} was not investigated by Müller and Kauppert, thus our experimental tests can be very useful to complete and detail the characteristic curves of overshot water wheels. Concerning the maximum efficiency, the achieved values are also in agreement with Weidner (1913) and Meerwarth (1935).

4.2 Theoretical model

In this section a theoretical model is developed to estimate the power losses, hence the efficiency of the overshot water wheel.

4.2.1 General theory

Figure 4.5 shows an overshot water wheel with an internal radius R, a rotational speed N and an angular distance between two blades $\beta = 2\pi/n$ where $n = 24$ is the number of blades. The angular position of each blade is θ, where in this case $\theta = 0^\circ$ is the vertical line passing for the rotation axle, while for the

breastshot wheel analysis $\theta = 0°$ was the horizontal line. In the figure, $H_{w,i}$ is the energy head of the flow rate Q_r which spills out the generic bucket i, with L_{Q_r} the volumetric loss during rotation. Q_u is the water loss at the top of the wheel and L_{Q_u} the related power loss. L_{imp} is the hydraulic impact loss and L_g the mechanical friction loss at the shaft. v_u is the upstream velocity and v_d the downstream one. The gray areas represent the water volumes contained in the buckets; their water surface is inclined of $\alpha = \alpha(\theta, N)$ as a consequence of the centrifugal force. In position $\theta = \theta_e = \theta_e(Q, N)$ the water begins to spill out. The arrows represent the water flows, in particular the flow rate Q and the volumetric losses Q_r and Q_u.

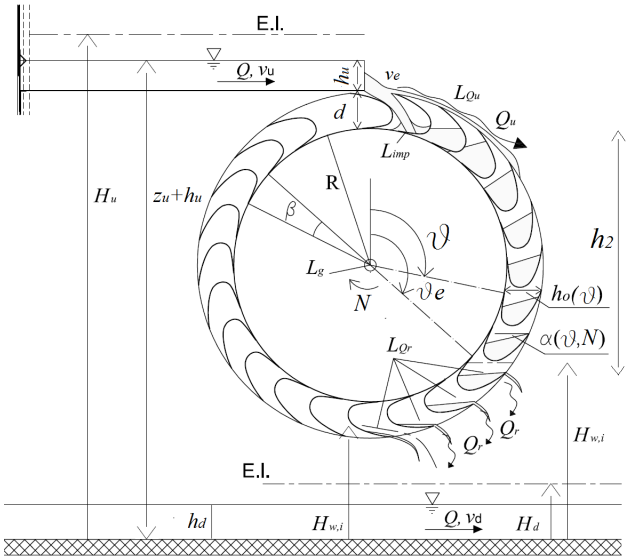

Fig. 4.5. Reference scheme for the overshot water wheel. E.l. is the energy line, Q is the total flow rate, H_u and H_d are the energy heads upstream and downstream of the wheel.

The water jet should enter into each bucket at its natural angle of fall, as a fast and thin sheet; the opening of each bucket is slightly wider than the jet, to ventilate the cells. The jet fills into the buckets impinging on the blades, dissipating a portion of its kinetic energy and generating the impact power loss L_{imp}. A portion of the inflowing water may be also lost, generating a power loss L_{Q_u}. The water volume in the bucket moves then with it at the mean tangential velocity $u = N \cdot (R + d/2)$, where d is the depth of the bucket along the wheel radius. After a rotation to $\theta = \theta_e$ from the starting position (the top of the wheel), the water begins to spill out, generating volumetric losses L_{Q_r}. When the bucket overcomes the lowest point of the wheel ($\theta = \pi$) the emptying process completes.

In the present analysis, we suppose the water inside the cells to be at rest and

the effect of the centrifugal force, which makes the surface profile of the water not to be horizontal, is taken into account.

The power input P_{net} the wheel disposes depends on the hydraulic and geometric boundary conditions and it is expressible by (Fig. 4.5):

$$P_{net} = P_u - P_d = \gamma \cdot Q \cdot H_{net} = \rho g \cdot Q \cdot (H_u - H_d) = \\ \gamma \cdot Q \cdot \left([z_u + h_u] - [z_d + h_d] + \frac{{v_u}^2 - {v_d}^2}{2g} \right) \quad (4.1)$$

where P_u is the power of the flow upstream of the wheel and P_d that downstream of the wheel, $\gamma = 9810$ N/m^3 the water specific weight and Q is the incoming flow rate. $\Delta H = H_u - H_d$ is the net head, v_u and v_d the upstream and downstream water velocity, respectively, and $g = 9.81$ m/s^2 is the gravity acceleration. In our case $v_d \simeq 0$ and the free surface of the tailrace is located just under the bottom of the wheel.

The mechanical power output P_{out} is expressible by:

$$P_{out} = P_{net} - \sum Losses = P_{net} - L_{imp} - L_t - L_g - L_{Q_u} - L_{Q_r} \quad (4.2)$$

where L_{imp} is the power loss occurring in the impact, L_t the impact loss generated when the blades impact into the tailrace water (if the blades are submerged in the tailrace), L_g the mechanical friction loss at the shaft, L_{Q_u} the volumetric loss at the top of the wheel and L_{Q_r} the volumetric loss during rotation. The efficiency η is:

$$\eta = \frac{P_{out}}{P_{net}} = \frac{P_{net} - \sum Losses}{P_{net}} = 1 - \frac{\sum Losses}{P_{net}} \quad (4.3)$$

4.2.2 Power losses estimation

The scope of the following sections will be the estimation of the power losses. Considering the radial symmetry of the wheel, the instantaneous power losses exhibit a period of $T = \beta/N$ (the rotational speed N of the wheel is expressed in rad/s, and β in radiants). To determine the power output P_{out} their average value during T will be considered.

4.2.2.1 Impact losses

Impact losses may occur both at the top of the wheel when the jet enters into the cells, and at the tailrace.

Called $\vec{v}$ the absolute velocity of the water impinging into the blades and $\vec{u}$ the tangential velocity of the blades in the impact point, the relative velocity of the jet is $\vec{w} = \vec{v} - \vec{u}$. The impact power loss can be written as done for impact power losses of breastshot water wheels, hence writing it as a function of the relative flow velocity:

$$L_{imp} = \xi \gamma Q \frac{w^2}{2g} \tag{4.4}$$

where ξ is the impact coefficient and $v_e = \sqrt{{v_u}^2 + 2g(h_u + d/2)}$ is the intensity of the jet absolute velocity; h_u is the water depth in the conveying channel and d the depth of the bucket opening.

In general, the impact torque also contributes to the power generation. This contribution decreases with the wheel rotational speed due to the reduction in the relative velocity. However, during rotation, the jet generally impinges on the external surface of the blades, due to their backward inclination, therefore it is reasonable to assume $\xi = 1$. Moreover, since the contribution of the impact torque to the power generation is related to the kinetic energy (which is much lower than the potential one) and the exchanged kinetic power depends on the relative entry velocity (and not directly on the absolute jet velocity) a different reasonable value of ξ does not affect appreciably the results.

The impact loss at the tailrace (L_t), happens when the blades near the lowest position ($\theta = \pi$) are submerged in the tailrace and their tangential speed is faster than that of the tailrace water. The loss L_t can be expressed as:

$$L_t = \frac{1}{2} C_D \rho (u - v_d)^2 A u \tag{4.5}$$

where v_d is the water velocity at the tailrace under the wheel, C_D the drag coefficient (depending on the shape of the blade) and A the area of the blade exposed to the impact.

4.2.2.2 Mechanical losses

The friction at the shaft supports can be expressed by:

$$L_g = M \cdot N = W \cdot f \cdot r \cdot N = (W_{wh} + W_{wat}) \cdot f \cdot r \cdot N \tag{4.6}$$

where M is the resistance torque due to the friction at the shaft supports, N the rotational velocity of the wheel, $W = W_{wh} + W_{wat}$ the total weight of the wheel, where W_{wat} is the weight of the water in the buckets and W_{wh} is the weight of the wheel, f the friction coefficient and r the shaft level arm.

4.2.2.3 Volumetric losses

Volumetric losses occur both at the top of the wheel (L_{Q_u}) and during rotation (L_{Q_r}).

A portion of the approaching flow rate is lost at the top of the wheel, generating the power loss L_{Q_u}:

$$L_{Q_u} = \gamma \cdot Q_u \cdot (H_u - H_d) \tag{4.7}$$

where Q_u is the flow rate which cannot enter into the buckets and it is a function of the wheel rotational speed and the blades shape. Due to the complex filling and impact process, Q_u is difficult to estimate theoretically. We introduce $\chi = L_{Q_u}/P_{net} = Q_u/Q$ that will be estimated by an optimization process, aimed to minimize the error between the experimental and theoretical power.

Volumetric losses L_{Q_r} occur when water Q_r starts spilling out from the buckets during wheel rotation, and the bucket starts to empty. Since the angular distance between two buckets is β, L_{Q_r} has a periodic cycle of $T = \beta/N$. The instantaneous power loss at time $t = t_j$ is:

$$L_{Q_r}(t = t_j) = \gamma \sum_{i}^{n_b} Q_{r,i} \cdot (H_{w,i} - H_d) \tag{4.8}$$

where $Q_{r,i}$ is the flow rate exiting from each bucket i at time $t = t_j$, whose energy head is $H_{w,i}$, and n_b is the number of the buckets contributing to the outflow.

$Q_{r,i}$ is expressible by:

$$Q_{r,i} = \frac{V(\theta_i, N) - V(\theta_i + d\theta, N)}{d\theta/N} = -N \frac{\partial V}{\partial \theta}\Big|_{\theta=\theta_i} \tag{4.9}$$

where $V(\theta_i, N)$ is the maximum water volume each bucket i can contain in its position $\theta = \theta_i$ for a certain rotational speed N. The average value of L_{Q_r} can be expresses by:

$$L_{Q_r} = \frac{\gamma \int_t^{t+T} \sum_i^{n_b} Q_{r,i} \cdot (H_{w,i} - H_d)}{T} \tag{4.10}$$

In order to avoid an early loss of water, each bucket should only be filled with $30 \div 50\%$ of its volume, so that the outflow starts at a very low level (Müller and Kauppert, 2004).

The spilling out process from a bucket starts at position $\theta = \theta_e$ where $V_{in} = V(\theta, N)$, with V_{in} the water volume which has filled the bucket and $V = V(\theta, N)$ the maximum water volume the bucket can contain (Fig. 4.5); all the buckets beyond the position θ_e contribute to L_{Q_r}.

The volume V_{in} is expressible by:

$$V_{in} = (Q - Q_u) \cdot \beta / N \tag{4.11}$$

while $V = V(\theta, N)$ depends on the geometric shape of the blades and it decreases with the angular position θ. The volume V decreases also with the rotational speed of the wheel, since the centrifugal force inclines the water surface profile of the water volume, as depicted in Fig.4.5.

In this theoretical model, two situations were studied: firstly the effect of the centrifugal force was neglected, then the centrifugal force is taken into account. Figure 4.6 depicts the shape of the blade of the overshot water wheel.

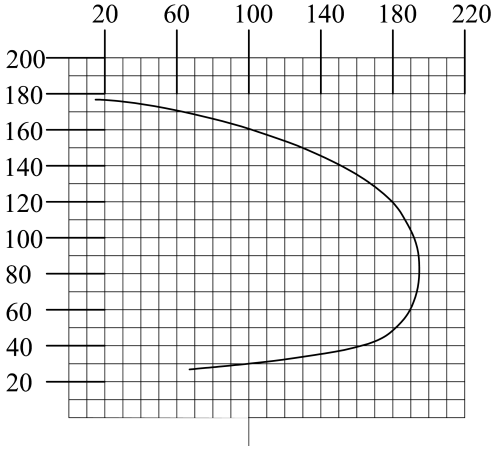

Fig. 4.6. The shape of the blade. The grid units are mm. The vertical line under 100 mm is the radial direction.

Neglecting the centrifugal force and supposing the water in the buckets is at rest, the water surface profile in the buckets is horizontal; in this simplified case,

the maximum water volume V is called $V_s = V_s(\theta)$ and it depends only on the shape of the buckets and on their position θ. Being independent from N, $V_s = V_s(\theta)$ is a characteristic parameter of the overshot wheel and Fig. 4.7 depicts it for the installed wheel. The curve represents the maximum water volume that can be contained inside the bucket at each angular position. The volume V_s reduces drastically after a rotation of $\theta \simeq \pi/2$ rad from the top of the wheel (where the water fills into the bucket and $\theta = 0$).

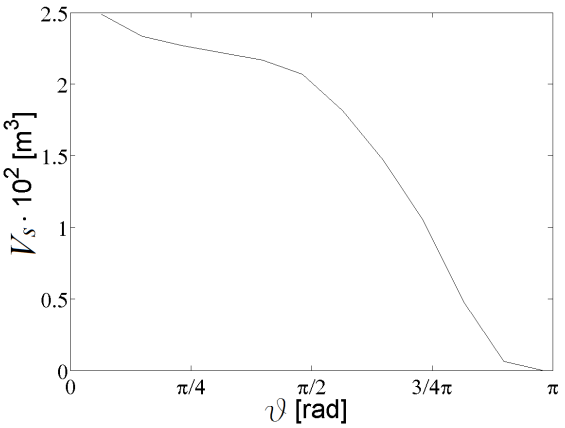

Fig. 4.7. The maximum water volume $V_s = V_s(\theta)$ the bucket can contain for the installed wheel.

When the effect of the centrifugal force is considered, the maximum water volume is $V = V(\theta, N) < V_s(\theta)$, because of the inclined water surface profile inside the buckets. The water surface in each bucket disposes in order to make its profile in each point perpendicular to the total acting force $\vec{F}_t = \vec{F}_c + \vec{F}_g$, where $\vec{F}_c = N^2 e$ is the centrifugal acceleration (force for unit mass) and $\vec{F}_g = \vec{g}$ the gravity acceleration, with e the distance between each point of the water surface in the buckets and the wheel rotation axle. For the sake of simplicity, assuming the water surface profile to be linear and the mean distance $e = \bar{e}$, V can be calculated assuming that V_s reduces of a quantity of about $V_l \simeq 1/2 b {h_o}^2 \sin\alpha$: $h_o = h_o(\theta)$ is the maximum horizontal length of the water surface inside the buckets, $\sin\alpha = F_c \sin\theta / F_t$ with $\alpha = \alpha(\theta, N)$ is the inclination of the water surface due to the centrifugal effect (in the point where the distance is $\bar{e}$ from the axle) and b the width of the buckets (Fig. 4.5). The higher N the higher α and the reduction of V, so that $V = V_s - V_l = V(\theta, N)$.

4.2.3 Interpretation of past formulations

As done for the breastshot water wheel, also in this case some past theoretical formulations are reported, from Garuffa (1897) and Church (1914). However, these Authors neglected in their formulation the volumetric losses at the top of the wheel, that are very important and significant at high flow rates, as discussed later.

In Garuffa (1897) the following formulation is considered.

$$P_{out,G} = P_{gr} - T_{imp} - T_g - \gamma Q \left(h_a + \frac{u^2}{2g} \right) \tag{4.12}$$

where $T_{imp} = 0.1\gamma Q \frac{{v_u}^2}{2g} + \gamma \frac{w^2}{2g}$ is the impact power loss, with v_u the horizontal flow velocity, T_g is the friction loss as calculated in eq. 4.6 and $\gamma Q(h_a + \frac{u^2}{2g}) = \gamma \sum_i^n Q_{r,i} \cdot (H_{w,i} - H_d)$ has to be interpreted as L_{Q_r} (eq.4.8): hence h_a is the head which is lost from the flow rate Q. Therefore, the only differences between this formulation and eq.4.2 are: (1) the additional impact power loss (second term on the right hand side), that anyway is negligible because it is about 1/150 of the potential energy of water (in eq.4.2 a simpler way for considering the inclination of the water surface in the bucket is also illustrated), (2) in eq.4.12 the volumetric losses at the top of the wheel are not considered.

Instead, in 1914, Church proposed the following formulation.

$$P_{out,C} = \rho g \cdot Q \cdot \left[\frac{(v_e \cdot cos\alpha - u)u}{g} + h_2 + \delta h_3 \right] \tag{4.13}$$

h_2 is the distance between the free surface of the water volume in the first bucket and the free surface in the bucket before when the emptying process starts (Fig.4.5; h_3 is the distance between the latter free surface and the tip of the blade just emptied, and $\delta = 0.5$. Therefore, $\rho g Q(1-\delta)h_3 = L_{Q_r}$. This coefficient will be better estimated for the investigated wheel. Also *Church* did not consider the volumetric losses at the top of the wheel.

In the next section, the coefficient δ and the head h_a will be estimated for the investigated wheel.

4.2.4 Theoretical results

Figure 4.8 depicts the theoretical power output (P_{out}) versus the experimental one (P_{exp}), assuming negligible the centrifugal force, i.e. $Q_u = 0$ and $L_{Q_u} = 0$. At low flow rates ($Q < 0.03$ m^3/s) the hypothesis for the calculation of L_{imp}, L_g

and L_{Q_r} are well posed. Indeed the points on the graph are disposed along the bisecting line. In these cases the entirety of the flow rate enters into the buckets and after a little rotation the water can be considered at rest, as confirmed by the experimental tests. At $Q = 0.03$ m^3/s the points starts to not be perfectly disposed along a line.

At $Q > 0.04$ m^3/s and high rotational speeds (at high rotational speeds correspond lower values of measured power output P_{exp}) the points representing P_{out} dispose over the bisecting line, being overestimated with respect to P_{exp}. In these cases the overestimation of the power output can be attributed to the neglected volumetric losses L_{Q_u}; hence the unknown volumetric losses Q_u can be estimated by an optimization process. The most reliable value of Q_u for each case is that value which minimizes the difference between the theoretical power P_{out} and the experimental one P_{exp}.

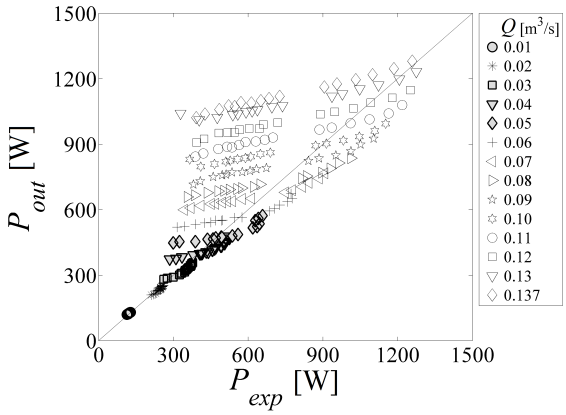

Fig. 4.8. Theoretical power results (P_{out}) versus experimental ones (P_{exp}) for different flow rates Q, assuming $L_{Q_u} = 0$; it is a very good assumption for small flow rates (Q <0.04 m^3/s).

Numerically speaking, after that a value for the outflow Q_u is assumed, the related power loss L_{Q_u} can be calculated by eq. 4.7 and, when the position θ_e where $V_{in} = V(\theta, N)$ is deducted, the outflow Q_r from each of the n_b buckets at $\theta > \theta_e$ can be calculated by eq. 4.9. Then, by eq. 4.8 and eq. 4.10 it is possible to evaluate L_{Q_r} and by eq. 4.6 to calculate L_g, being known W_{wat}. P_{out} can be then calculated by eq. 4.2. Instead, for the lowest N (or the biggest P_{exp}) the estimated power output P_{out} is lower than the experimental one; it happens because of the more pronounced oscillation motion inside the buckets, not considered in this thesis caused by the higher values of the relative jet velocity.

From the theoretical results it can be deduced that the bigger Q the higher the power losses. The volumetric losses L_{Q_r} and L_{Q_u} increase with Q because

the spilling out process happens early and the portion of Q which cannot fill into the buckets enhances. The impact loss L_{imp} enhances as a consequence of the increase in the jet velocity and flow rate, and friction losses L_g increase as a result of the increase in the water weight in the buckets. Anyway, L_g is negligible, being less than 0.2% of the power input. The tailrace loss is considered to be $L_t = 0$ for these experiments, since the wheel is over the free surface of the tailrace.

The dependency from the rotational velocity N is instead more interesting. Fig. 4.9 shows the trend of $\chi = L_{Q_u}/P_{net}$ with N; for $N > N_{cr}$ (taken as $\simeq 2.7$ rad/s), χ increases linearly. The trend equation for χ is:

$$\begin{cases} \chi = \frac{L_{Qu}}{P_{net}} \simeq 0 & \text{for } N < N_{cr} \\ \chi = \frac{L_{Qu}}{P_{net}} = 2.0 \cdot \left[\frac{N}{N_{cr}} - 1\right] & \text{for } N > N_{cr} \end{cases} \tag{4.14}$$

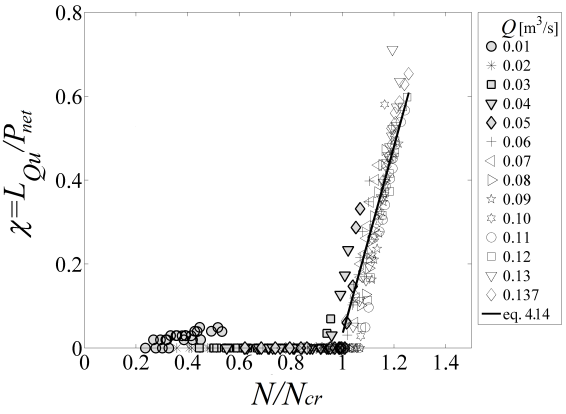

Fig. 4.9. Dimensionless volumetric loss $\chi = L_{Q_u}/P_{net}$ versus the dimensionless rotational speed of the wheel N/N_{cr}, for different discharges Q; L_{Q_u} is the volumetric loss due to the water which cannot fill into the buckets, P_{net} the available power input and $N_{cr} = 2.7$ rad/s the critical velocity.

Figure 4.10 depicts the trend of L_{Q_r}/P_{net}. For $N < N_{cr}$ ($\simeq 2.7$ rad/s) the faster the rotational speed the bigger L_{Q_r}; although the water volume V_{in} which fills into the buckets decreases with N, the increasing effect of the centrifugal force becomes more important and the spilling out begins earlier. The maximum calculated value of the water surface inclination inside the buckets caused by the centrifugal effect is $\alpha \simeq 40°$. Then, at $N = N_{cr}$, L_{Q_r}/P_{net} begins to decrease sharply, due to the fact that the rapid enhancement in L_{Q_u} reduces considerably V_{in}. For very slow rotational speeds the entirety of the flow rate fills into the bucket

and V_{in} increases, but the effect of the centrifugal force reduces. For $N \to 0$ the buckets fill completely and the emptying process starts immediately from the initial position.

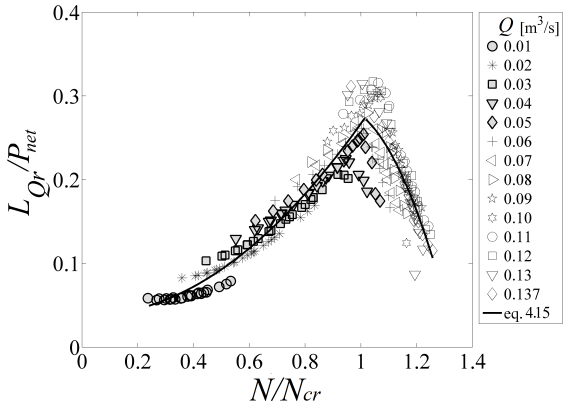

Fig. 4.10. Dimensionless volumetric loss L_{Q_r}/P_{net} versus the dimensionless wheel rotational speed N/N_{cr}, at different discharges Q; L_{Q_r} is the volumetric loss from the buckets during rotation, P_{net} the available power input and $N_{cr} = 2.7$ rad/s the critical velocity of the wheel.

The trend equation of L_{Q_r}/P_{net} is:

$$\begin{cases} \frac{L_{Q_r}}{P_{net}} = 0.20 \cdot \left(\frac{N}{N_{cr}}\right)^2 + 0.05 \cdot \frac{N}{N_{cr}} + 0.02 \quad \text{for } N < N_{cr} \\ \frac{L_{Q_r}}{P_{net}} = -1.26 \cdot \left(\frac{N}{N_{cr}}\right)^2 + 2.19 \cdot \frac{N}{N_{cr}} - 0.66 \quad \text{for } N > N_{cr} \end{cases} \tag{4.15}$$

This is also confirmed plotting the coefficient δ used by *Church* in eq.4.13 (Fig.4.11), using in the calculation the head $h_3 + u^2/2g$ instead of h_3 only. δ is obtained for the investigated wheel imposing $\rho g Q(1-\delta)h_3 = L_{Q_r}$. As can be observed in Fig.4.11, the coefficient decreases with the rotational speed; this means that the power losses increase with the wheel speed (since δ indicates how much of the head is exploited during the emptying process). The average value is $\delta = 0.34$, and $0.4 < \delta < 0.6$ in the range of approximately 0.9÷1.5 rad/s. This can be also observed plotting the head h_a of eq.4.12, versus the rotational speed at different flow rates. The lost head h_a increases with the rotational speed (Fig.4.12). It is important to remember that this is a virtual head, as well as the average head that would be lost from the net flow rate $(Q - Q_u)$, in order that the

related power loss would assume the same value of the real power loss. Instead, in the real case, the flow rate inside the bucket spills out from it progressively, hence not the entirety of $Q - Q_u$ is lost immediately.

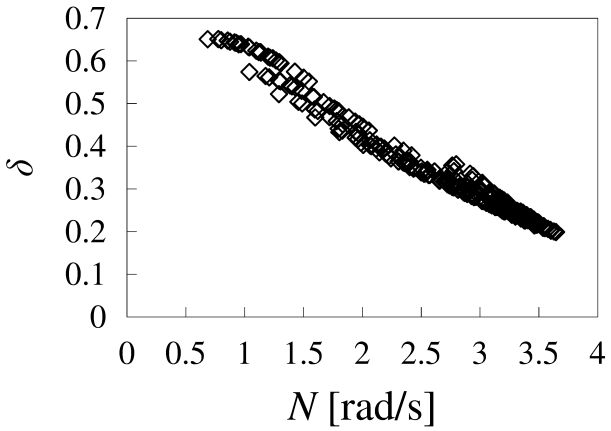

Fig. 4.11. *Church* coefficient δ versus the rotational speed of the wheel, applying is method to the experimental results.

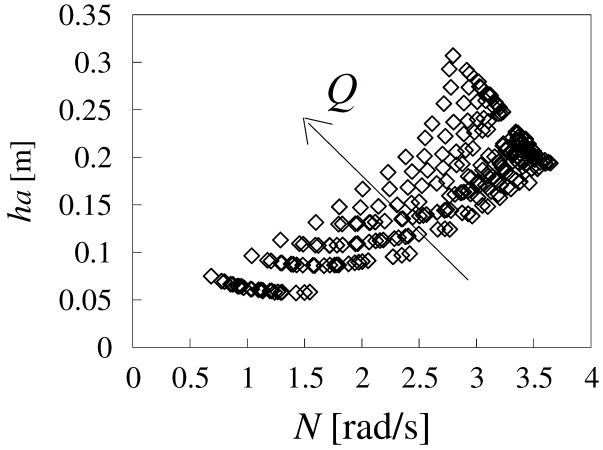

Fig. 4.12. *Garuffa* head versus the rotational speed of the wheel.

Figure 4.13 depicts the trend of L_{imp}/P_{net} versus N/N_{cr}. L_{imp}/P_{net} increases with N, and at $N > N_{cr}$ it decreases, since the enhancement in L_{Q_u} reduces the flow rate of the jet which impinges on the wheel. For $N \to 0$ the entirety of the discharge fills into the bucket and $u \to 0$. The relative velocity becomes $\vec{w} = \vec{v}$ and, assuming $\xi = 1$, $L_{imp}/P_{net} = \frac{{v_u}^2/2g+h_u+d/2}{\Delta H}$, where $v_u = v_u(Q)$, $h_u = h_u(Q)$ and $\Delta H = \Delta H(Q)$ (because $\Delta H = \Delta H(v_u, h_u)$). In correspondence of $N/N_{cr} = 1$ there is the maximum, which value is 12%, lower than that for $L_{Q_r}/P_{net} = 32\%$.

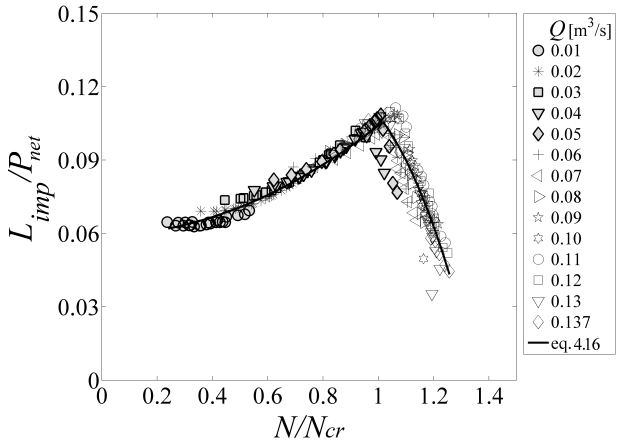

Fig. 4.13. Dimensionless impact loss L_{imp}/P_{net} versus the dimensionless rotational speed of the wheel N/N_{cr}, at different discharges Q. L_{imp} is the impact loss, P_{net} is the power input and $N_{cr} = 2.7$ rad/s the critical rotational speed of the wheel.

The trend equation for L_{imp}/P_{net} is:

$$\begin{cases} \frac{L_{imp}}{P_{net}} = 0.018 \cdot \left(\frac{N}{N_{cr}}\right)^2 + 0.035 \cdot \frac{N}{N_{cr}} + 0.05 \quad \text{for } N < N_{cr} \\ \frac{L_{imp}}{P_{net}} = -0.32 \cdot \left(\frac{N}{N_r}\right)^2 + 0.54 \cdot \frac{N}{N_r} - 0.11 \quad \text{for } N > N_{cr} \end{cases} \tag{4.16}$$

Figure 4.14 illustrates the increase of L_g/P_{net} with N. Although W_{wat} in eq. 4.6 decreases with N, $L_g/P_{net} = M \cdot N/P_{net}$ increases with N; this happens because W_{wat} is negligible with respect to the weight of the wheel W_{wh}. For $N \to 0$ L_g tends to 0. The trend equation for L_g/P_{net} is:

$$\frac{L_g}{P_{net}} = 0.00065 \cdot \left(\frac{Q}{Q_{max}}\right)^{-1} \cdot \left(\frac{N}{N_{cr}}\right) \tag{4.17}$$

and it is affected by the wheel rotational speed N and the flow rate Q.

Figure 4.15 depicts the theoretical powers calculated by eq. 4.2 versus the measured ones and the results are well aligned along the bisecting line. At low flow rates and $P_{exp} < 800$ W the model predicts the power output very well and the highest errors are related to high discharges (corresponding to the lowest efficiency); it is a satisfactory result, since overshot water wheels are used in sites

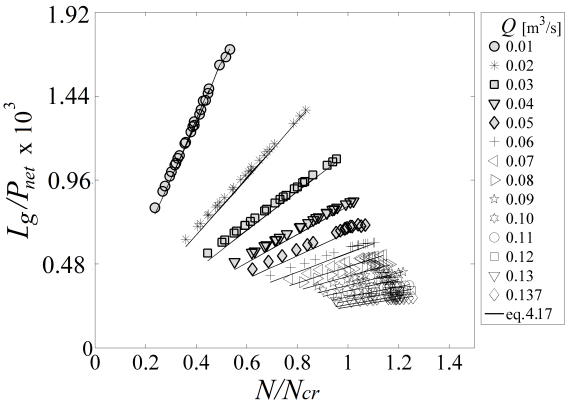

Fig. 4.14. Dimensionless friction loss L_g/P_{net} versus the dimensionless rotational speed of the wheel N/N_{cr}, for different discharges Q. L_g is the friction loss, P_{net} the power input and $N_{cr} = 2.7$ rad/s the critical rotational speed of the wheel.

with low discharges.

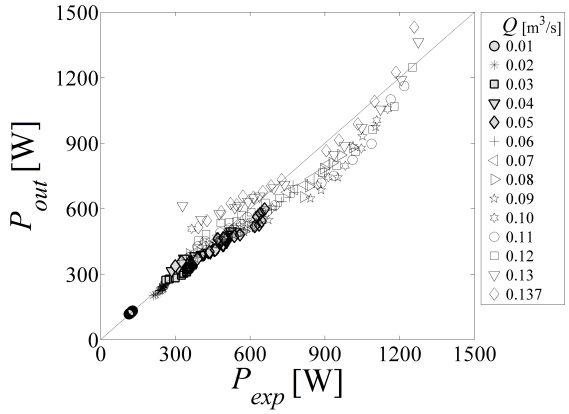

Fig. 4.15. Estimated power output P_{out} versus the experimental one P_{exp} at different flow rates Q. The average error is 8.2%.

The global average error among the experimental powers (P_{exp}) and the theoretical ones (P_{out}) can be expressed as:

$$\bar{er} = \frac{1}{n_p}\sum_{j=1}^{n_p} er_j = \frac{1}{n_p}\sum_{j=1}^{n_p} \frac{|P_{out_j} - P_{exp_j}|}{P_{exp_j}} \tag{4.18}$$

where n_p is the total number of the experiments and P_{out} is calculated by eq.4.2. Expressing the volumetric losses L_{Q_u} by eq.4.14, $\bar{er} = 8.2\%$.

Imposing the efficiency η in eq. 4.3 equal to zero and substituting in it eq. 4.14, 4.15, 4.16, 4.17 for $N > N_{cr}$, it is possible to obtain the value of N corresponding to the runaway velocity N_r, for $Q \geq 0.03$ m^3/s, as a function of the flow rate.

$$\frac{P_{net} - L_{imp} - L_g - L_{Q_u} - L_{Q_r}}{P_{net}} = \\ = a - \left(\frac{N_r}{N_{cr}}\right) \cdot \left[\left(b + \frac{c}{(Q/Q_{max})}\right) - d\left(\frac{N_r}{N_{cr}}\right)\right] = 0 \quad (4.19)$$

In our case, using the equations and coefficients found for the power losses, the constants in eq.4.19 assume the following values: a = 3.76, b = 4.74, c = 0.00065 and d = 1.58. $N_{cr} = 2.7$ rad/s and $Q_{max} = 0.05$ m^3/s is the flow rate at the maximum efficiency. The obtained solution N corresponds to N_r, when the total extracted power from the water flow is dissipated by friction and other losses. Eq. 4.19 can be solved analytically. The runaway velocity N_r depends slightly on the flow rate, since it appears only in eq.4.17. $N_r = 4.05 \div 4.11$ rad/s as confirmed by the experimental results (Fig. 4.3 and Fig. 4.4a).

Table 4.1 depicts the minimum and maximum values for each power loss, as a percentage of the power input. L_{Q_u}/P_{net} represents the most significant power loss for $N > N_{cr}$. L_{Q_r}/P and L_{imp}/P exhibit a maximum of 32% and 12% at $N = N_{cr}$, respectively; L_g is the smallest one. All the power losses depend strictly on the rotational speed N. The faster N the bigger L_{Q_u} and L_g, while for L_{Q_r} and L_{imp} there is a maximum at $N = N_{cr} \simeq 2.7$ rad/s. The increase in the flow rate Q makes all the power losses increase.

Table 4.1. Minimum and maximum value of the dimensionless power losses.

L/P_{net}	L_{imp}/P_{net}	L_{Q_u}/P_{net}	L_{Q_r}/P_{net}	L_g/P_{net}
Min [%]	3.5	0	5.6	0.0
Average [%]	8.3	14.5	18.5	0.06
Max [%]	11.1	71.1	31.7	0.17

The identified final equations may not be valid for overshot wheels differently sized, while the theoretical model continues to remain reliable. Instead, the estimation of the top volumetric losses is relative to the investigated water wheel and for its blades shapes. It is not reliable for being applied in other blades geometric configurations. However, water wheels should operate in their optimal

performance range, when such volumetric losses are negligible, hence at rotational speeds lower than the critical speed. In this range, the top volumetric losses are practically zero, and the theoretical model performs well.

In order to reduce the power losses and to increase the performance of the wheel, it is necessary to reduce mainly L_{Q_u}, for example by recovery systems for the lost flow rate (as done in Wahyudi et al., 2013), or by the improvement of the blades geometry to reduce both L_{Q_u} and L_{Q_r}. The former aspect will be investigated by numerical simulations in section 4.4.

4.3 Dimensional analysis

Applying the dimensional analysis already used for the breastshot wheel, it is possible to determine a mathematical law that is able to predict the maximum power output at each flow rate (Vidali et al., 2016). The dimensionless law used for the breastshot wheel was:

$$\frac{P_{out} H_g^4}{\rho Q^3} = f\left(\frac{\mu H_g}{\rho Q}\right) \rightarrow P^* = f(1/Re) \tag{4.20}$$

In our case (the overshot water wheel) H_g is same as the diameter. Plotting the dimensionless power output (the so called Newton number) versus the Reynolds number, two possible laws can be interpolated from the data: a power law and a polynomial one.

Using the power law, the previous equation becomes:

$$P^* = \frac{P_{out} {H_g}^4}{\rho Q^3} = \psi_3 \left(\frac{\mu H_g}{\rho Q}\right)^{\psi_4} \tag{4.21}$$

where $\psi_3 = 68136979762148$ and $\psi_4 = 2.10276$

Using the polynomial law:

$$P^* = \psi_5 (1/Re)^2 + \psi_6 (1/Re) + \psi_7 \tag{4.22}$$

where $\psi_5 = 24318980893542.4$, $\psi_6 = 54104958$ and $\psi_7 = -1174$.

Figure 4.16 depicts the power output estimated by the dimensionless laws versus the experimental power output; for each flow rate the maximum power is considered. As can be observed, the model well estimates the maximum power output; at the highest power output the accuracy is lower since the larger volumet-

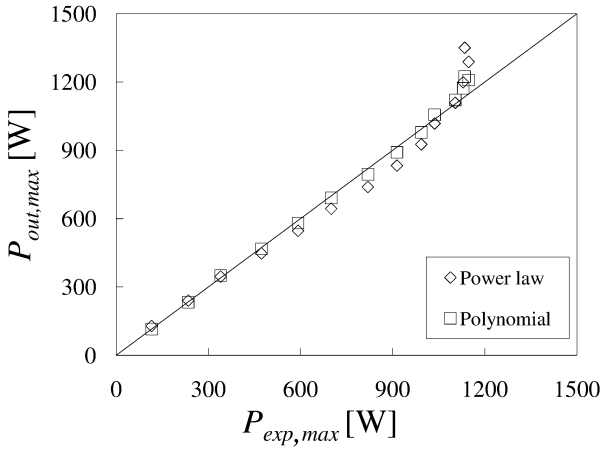

Fig. 4.16. Calculated power output versus the experimental one. For each flow rate, the maximum power was considered.

ric losses complicate the hydraulic behavior. While the power input increases due to the increase in the flow rate, the experimental power output remains constant, due to the volumetric losses. Therefore, in the present case this law should be used only for $Q < 0.110$ m^3/s, because for higher flow rate the dimensionless law does not predict accurately the power output.

4.4 Numerical analysis

In the previous sections, it has been shown that at flow rates higher than the maximum optimal one, the efficiency of overshot water wheels reduces almost linearly as flow rate continues to increase. This is due by the fact that not the entirety of water is exploited from the top of the wheel, and a portion of flow rate is lost with the formation of splashes and water droplets. As a consequence, there is the need of improving the efficiency in these conditions: this scope is addressed using CFD (Computational Fluid Dynamic) tools.

Therefore, the first aim of this section is to investigate the overshot water wheel by 3D CFD simulations, in order to shed more light on its hydraulic behavior. An higher flow rate than the optimal one will be investigated (there is the need to improve the efficiency at these flow rates). An improved design which can be applied to all overshot water wheels is investigated by CFD simulations, and the performance will be compared with the performance of the original design. Future work will be carried out to investigate more in detail the improved design.

4.4.1 Improved design

The proposed modified design of the overshot water wheel (Fig.4.17) consists in a wall located around the periphery of the wheel, with the goal of reducing the volumetric losses and improving the wheel efficiency. The design of the wall is conceived in order to not affect the upstream conditions, guaranteeing atmospheric pressure at the top of the wheel. If the previous condition would not be satisfied, we may deal with a pressurized turbine (similar to *Francis* turbine) and not with a gravity water wheel, that would be beyond the purpose of the present study. Therefore, the clearance between the wall and the wheel at the top should ensure that the wall does not enter in contact with the upstream water flow; in our case this distance was chosen as 0.16 m. Such configuration is led by the fact that it is essential to not affect the upstream conditions when civil works are made on existing water wheels. Instead, the gap between the wall and the wheel is 0.01 m in the lowest half of the wheel; the gap is needed to avoid friction between the rotating wheel and the wall, while minimizing the flow through the gap (thus the volumetric losses); the smaller this gap, the lower the volumetric losses through the wheel. Generally a gap of 0.01 m is adopted between breastshot/undershot water wheels and the curb below them (independently from the diameter), so a gap of 0.01 m was here adopted. The radius of the portion of the wall in the lowest half of the wheel is $R_{wall} = R_{wheel} + 0.01$ m, while the wall in the upper part of the wheel does not require a particular shape; the only advice is that it has to be curved, linking the top edge of the wall (where there is the clearance of 0.16 m) to the circular portion of the wall in a gentle way.

This additional wall is useful because it readdresses the water which would spill out from the buckets into the wheel, reducing the volumetric losses. It can be a good strategy to increase the performance of overshot water wheels at flow rates higher than the maximum optimal one, thus when a portion of the flow rate does not fill the buckets, generating volumetric losses. The wall can be a good strategy also when the bed of the conveying channel is quite distant from the top of the wheel; in this case, the impact between the water jet and the blades is very significant and a portion of water spills out from the buckets generating volumetric losses. Then, considering that the wall can be done with a simple steel plate, the additional cost is negligible with respect to the total cost of the installation. When instead dealing with wheels already in operation (whose design has to be improved when new bigger flow rates are available), this strategy can be considered a cost effective improvement.

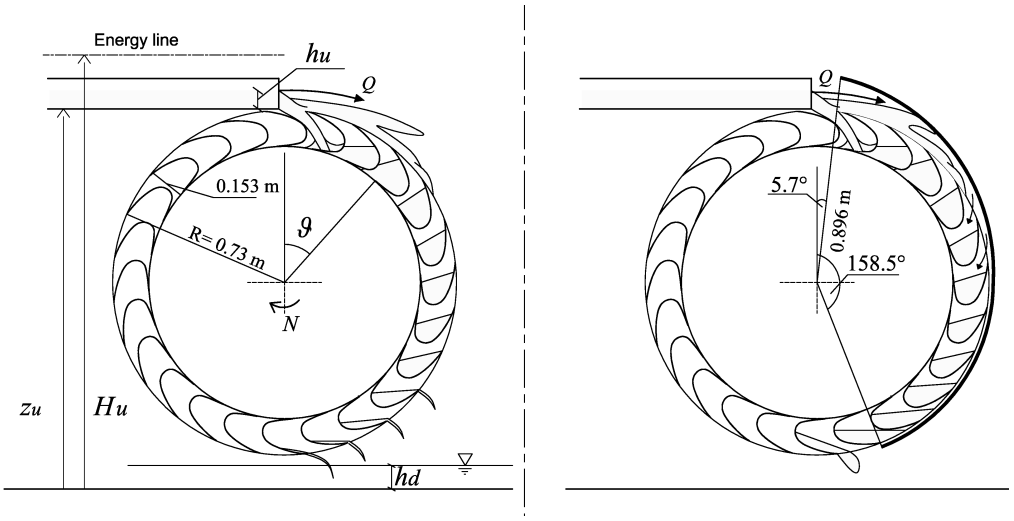

Fig. 4.17. The original water wheel on the left and the modified configuration on the right. The additional wall (on the right) recovers and re-addresses the water into the buckets.

4.4.2 Numerical simulations: geometry and mesh

The computational domain is composed of two subdomains; the stationary domain and the rotating domain of the wheel, connected together through interface surfaces.

The wheel is meshed with prismatic elements of a maximum edge dimension of 0.015 m. Two additional simulations were carried out using more refined meshes in the bucket containing the monitored blade (this bucket can be called *investigated* bucket). The first mesh with elements of 0.01 m (coarse mesh c) in the investigated bucket and in the previous two and next two buckets. Instead, the investigated bucket using the finest mesh was meshed with elements of 0.005 m, that reduces to 0.002 m in contact with the blade (fine mesh f). This mesh is one order of magnitude smaller than the mesh successfully used in Quaranta and Revelli (2016b). The mesh elements were 0.005 m also in the bucket just after and before the investigated one. In Fig. 4.19 it is possible to observe the three more refined buckets (the investigated bucket, the bucket after it and the bucket before it). The mesh is 0.005 m in the three buckets, and the investigated bucket is the central one. Furthermore, when the finest mesh is used, the bucket before and the bucket after the three previous ones are meshed with elements of 0.01 m.

The external domain is meshed with tetrahedron and cubic elements, whose maximum edge dimension ranges from 0.01 m near the wheel, up to 0.1 m at its boundaries (Fig.4.18). The mesh size at the interface between the rotating

wheel and the domain in contact with the wheel is the same on each side, in order to reduce numerical dissipation. In the other interfaces (those between the stationary air domains, the mesh dimension transition is sharp in order to stabilize the solution). Figure 4.19 illustrates the mesh of the improved design.

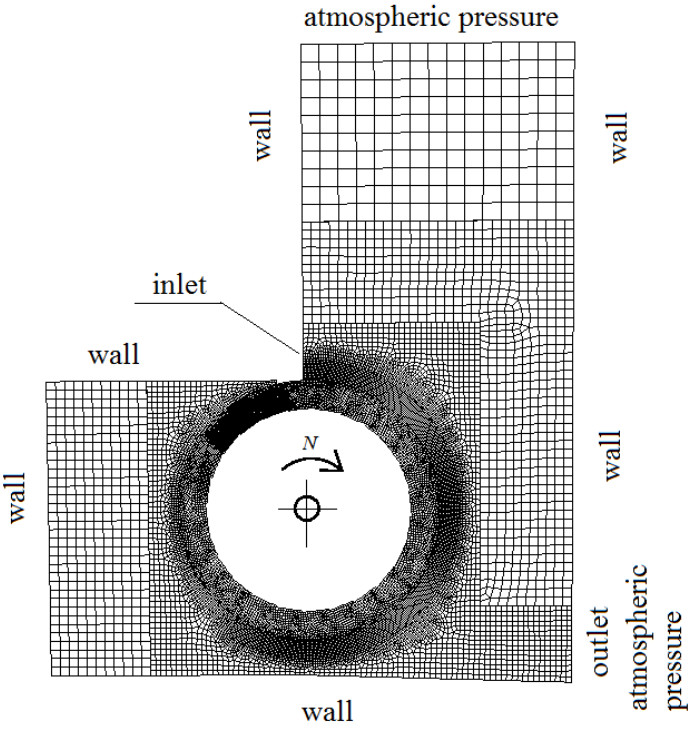

Fig. 4.18. The computational domain of the rotating wheel and the external air domain. The wheel is meshed with finer elements. The boundary conditions are also depicted. The picture refers to the water wheel in the original configuration.

4.4.3 Numerical setup

The same numerical model used for the breastshot water wheel is here used, thus refer to section 3.4.1.1 for the solved equations.

Concerning with the boundary conditions, the water depth h_u and the average velocity v_u at the inlet were imposed (uniform profile, with *no slip* conditions at the channel walls). The velocity was obtained dividing the flow rate by the wet area $A = B \cdot h_u$, where B is the channel width and h_u the water depth, from experiments. At the inlet, a fixed value of the turbulence intensity $I = 0.05$ and a fixed value of the turbulent viscosity ratio $\mu_t/\mu = 10$ were specified, where μ

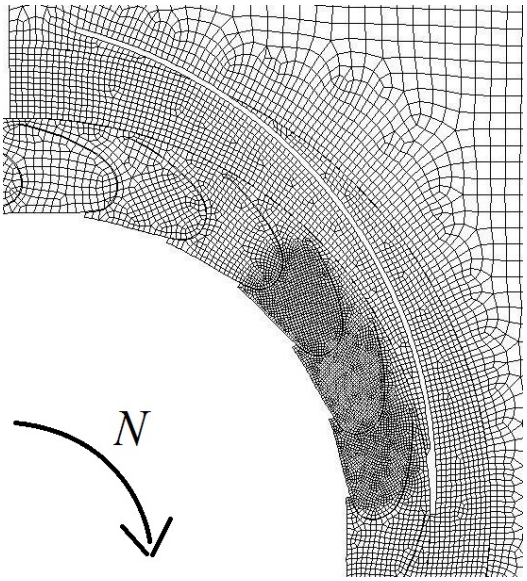

Fig. 4.19. The computational domain of the rotating wheel and the external air domain with the wall. The domain with the monitored blade is meshed with a finer mesh.

is the water dynamic viscosity. These values are generally fixed by default and a literature review confirms them (Pujol et al., 2010; Quaranta and Revelli, 2016b). At the external surfaces of the outer domains the wall boundary conditions are imposed (reducing the volume of the computational air domain, which is out of our interest), while at the top and at the outlet the atmospheric pressure is imposed. The fraction volume of water and mixture velocity were imposed equal to zero throughout the domain, except at the inlet. The gravity acceleration was 9.81 m/s^2 in the vertical direction. In order to reduce computational time, only half width of the wheel was simulated; on the vertical symmetry plane (the vertical plane perpendicular to the rotation axle, which divides the wheel in two symmetric vertical parts) a symmetry boundary condition was imposed. At the walls of the blades surfaces, wheel and channel bed, the no slip boundary condition was adopted.

4.4.4 Numerical results

4.4.4.1 Post-processing and accuracy of the numerical results

The total number of mesh elements used for the overshot water wheel is lower than the respective number used for the breastshot water wheel, since the domain is smaller. Each time step took approximately 80 seconds in a processor at 2.40 Ghz with 8 Gb RAM, for a total time of 5 days for simulation.

During each simulation, the torque at the shaft experienced by a blade was monitored, as shown in Fig.4.20. Considering that 12 blades contribute to the torque when the wheel is working, the average torque $\bar{C}$ can be calculated as:

$$\bar{C} = \frac{1}{T} \int_{t_i}^{t_f} C(t) \partial t \tag{4.23}$$

where $C(t)$ is the shaft torque experienced by the monitored blade at time t, $T = \beta/N$ is the temporal distance between two buckets (β [rad] is the angular distance between two buckets) and t_i and t_f are the initial and final time, respectively, between which the torque experienced by the blade is different from zero. When the considered blade starts to interact with the flow, the downstream buckets have already started to interact with the flow. The numerical power output was obtained multiplying the torque by the rotational speed $P = \bar{C} \cdot N$ (friction at the bearings is negligible).

In order to test the accuracy of the numerical solution, two meshes were tested. Considering the original water wheel, Tab.4.2 illustrates the working conditions of the simulated case and the numerical torque at the shaft (C). The agreement between the CFD results and the experimental ones is very good (discrepancy smaller than 3.1%), as illustrated in Tab.4.2; hence the CFD model is able to capture the main hydraulic characteristics of the problem. The differences between the results with different meshes are negligible, thus they can be considered of the same order of magnitude of the error generated in the elaboration of the results.

Table 4.2. Simulations and results for the original wheel without the peripheral wall: flow rate Q, upstream water depth h_u, rotational speed N and experimental power output P_{exp}. For the numerical results on the power output P, c refers to the coarse mesh and f to the finer mesh.

Variable	Q	h_u	N	C_{exp}	C^c	C^f
Units	[m^3/s]	[m]	[rad/s]	[Nm]	[Nm]	[Nm]
	0.137	0.081	2.7	425	412	411

When the water flow starts to interacts with the blades, the generation of a lot of splashes and water droplets occurs. Furthermore, the formation of jets and splashes inside the buckets, with mixing of air and water (Fig.4.21b), complicates the hydraulic behavior.

The hydraulic behavior of overshot water wheels is hence more complicated than stream water wheels (Akinyemi and Liu, 2015) and breastshot water wheels (Quaranta and Revelli, 2016b), which have been already investigated by CFD

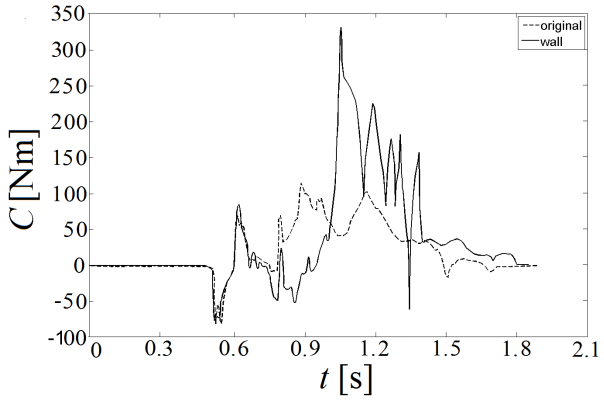

Fig. 4.20. The shaft torque exerted on a blade over the time, for the original wheel and for the configurations with the wall. The trend is quite jagged because of the pronounced oscillations of the water inside the buckets.

simulations. Anyway, considering the validation reported in Tab.4.2, the achieved results can be considered satisfactory, and accurate enough to compare the original design with the improved new one.

4.4.4.2 Description of the results and new design

Referring to Fig.4.20, it is possible to see the torque during the time, both for the original and for the improved design, using the finer mesh. In Tab.4.3 the power output and efficiency results are reported and compared each other.

Table 4.3. Numerical results (using the finer size mesh) for the original configuration and for the improved design (power output and efficiency).

Variable	Q	P^f	η^f	${P_{wall}}^f$	${\eta_{wall}}^f$	$\frac{\eta^f_{wall}-\eta^f}{\eta^f}$
Units	[m^3/s]	[W]	[-]	[W]	[-]	[-]
	0.137	1109	0.48	1791	0.77	0.64

Considering the torque curve of the original design in Fig.4.20, when the blade begins to interact with the water, a portion of the flow fills the buckets, whereas a larger portion runs through the external surfaces of the blades, initially providing a negative torque, due to the backward inclination of the blades. An amount of this external flowing water enters into the buckets after a blade rotates $\theta \simeq 50°$ from the initial position, Fig.4.21a ($\theta = 0°$ is the position where the blade is

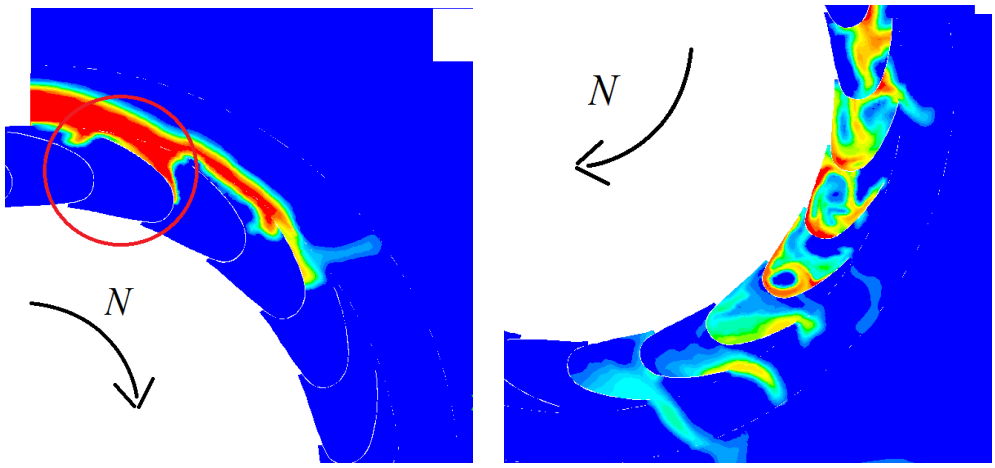

(a) (b)

Fig. 4.21. Contour of volume fraction for the original water wheel on the symmetry plane (normal to the rotational axis): red corresponds to only water present in the cells and blue to air. The transition between the two colors indicates the free surface. In figure (a), the water which flows externally along the blade exerting a negative torque is circled.

over the rotation axle of the wheel). It means that not the entirety of the water is actively exploited from the top of the wheel, thus the efficiency decreases. A certain amount of water is lost, flowing outside from the wheel. The maximum torque occurs when the blade has undergone a rotation of approximately ninety degrees from the initial position. In the optimal position the moment arm is the longest. In the lowest part of the wheel, the buckets begin to empty (Fig.4.21b).

When the wall is added, the interaction does not change at the beginning: also in the modified design, the blade experiences a negative torque. The behavior changes after about 0.8 s, when the bucket begins to interfere with the water which has been recovered by the wall, and which is flowing through the gap between the wall and the wheel (Fig.4.22). The blade experiences then a negative torque, since the cumulated water in the gap brakes the motion of the blade. At $t = 1$ s the torque becomes positive, since the pressure generated by the water in the gap is now exploited by the blade. The blade is pushed not only by the water weight in the bucket, but also by the hydrostatic pressure inside the gap. This is well depicted in Fig.4.23b, where the overpressure is shown. The efficiency improves noticeably, of more than 50% (Tab.4.3).

Hence the hydraulic interaction between the blades and the flow changes, and the useful effect of the new configuration is clearly evident: the volumetric losses decrease and the global effect is a torque improvement (Fig.4.21). The wall is designed in order to not affect the upstream conditions, guaranteeing atmospheric

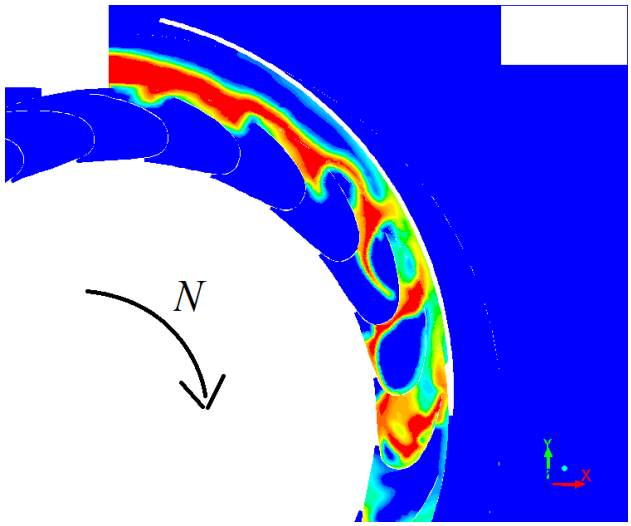

Fig. 4.22. Contour of volume fraction for the modified water wheel on the symmetry plane (normal to the rotation axis): red corresponds to only water present in the cells and blue to air. The transition between the two colors indicates the free surface.

pressure at the top of the wheel. Therefore, the inlet configuration (which, as explained, is intentionally not built for addressing all the flow rate into the first cell at the top of the wheel) is not improved. The wall is useful for re-addressing the water which is flowing outside of the wheel into the buckets, reducing the volumetric losses. In this way, the upstream conditions are not disturbed by the wall.

In Wahyudi et al. (2013) a different method has been experimentally tested to increase the torque of overshot wheels. The overflow of water from the buckets and the excess flow from the channel (volumetric losses at the top of the wheel) were converted into a water jet with high kinetic energy through a nozzle, and then squirt against the lowest blade. The efficiency increased from 61.6% to 73.5% (19% improvement). In the present work, the wall configuration is more efficient since water losses are converted into pressure, instead of velocity; it increases the efficiency of the wheel of more than 20%. As previously mentioned, considering that the wall can be done with a simple steel plate, the additional cost is negligible with respect to the total cost of the installation.

In conclusion, considering the complex phenomenon, the results are satisfactory to highlight the complex working behavior of overshot water wheels at high flow rates. The investigated modified design improves the wheel efficiency, thus it can be considered a viable option.

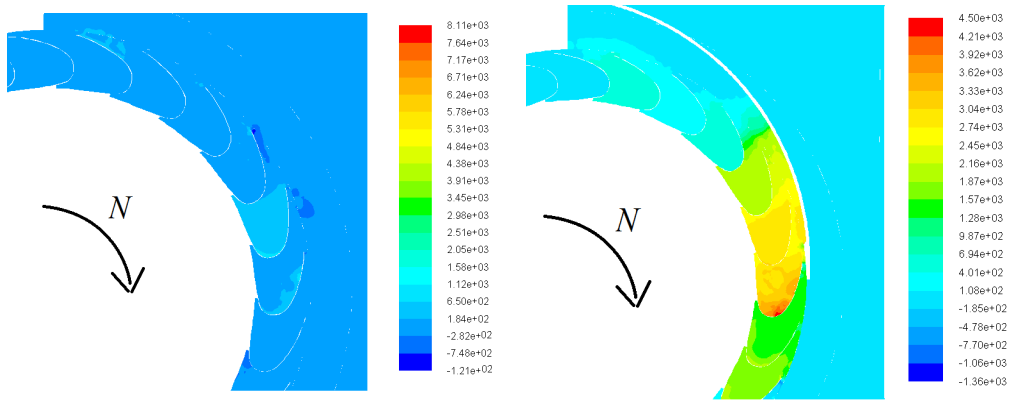

(a) *Original design* (b) *Improved design*

Fig. 4.23. Contour of static pressure [Pa] on the symmetry plane (normal to the rotation axis): the presence of the wall increases the static pressure.

4.5 General design suggestions

In order to design an overshot water wheel, once the flow rate and head are known, the diameter and width should be fixed. The diameter should be a little shorter than the vertical distance between the downstream free surface and the upstream channel bed, for instance 0.10 m on both sides (above and below). Then the maximum rotational speed can be determined using the results obtained in section 4.1.2. The number of the blades and their configuration (depth of the buckets) can be chosen using the historic literature. Once that the filling ratio is chosen (between 0.3 and 0.5), and the flow rate is known, the width of the wheel can be determined in order to satisfy that filling ratio. At this point the theoretical model can be applied to estimate the efficiency. Being the wheel now designed for its optimal configuration, it is not necessary to estimate the top volumetric losses. When the flow rate is slightly variable during the year, the water wheel could be designed considering the lowest flow rate and a width corresponding to a filling ratio of 0.3. In this way, the increase of the flow rate would lead to an increase in the filling ratio, that up to 0.5 remains still optimal. For higher values, the side wall here numerically investigated is suggested.

Chapter 5

Investigation of *Sagebien* and *Zuppinger* water wheels

In this chapter, the performance of a *Sagebien* wheel will be investigated and compared with the performance of a *Zuppinger* one, through experimental tests. Due to their different blades design, comparing the performance of these wheels allows to evaluate whether it is more important to minimize the inflow power losses (*Sagebien* wheel) or the outflow power losses (*Zuppinger* wheel). This is an important issue; indeed, it is often not practically possible to design a blade profile that minimizes both the inflow and the outflow power losses, because this would require a very large diameter. This work was performed at Southampton University (Quaranta and Müller, 2017).

In modern times, *Sagebien* wheels have not been investigated, whereas measurements at a full scale *Zuppinger* wheel demonstrate efficiencies of 72 to 75% (Neumayer et al. 1979) and up to 85% for a *Zuppinger* wheel of 1.8 m in diameter and head difference of 0.25 m (v. Harten et al. 2013). Furthermore, the most of the engineering information concerning with these wheels is reported in books dated to the Nineteenth century and the beginning of the Twentieth century (e.g. Sagebien, 1866; Garuffa, 1897; Müller, 1899; Busquet, 1906; Church, 1914). *Zuppinger* and *Sagebien* wheels have never been compared under the same hydraulic conditions. The historic information is often not clear and reliable; for example, concerning with the rotational speed, a maximum reference tangential speed is suggested, but this may be not satisfactory, since the rotational speed depends on several factors. It is also not clear the performance of the wheels at different flow rates. Hence there exists the need to determine with more accuracy their characteristic curves, thus the efficiency at different hydraulic conditions.

5.1 Experimental tests

5.1.1 Experimental setup

Physical models of a *Zuppinger* and *Sagebien* water wheel were built and investigated in the test channel of the Hydraulic laboratory at University of Southampton (UK). The wheels were conceived with a scale factor of 1:10 (using Froude similarity) of typical full scale wheels.

5.1.1.1 Experimental channel

The test channel was 12 m long, 0.30 m wide and 0.40 m deep (Fig.5.1). The flow rate (Q_{in}) was set by a pump and a bypass system; it was measured using the sharp crested weir at the outlet of the channel, which was 6.95 m downstream of the wheel. The weir allowed both the measurement of the flow rate and the regulation of the downstream water depth. The flow rate was estimated by:

$$Q_{in} = X b t \sqrt{2gt} \tag{5.1}$$

where $X = 0.402 + 0.054t/h_s$ is the weir coefficient, $B = 0.30$ m is the channel width, t is the water depth over the weir and $g = 9.81$ m/s^2 is the acceleration of gravity. In the coefficient X, h_s is the weir height. The water depth was measured 1.13 m upstream of the weir, by a point gauge with precision of $\pm 10^{-4}$ m. The upstream water depth (h_u) was measured 1.69 m before the centre of the wheel, while the downstream water depth (h_d) was measured 1.50 m downstream of the wheel; the precision was $\pm 10^{-3}$ m. Since the wheel was located over a plate 30 mm thick, the downstream water depth measured from the top of the plate was $h_{d,w} = h_d - 30$ mm.

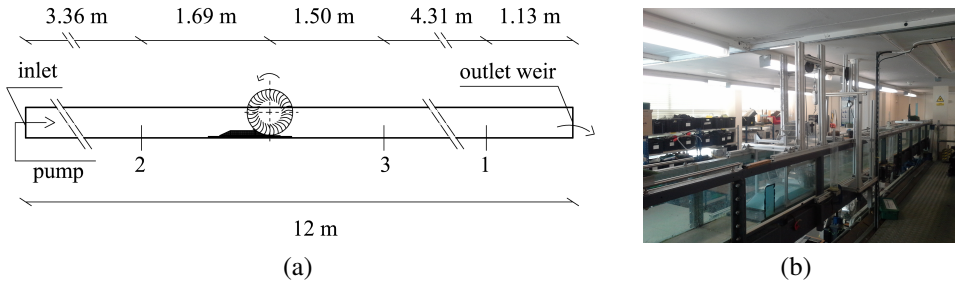

Fig. 5.1. The test channel. (a) The water depths were measured at 1 (for the weir), 2 and 3 (upstream and downstream water depth, respectively); (b) a picture of the Flume.

5.1.1.2 Experimental water wheels

Scale models of typical *Zuppinger* and *Sagebien* wheels were installed in the channel (Fig.5.2). Since the channel was wider than the wheels, the wheels were installed inside lateral shrouds, as depicted in Fig.5.3.

(a) (b)

Fig. 5.2. The *Sagebien* water wheel; (b) the *Zuppinger* water wheel.

The shrouds were made of a high density polystyrene foam ramp inside an acrylic housing. They were installed both to reduce the channel width upstream of the wheel (addressing the total inflow rate to the wheel) and to increase the bed elevation upstream of the wheel, creating a geometric head difference through the wheel of 65 mm. The *Zuppinger* wheel was firstly investigated. Its diameter is 600 mm and the width is 195 mm. It consists of 30 aluminium blades, 150 mm long, 180 mm width and 0.5 mm thick. The *Sagebien* wheel (Fig.5.4) is 600 mm in diameter and 195 mm in width. It consists in 30 aluminium straight blades, 150 mm long, 180 mm width and 1.5 mm thick. The blades were fastened to lateral acrylic Perspex disks (8 mm thick) of the wheel by screws. A sketch of the blades is depicted in Fig.5.5.

Because of the manufacture process of the side disks, the disks' surface was not perfectly smooth and flat, hence lateral gaps were needed to avoid friction between the disks of the wheel and the lateral walls of the shroud. A gap between the wheel and the curved section of the shroud below the wheel was also provided. Given that the wheel had a precise fit inside the shroud, care was taken so that the wheel did not come in contact (producing unwanted frictional forces) with the side walls, nor the shroud below it. Therefore, the wheel had to rotate freely, whilst minimizing the gaps. Since the wheels underwent small distortions during operation, and because of the not perfect alignment of the disks' surface, it was not possible to reduce the gaps under a certain value. The gaps were 6 mm below the wheel and 4 mm between the wheel and the lateral walls. This configuration

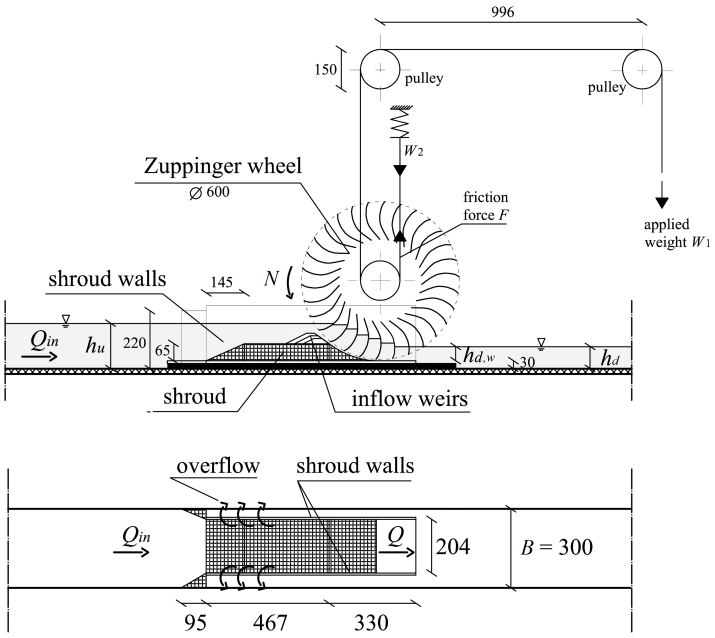

Fig. 5.3. Lateral and plan 2D views of the channel, the Prony brake and the *Zuppinger* wheel (in millimetres). The water depth must be $h_u \leq 220$ mm to avoid volumetric losses. The lateral gaps were different on each side.

generated leakage losses, whose estimation is reported in the next section. At full scale, such gaps would be 40 to 60 mm, so that the gap width at model scale is disproportionally large. Therefore, in order to eliminate this scale effect in the results, the leakages will be subtracted from the total flow rate, and only the flow rate effectively passing through the wheel will be considered in the calculation of the efficiency. Then, the when applying the results here presented to a full scale model, the full scale efficiency can be estimated subtracting to the experimental efficiency here reported the effect of the full scale leakages, estimating them using the same method here used.

5.1.1.3 Power output estimation

A Prony brake was installed to regulate the wheel velocity (N). Figure 5.3 depicts the *Zuppinger* wheel and the Prony brake. The Prony Brake uses a stationary friction belt around the surface of a pulley, which is fastened at the shaft of the wheel (on the right side of the wheel in this case). A weight W_1 attached to this belt applies tension to it, creating a friction force F along the profile of the pulley. This causes a braking force on the wheel. When the wheel rotates, the weight

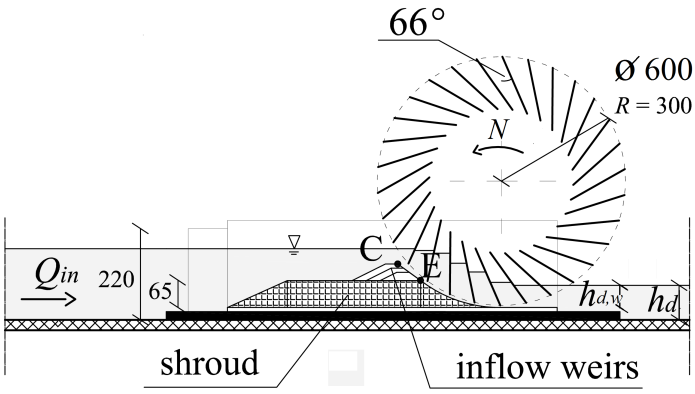

Fig. 5.4. The *Sagebien* water wheel installed in the channel. The inflow weirs were installed on the shroud upstream of the wheel for a second series of tests.

W_2 transmitted through the belt to the 'counterweight' (which takes the form of a securely fixed digital scale) is reduced by the friction force F exerted along the pulley. The braking force F can be calculated by the difference between the applied weight W_1 and the weight W_2 read on the scale (the weight is the mass multiplied by the gravity acceleration, and the mass M was read with a precision of ± 0.01 kg). Since the pulley is fastened to the wheel, the friction force times the pulley radius r ($r = 0.075$ m) is equal to the braking torque (C) applied to the wheel, which in stationary conditions must be equal to the torque generated by the wheel. The wheel velocity was measured by a stopwatch with precision of 0.01 s. The time for 10 revolutions was monitored; three measurements were made, and the mean value was used for the calculations. Then, the power output was obtained by the torque C (Nm) and rotational speed N (rad/s):

$$P_{exp} = CN = r(M_1 - M_2)gN \tag{5.2}$$

5.1.1.4 Leakage estimation

Considering that the tested wheels are 1:10 scaled models of typical ones, the 4 mm and 6 mm gaps correspond to 40 mm and 60 mm, respectively, in the full scale models. Considering that maximum gaps in real cases generally are 10÷20 mm, such gap values are not common. This means that larger leakage losses occur in the model with respect to the full scale wheels.

The flow through the gap is an integral part of the losses inherent in a water wheel installation, and the gap width is a compromise between the necessity to reduce losses, and the requirement to avoid jamming of the wheel through e.g.

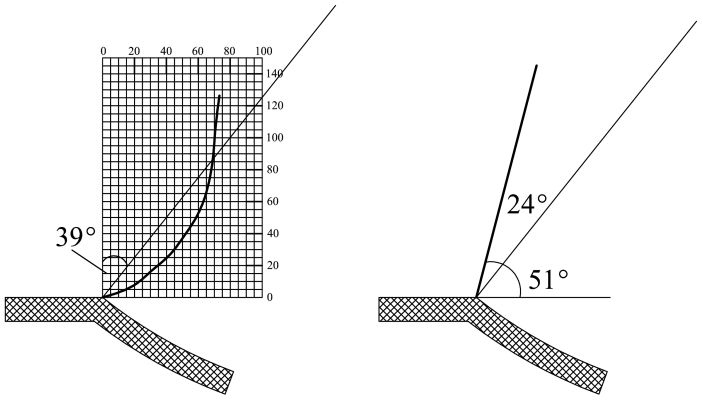

Fig. 5.5. The blade shape (units in mm) of the *Zuppinger* (left) and *Sagebien* (right) water wheel (the blade is the thick line). The blades of *Sagebien* wheels are straight blades. The continuous thin line is the radial direction.

floating branches which can get stuck between blades and the concrete walls of the channel. Considering a scale of approximately 1:10; this would mean that gap widths of 1 mm were required. The scaling of gaps width has two aspects:

1. The flow resistance of the gap, i.e. Reynolds similarity. For turbulent flow, $Re > 2000$ is needed. The gaps width in the model ensure $Re > 2000$.

2. Construction requirements at model scale.

Assuming a typical head difference of 0.9 m, and five immersed blades, hence a gap flow velocity of 1.8 m/s, the Reynolds number for the gap flow at full scale (gap width of 1 cm) can be determined as $Re = 19,000$. An exactly scaled down geometry would result in $Re = 600$ for the gap flow (gap width of 1 mm), and therefore would lead to lower gap losses than at full scale (because of laminar flow). The material used for the construction of the wheel, as well as distortion of the runner caused by the application of high torque and normal forces on the shaft, meant that the model had gap widths of 4 mm on the sides and 6 mm at the bottom This implied that, although flow conditions around the blade were modeled accurately ($Re > 2000$, turbulent flow as at full scale), the flow volume through the gaps was significantly larger than at full scale. The model therefore suffers from scale effects which have to be compensated to obtain realistic performance predictions. Therefore, in the analysis of the results, it is preferable to eliminate the flow leakage and to consider the effective discharge. This ensures that the experimental results have a general significance, because the leakages are closely related to the specific hydraulic system in which the wheel is tested. For the purpose of this investigation, the leakage flow Q_{gaps} in the model scale was determined by

eq. 5.3:

$$Q_{gaps} = Q_f + Q_l + Q_u \tag{5.3}$$

where, using the same terminology of section 4.2.2.3: Q_f is the leakage through the horizontal gap, that can be estimated by eq.3.29 as was done for breastshot wheels. The difference between the free surface upstream-downstream is $h_u - h_d$, since the slope of the channel is zero. For the sake of simplicity, it is possible to assume that the water depth in each bucket is the same, so that the head difference through each blade is the same. Q_l can be assumed zero, since from the experiments it could be observed that the water level difference between the flow through the lateral gap and that of the buckets was almost zero. Q_u was the leakage through the lateral vertical gaps at the inlet of the wheel, estimated assuming the same flow velocity of the approaching flow rate (since the downstream water depth was not in touch with the upstream one), and considering the geometry of the gaps. The leakages so estimated ranged between 0.4 to 0.8 l/s.

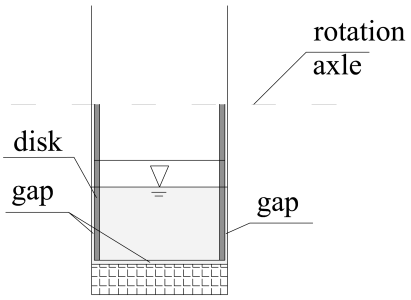

Fig. 5.6. View of the blades at the inlet (the dimensions of the gaps are not realistic to make them more visible).

5.1.1.5 Efficiency estimation

In order to determine the efficiency of the wheel, the power input of the wheel was evaluated by measuring the upstream depth h_u and the downstream depth h_d; the available head, or head difference, H_{gr} (i.e. the difference between the energy head upstream and downstream of the wheel) was obtained as:

$$H_{gr} = \left[\left(h_u + \frac{{v_u}^2}{2g}\right) - \left(h_d + \frac{{v_d}^2}{2g}\right)\right] \tag{5.4}$$

where v_u is the mean upstream velocity of the flow and v_s is the mean downstream velocity of the flow (the slope of the channel bed was zero).

The power input to the wheel can be then expressed by:

$$P_{gr} = \rho g(Q_{in} - Q_{gaps})H_{gr} \tag{5.5}$$

and the efficiency of the wheel is defined as:

$$\eta = \frac{P_{exp}}{P_{gr}} \tag{5.6}$$

Using the net flow rate to the wheel, higher efficiency values are expected, since leakages are not considered. Therefore, the efficiency for a real application should be then calculated as $\eta_f = \eta - Q_{gaps,f}/Q_{in,f}$, where with the suffix f we refer to the values in the full scale model.

5.1.1.6 Experimental procedure and investigated conditions

The aim of the first set of experiments was to investigate the performance of the wheels in their traditional configuration without inflow control. The investigated flow rates ranged approximately between $Q = 2 \div 7$ l/s (five flow rate cases for the $Zuppinger$ wheel and four cases for the $Sagebien$ wheel), wheel rotational speeds approximately between $N = 5 \div 45$ rpm, upstream water depths between $h_u = 130 \div 210$ mm (the upstream depth depended on the flow rate) and downstream water depths between $h_d = 20 \div 80$ mm (four cases).

The test procedure was: the flow rate was firstly set with the pump of the supply pipe, and then the downstream water depth was regulated acting on the height of the downstream weir. Different wheel velocities were then investigated, acting on the Prony brake. Since the upstream water depth depended on the flow rate, the maximum investigated flow rate took into account the maximum limit of the upstream depth, since for $h_u > 220$ mm water overflows from the lateral acrylic walls of the shroud. The minimum flow rates took in consideration the real operative conditions; at very low flow rates, the wheel rotation did not occur and the leakages were comparable with the total inflow rate. The downstream depth was regulated by the outlet weir, considering the real operative conditions of these water wheels. The maximum investigated wheel velocity was the run-away velocity (found as 45 rpm maximum, occurring at the highest flow rate and hydraulic head); in these cases the braking torque was not applied to the wheel. The minimum wheel velocity was instead chosen considering different aspects:

(1) the conditions tolerable by the brake system;

(2) a free and uniform wheel rotation had to be ensured;

(3) the maximum tolerable upstream water depth. At $N < 9 \div 11$ rpm for the *Zuppinger* wheel and $N < 11 \div 13$ rpm for the *Sagebien* wheel, the upstream water depth progressively increased. Therefore, the minimum wheel rotational speed was between $5 \div 8$ rpm for the *Zuppinger* wheel and between $5 \div 10$ rpm for the *Sagebien* wheel, depending on the flow rate.

(4) the realization of the maximum efficiency for each hydraulic condition (flow rate and downstream water depth), since when the rotational speed became slower than a certain value, the efficiency started to decrease;

5.1.1.7 Operative conditions: tests with the inflow weirs

A second series of tests was performed; the wheels were tested with an inflow weir on the shroud upstream of the wheel, as depicted in Fig.5.4. These tests were carried out to investigate whether the wheels are able to work at a constant upstream water depth and flow rates which progressively reduce. This method can represent a possible solution to maintain a constant rotational speed, which should be preferred to the variable speed operation (e.g. Müller and Kauppert, 2004). Normally, when the flow rate reduces, the upstream water depth also reduces. In order to ensure always the same upstream depth, an inflow weir is hence necessary, whose height has to be increased as the flow rate reduces, increasing the water entry point to the wheel, thus the potential energy of the flow. On the basis on the practical operative conditions of *Zuppinger* and *Sagebien* water wheels, the upstream water depth was fixed at $h_u = 150$ mm, and the downstream water levels at $h_d = 80$ mm. The downstream water depth was then lowered to $h_d = 50$ mm, in order to evaluate the consequences of the downstream water depth on the performance of the wheel in these conditions. The investigated trapezoidal inflow weirs were 20-30-40 mm high. Because of the trapezoidal shape, the downstream side (the side in front of the wheel) EC (Fig.5.4) of the inflow weir is not circular, but straight. Although it is inclined as the local inclination of the shroud in E, the gap between the weir and the blades increases from the lowest edge E to the highest edge C of the inflow weir, generating higher leakage losses than in standard operative conditions.

5.1.2 Results

In this section we will briefly discuss the results in their original form (dimensional terms). In order to generalize them, they will be detailed discussed in the following sections using dimensionless terms. The efficiency will be described as a function of the normalized wheel rotational speed, normalized flow rate and

normalized head difference.

Figures 5.7 and 5.8 show the power output versus the rotational speed for two representative cases. The power output reduces with increasing wheel speed. When the wheel rotates freely, without any brake, the power output is zero. The downstream water depth affects the power output especially at high wheel velocities ($N > 20$ rpm, 6.3 rpm in the full scale model). The effect of the downstream depth is less important in the *Zuppinger* wheel, thanks to the blades shape, intentionally conceived to minimize the outflow power losses. The head difference was regulated acting on the downstream weir: the higher the height of the weir, the higher the downstream water depth, thus the lower the head difference. The increase in the downstream water depth increases the adverse hydrostatic force exerted by the tailrace to the blades, reducing the wheel speed and the power output. It is also possible to observe that when the downstream depth was higher than approximately 0.09 m, the power output was significantly and badly affected.

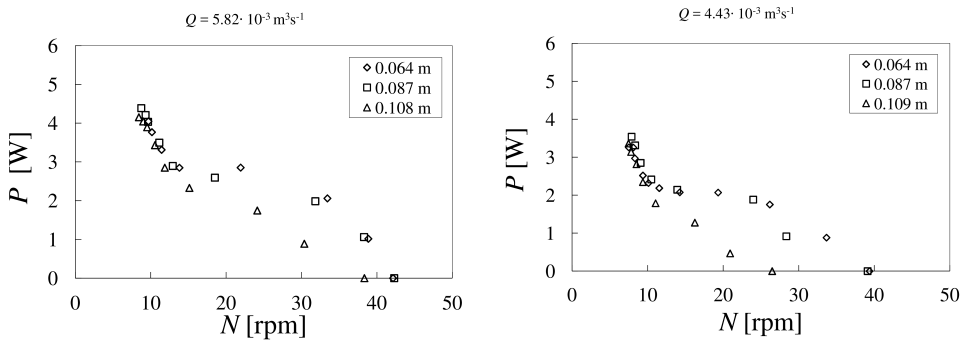

Fig. 5.7. Power output versus the wheel rotational speed at different downstream water depths $h_{d,w}$, for the *Zuppinger* wheel. Two representative flow rate cases are illustrated.

Leakage losses were estimated and subtracted from the total inflow, thus the actual flow rate through the wheel was calculated. The leakage losses ranged between $0.4 - 0.8$ l/s. A series of tests was performed with the wheel fixed and at different flow rates and downstream water depth; since the wheel was at rest, all the flow rate which passed through the wheel was leakage. In this way, investigating similar water depths (upstream and downstream of the wheel) with respect to the operative conditions with the moving wheel, it was possible to validate approximately the leakages estimation. The leakage during the static tests ranged between $0.5 - 1$ l/s. At this point it was possible to estimate the wheel efficiency.

Tables 5.1 and 5.2 show the summary of the results in the highest efficiency configurations. For each actual flow rate and downstream water depth, the maximum efficiency η_{max} occurs at the optimal rotational speed N_{opt}. The maximum

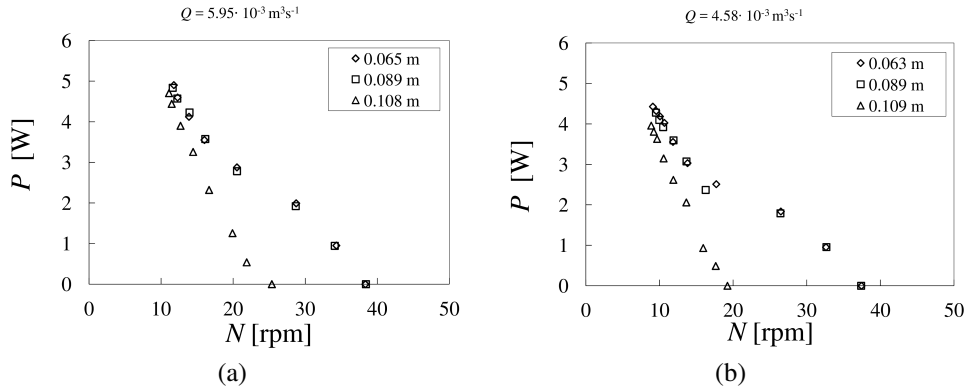

Fig. 5.8. Power output versus the wheel rotational speed at different downstream water depths $h_{d,w}$, for the *Sagebien* wheel. Two representative flow rate cases are illustrated.

efficiency of the *Sagebien* wheel ranges between 63÷88%, while the *Zuppinger* wheel efficiency ranges between 54÷88%. These values are reasonable, since they do not include leakages, that should be considered in the real case, as explained in section 5.1.1.5. The efficiency is a function of the wheel velocity, and the maximum efficiency is a function of the head difference and flow rate. The optimal wheel speed increases with the flow rate. The optimal speeds for the *Zuppinger* wheel are included between $6.5 \div 15.1$ rpm for $2.0 < Q < 5.9$ l/s (excluding the highest flow rate cases, that are too high), while for the *Sagebien* wheel the optimal speed range is $5.9 \div 14.0$ rpm for $2.1 < Q < 5.9$ l/s. The filling ratio (which is the ratio of the water volume in the bucket to the bucket volume, deducible from the geometric design of the wheel) at the optimal efficiency is between 39% to 87% for the *Zuppinger* wheel (excluding the lowest value of the filling ratio among all the filling ratio values) and 41% to 88% for the *Sagebien* wheel.

These results are in agreement with those found in literature. The maximum efficiency of *Zuppinger* wheels was identified in 85% (v. Harten et al., 2013), and the blades number could be reduced from the recommended 50 to 30 without a performance penalty. Concerning *Sagebien* wheels, to the best of our knowledge no experimental tests have been performed in detail. Anyway, the efficiencies were estimated as 80 to 93% (Sagebien, 1866), in agreement with the results achieved in the present work.

The optimal speeds for the *Zuppinger* wheel are 6.5÷15.1 rpm, and for the *Sagebien* wheel they are included between 5.6÷14.0 rpm. For the *Sagebien* wheel, these velocities correspond to tangential velocities between 0.18÷0.44 m/s, hence 0.56÷1.4 m/s in the 10:1 full scale model (2.0÷5.0 rpm), which is faster than what was proposed in literature (0.6÷0.8 m/s). For the *Zuppinger* wheel, 6.5÷15.1

Table 5.1. Operative conditions (corrected flow rate estimated subtracting from the total flow rate the estimated leakages, upstream and downstream water depth, head difference), maximum efficiency, optimal speed, fill ratio and power output at maximum efficiency for the *Zuppinger* wheel.

Q [l/s]	h_u [m]	h_d [m]	H_{gr} [m]	η_{max} [%]	N_{opt} [rpm]	Fill.ratio	P_{exp} [W]
2.0	0.127	0.039	0.086	55	6.50	0.50	0.93
2.1	0.126	0.060	0.065	60	8.66	0.39	0.80
3.0	0.155	0.044	0.108	56	6.66	0.71	1.77
3.0	0.136	0.065	0.070	68	8.71	0.56	1.40
3.1	0.140	0.086	0.053	82	7.76	0.63	1.32
3.1	0.156	0.107	0.049	85	6.43	0.77	1.25
4.4	0.185	0.064	0.118	65	8.11	0.87	3.25
4.4	0.159	0.087	0.070	79	10.48	0.69	2.41
4.5	0.170	0.109	0.060	88	9.36	0.77	2.34
5.9	0.179	0.064	0.109	53	11.44	0.83	3.31
5.7	0.184	0.087	0.094	67	11.13	0.82	3.50
5.9	0.162	0.108	0.053	76	15.12	0.63	2.33
7.5	0.179	0.084	0.089	61	16.00	0.76	4.02
7.5	0.202	0.107	0.093	65	12.52	0.96	4.44

rpm correspond to 0.7÷1.5 m/s in the full scale model, thus rotational speeds of 2.2÷4.8 rpm, which is slower than what has been proposed in literature.

5.1.2.1 Efficiency versus normalized wheel velocity

Figures 5.9 and 5.10 depict the efficiency of the wheels versus the normalized rotational speed. The wheel speed was normalized in order to make the different tests comparable. The normalized velocity u^* is the ratio of the tangential wheel velocity u to the term $\sqrt{2gH_{gr}}$, as also done for the investigated breastshot water wheel. The runaway velocity was the highest investigated wheel velocity, to which corresponds a normalized velocity of approximately 1. The efficiency initially increases with the increase in the wheel rotational speed. The efficiency reaches a maximum (η_{max}), which is higher as the downstream water depth increases, and then the efficiency decreases. At the runaway velocity the power output and efficiency is zero. However, when the downstream depth $h_{d,w}$ is lower than 0.035 m, the maximum efficiency remains constant over a wider range of rotational speeds, which is between $10 \div 15$ rpm. Hence the downstream water depth affects both the wheel velocity and the efficiency; the higher the water depth the lower

Table 5.2. Operative conditions (corrected flow rate estimated subtracting from the total flow rate the estimated leakages, upstream and downstream water depth, head difference), maximum efficiency, optimal speed, fill ratio and power output at maximum efficiency for the *Sagebien* wheel.

Q [l/s]	h_u [m]	h_d [m]	H_{gr} [m]	η_{max} [%]	N_{opt} [rpm]	Fill.ratio	P_{exp} [W]
2.09	0.160	0.048	0.087	67	9.11	0.41	1.21
2.10	0.151	0.065	0.084	78	6.47	0.57	1.35
2.13	0.160	0.088	0.072	87	5.88	0.64	1.30
2.16	0.170	0.110	0.061	75	4.59	0.83	0.97
3.36	0.189	0.048	0.137	67	8.02	0.74	3.01
3.45	0.156	0.065	0.088	73	11.10	0.55	2.17
3.47	0.168	0.085	0.082	83	9.46	0.65	2.33
3.42	0.195	0.107	0.087	80	7.03	0.86	2.36
4.53	0.193	0.052	0.133	68	10.50	0.76	4.00
4.55	0.192	0.063	0.125	72	10.66	0.75	4.03
4.62	0.181	0.089	0.091	88	11.90	0.68	3.59
4.61	0.205	0.109	0.094	85	9.67	0.84	3.63
5.89	0.203	0.065	0.133	64	11.76	0.88	4.90
5.97	0.185	0.089	0.094	77	13.94	0.76	4.23
5.99	0.194	0.108	0.085	78	12.69	0.83	3.90

the rotational speed, because of the higher adverse hydrostatic force generated by the tailrace on the blades. This result can be immediately deducted observing that the value of the runaway velocity reduces as the downstream depth increases. The optimum normalized velocities u^* are included in the range between 0.1 to 0.35. They increase with the flow rate, since the higher the flow rate, the higher the approaching flow velocity. This is valid for both the wheels (Fig.5.11).

V. Harten et al. (2013) tested a wheel of 1.8 m diameter, with a maximum efficiency of 85% at 7.6 rpm and a head difference of 0.25 m; the normalized velocity is $u^* = 0.32$, which corresponds well to our results. Our results also well correspond with the normalized velocities found for the breastshot water wheel and investigated in section 3.1.2.3 ($u^* = 0.2 \div 0.4$).

5.1.2.2 Maximum efficiency versus head difference and flow rate

The efficiency was also investigated as a function of head difference and flow rate. In order to make the results generically applicable, it was decided to normalize the energy head to the wheel's diameter and the flow rate to the optimal flow

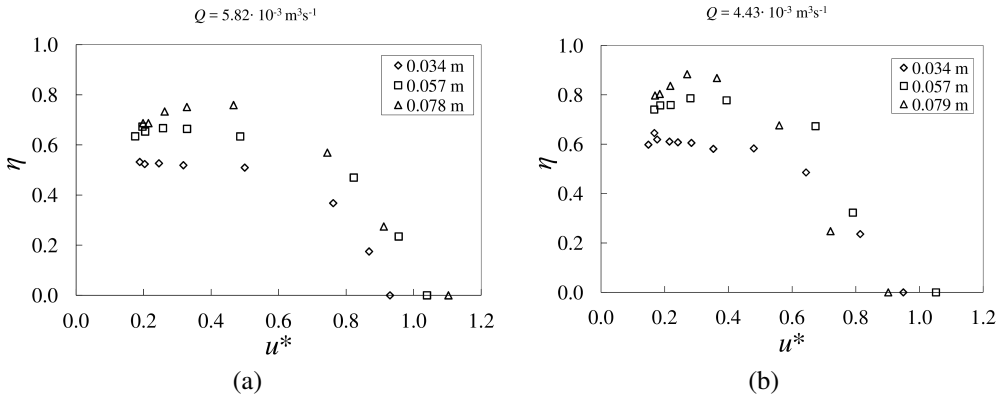

Fig. 5.9. Efficiency versus the normalized wheel speed at different downstream water depths $h_{d,w}$, for the *Zuppinger* wheel. Two representative flow rate cases are illustrated.

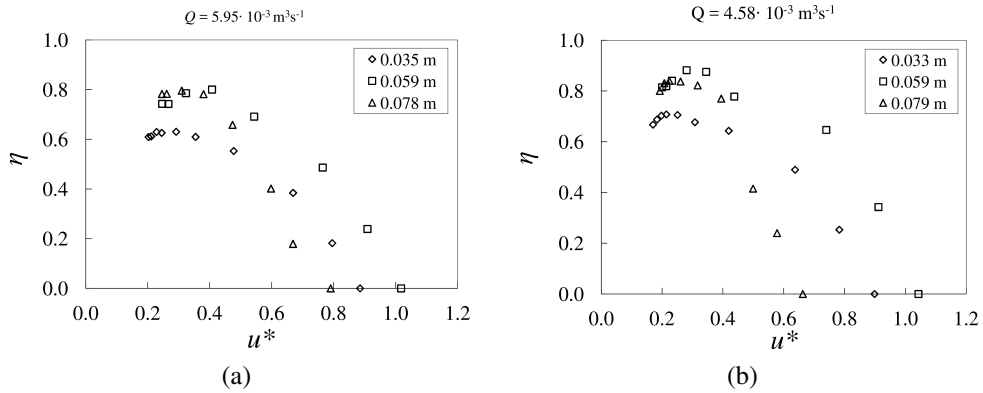

Fig. 5.10. Efficiency versus the normalized wheel speed at different downstream water depths $h_{d,w}$, for the *Sagebien* wheel. Two representative flow rate cases are illustrated.

rate. Figure 5.12 shows that the maximum efficiency decreases with the increase in the head difference, thus with the decrease in the downstream water depth. This particular decreasing trend occurs because the head difference appears at the denominator of the definition of efficiency. Therefore, although the power output decreases with the increase in the downstream water depth (reduction in the head difference), the global efficiency improves.

Figure 5.13 shows the maximum efficiency versus the normalized flow rate, where Q_{max} is the flow rate at maximum efficiency for each downstream water depth (the downstream water depth depends on the downstream geometric conditions in addition to the flow rate). The efficiency of the *Sagebien* wheel slightly reduce with the flow rate, whereas the efficiency of the *Zuppinger* wheel slightly decreases. The optimal flow rates are 3.02, 3.06, 4.49 l/s at $h_{d,w} =$

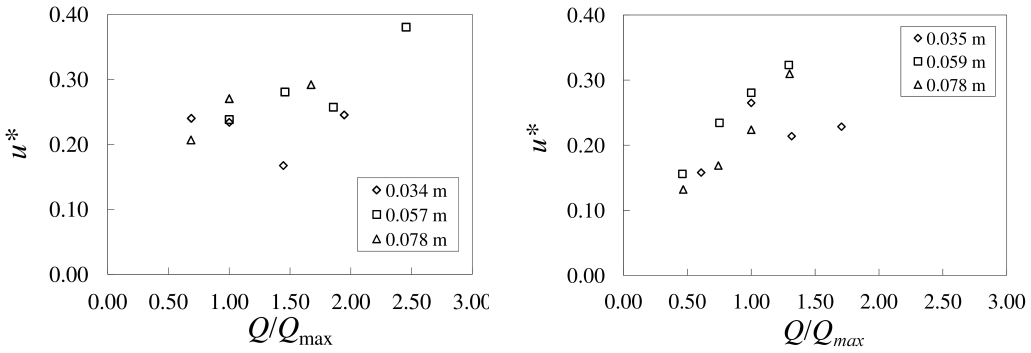

(a) *Zuppinger* (b) *Sagebien*

Fig. 5.11. Optimal normalized rotational velocities versus the normalized flow rate at different downstream water depths $h_{d,w}$, for the *Zuppinger* (a) and *Sagebien* wheel (b).

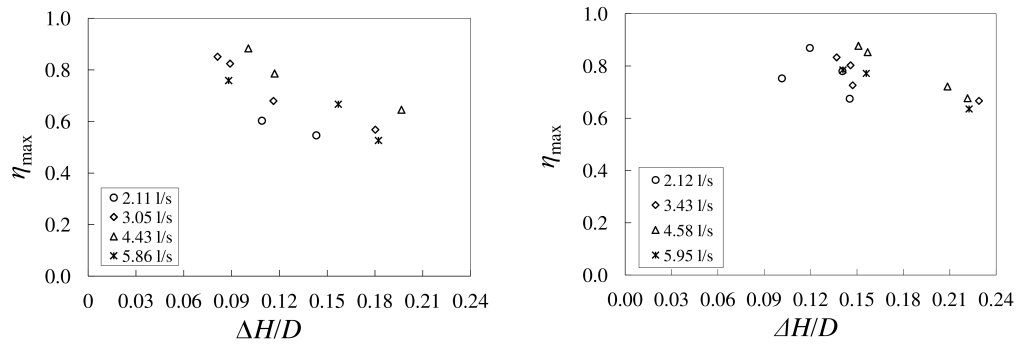

(a) *Zuppinger* (b) *Sagebien*

Fig. 5.12. Efficiency versus the normalized head difference at different flow rates, for the *Zuppinger* (a) and *Sagebien* (b) wheel.

$0.034, 0.057, 0.078$ m, respectively, for the *Zuppinger* wheel. For the *Sagebien* wheel the optimal flow rates are 3.45, 4.62, 4.61 l/s at $h_{d,w} = 0.035, 0.059, 0.078$ m, respectively. The optimal flow rates for the *Zuppinger* wheel are lower than the optimal flow rates for the *Sagebien* wheel, hence *Sagebien* wheels can exploit larger flow volumes at higher efficiencies. This result is confirmed comparing the filling ratio of the buckets; it corresponds to 39%÷87% for the *Zuppinger* wheel and 41% to 88% for the *Sagebien* wheel in the optimal efficiency cases. The previous results show that *Sagebien* water wheels are more convenient for a practical use, since their efficiency is less affected by the external hydraulic conditions. Anyway, the *Zuppinger* wheel exhibits an efficiency which has a wider plateau versus the rotational speed. Therefore, although the *Sagebien* wheel can be used over a wide range of operative conditions (at a variable speed of operation), the

choice of its rotational speed is a very crucial point. Hence, when the external conditions remain constant (flow rate and water depths) it would be better to use the *Zuppinger* wheel, whose optimal rotational speed estimation is easier.

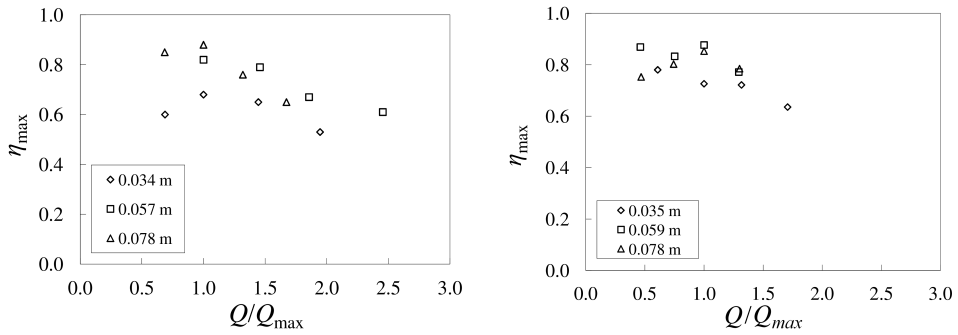

(a) *Zuppinger* (b) *Sagebien*

Fig. 5.13. Efficiency versus the normalized flow rate (Q_{max} is the flow rate at maximum efficiency for each curve) at different downstream depths $h_{d,w}$; (a) *Zuppinger* wheel; (b) *Sagebien* wheel.

For the *Sagebien* wheel the optimal flow rates range between 3.5 to 4.6 l/s. For the *Zuppinger* wheel the optimal flow rates range approximately between 3 to 4.5 l/s. The results are in agreement with the historic literature, since the total flow rates scaled to the full scale model correspond to 1.1 and 1.45 m^3/s for the *Sagebien* wheel. For the full scale *Zuppinger* wheel, the identified flow rates correspond to 0.96 and 1.42 m^3/s. Considering that the full scale width is 1.8 m, the previous results correspond to a maximum flow rate of about 0.8 m^3/s per meter width. The optimal flow rates at a fixed downstream water depth are generally higher in the *Sagebien* wheel than in the *Zuppinger* wheel, thus *Sagebien* wheels can exploit larger water volumes.

As explained in the Introduction, the mean difference between the investigated wheels is the shape of the blades, that in *Sagebien* wheels is optimized for the inflow conditions, and in *Zuppinger* wheel for the outflow conditions. As a consequence, as it was observed during the experimentation, the *Zuppinger* wheel may generate a slam effect and noise at the inlet, since the surface of the blade that is entering into the upstream water is practically parallel to the upstream water surface. Instead, the *Sagebien* water wheel may lift water on the downstream side.

5.1.2.3 Performance with the inflow weirs

Zuppinger wheels and some *Sagebien* wheels have inflow weirs to regulate the upstream water level, in order to provide good efficiency at a constant speed operation. Scope of this section is to analyze the performance of the wheels equipped with inflow weirs just upstream of them. Different flow rates were investigated, ensuring a constant upstream water depth. In order to ensure always the same upstream depth, the height of the weir has to be higher as the flow rate reduces. This allows to explore the wheel behavior at very low flow rates. On the basis on the practical operative conditions for *Zuppinger* and *Sagebien* water wheels, the upstream water depth was maintained at $h_u = 150$ mm and the downstream water depth at $h_{d,w} = 60$ mm. Trapezoidal inflow weirs of 20 - 30 - 40 mm were investigated (one at time), with total flow rates ranging between $Q = 0.6 \div 3.7$ l/s. The downstream depth was then lowered to $h_{d,w} = 20$ mm. The downstream depth of 20 mm corresponds to a water level which is not able to exert a significant adverse hydrostatic force from the tailrace to the wheel.

The efficiency trend of the *Sagebien* water wheel (Fig.5.14b) reaches a maximum for each different inflow configuration, except for the highest inflow weir (40 mm). With the inflow weir of 20 mm, the optimal conditions are included between 5÷10 rpm (1.58÷3.16 rpm in the full scale model), i.e. normalized velocity of 0.13÷0.3, with efficiencies of 67%÷80%. For the inflow weir of 30 mm the maximum efficiency is 70% at 3.69 rpm (1.2 rpm at the full scale model), which immediately decreases after the maximum. When $h_{d,w} = 60$ mm, the *Zuppinger* wheel cannot reach a maximum efficiency both with the weir of 40 and 30 mm (Fig.5.14a), hence only inflow weirs lower than 30 mm are advisable. The optimal conditions for the weir of 20 mm are between 3.8÷8 rpm (1.2÷2.5 rpm in the full scale model), i.e. normalized velocity between 0.1÷0.24, and efficiencies between 70÷80%. The maximum height of the inflow weir was identified in 48.8% of the water depth just upstream of it (the water depth on the shroud) for the *Sagebien* wheel and 33.4% for the *Zuppinger* wheel. These tests show that it is possible to use inflow weirs up to 1:10 with respect to the wheel radius in *Sagebien* wheels, while in *Zuppinger* wheel only up to 1:15.

When the downstream depth is lowered to 20 mm, the optimal conditions of the *Sagebien* wheel are represented by a constant efficiency of approximately 60% in the range of 5÷12.5 rpm (1.58÷3.95 rpm in the full scale model) for inflow weirs lower than 30 mm (with the weir of 30 mm the maximum efficiency is 60%, but rapidly it decreases), while for the *Zuppinger* wheel the optimal conditions are in the range of 5÷15 rpm (1.58÷4.74 rpm in the full scale model) for inflow weirs lower than 30 mm, with efficiencies between 56% and 64%.

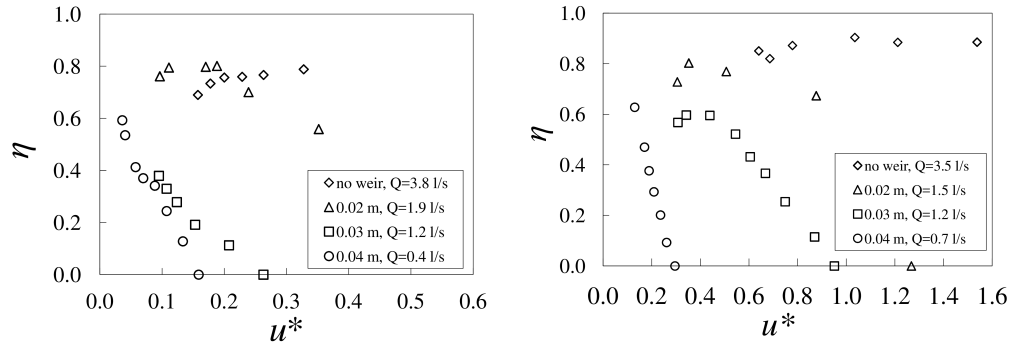

(a) *Zuppinger* (b) *Sagebien*

Fig. 5.14. Efficiency versus the normalized wheel rotational speed for different inflow weirs for the *Zuppinger* (a) and *Sagebien* (b) wheel. The results are relative to the downstream water depth of $h_{d,w} = 0.06$ m.

Concluding, although both *Sagebien* and *Zuppinger* wheels can be considered efficient hydropower converters at very low heads, *Sagebien* wheels are better than *Zuppinger* ones. The maximum efficiency of the *Sagebien* wheel is constant over a wider range of flow rates and head differences, while the performance of the *Zuppinger* wheel decreases more significantly with the head difference and flow rate. Hence the optimization of the inflow conditions is more important than the optimization of the outflow conditions. The wheels can also be employed at a constant speed operation, by a control of the inflow, as long as the weir height is lower than the maximum recommended height. Practical suggestions were also reported to guide engineers in the design of these water wheels.

Conclusions

The aim of the present thesis was the investigation, estimation and improvement of the performance of gravity water wheels.

The investigation of the performance was achieved through experimental tests on scale models of breastshot, overshot and undershot water wheels. The results of the experimentation, supported by the results found in literature, show that the maximum efficiencies are included between 80÷90% for overshot and undershot, and 70÷ 85% for breastshot water wheels. These values are comparable with other micro hydropower converters, such as *Kaplan* turbines and Archimedes screws. Furthermore, the efficiency remains optimal over a wide range of flow rates. Since the investigated breastshot and overshot wheels are 2 m and 1.4 m in diameter, respectively, thus they do not suffer of particularly scale effects, the results here found can be considered reliable also for practical cases and different installations. Instead, for the undershot wheels, as already discussed, the efficiency has to take into account volumetric losses of the full scale model.

The rotational speed affects the performance. Considering the breastshot wheel, the rotational speed is important especially when the approaching flow velocity is not negligible, as in the case of the breastshot water wheel equipped with a sluice gate inflow. For the overshot wheel, a maximum limit for the rotational speed can be identified; when this limit is exceeded, the efficiency begins to rapidly decrease, as a consequence of the volumetric losses at the top of the wheel. For undershot wheels, the rotational speed is a significant parameter, since the inflow and outflow power losses depend on it.

The theoretical models are accurate enough to predict the performance of water wheels, and they can be used also for engineering applications. In particular, the theoretical model for the breastshot water wheel has highlighted that the upstream conditions are more important than the downstream ones when an optimization process has to be considered. This result was also confirmed by the experimental tests on undershot water wheels, since the *Sagebien* wheel performs better than the *Zuppinger* one (*Sagebien* wheels are optimized to reduce the in-

flow power losses, thus they are optimized considering the upstream conditions). Therefore, the design of the blades can contribute to improve the efficiency of breastshot wheels.

The estimated impact coefficient for breastshot wheels can be considered reliable in water wheels whose blades are oriented parallel to the relative flow velocity in the impact point, and when the water flow enters into the wheel substantially under the axle. The quantification of impact losses by the presented theoretical model may not be valid if the water entry point is close to the wheel axle. In this case, although the blades could be well designed, the moment arm of the impact force would approach zero, and the generated impact force could be used to compress the wheel onto the shaft, instead of generating torque. However, water wheels better exploit the potential energy of water.

Concerning with the overshot water wheel, the theoretical model has revealed that the volumetric losses at the top of the wheel becomes determinant at high rotational speeds, generally needed at high flow rates; therefore, an optimization process should aim to reduce them, as it was done by the CFD model. The estimation of the top volumetric losses using the theoretical model is relative to the investigated water wheel and for its blades shapes. It is not reliable for being applied in other geometric configurations. However, water wheels should operate in their optimal performance range, when such volumetric losses are negligible. Hence, the most important results found for the overshot wheel was the identification of the maximum rotational speed, after that the volumetric losses start.

Dimensional approaches were also adopted to obtain speditive equations to estimate the maximum power output and efficiency achievable by similar overshot and breastshot wheels.

Following the previous results, numerical simulations were performed to optimize the performance of breastshot and overshot water wheels, acting on the blades design and on the geometry at high flow rates, respectively. In this way, it has been possible to improve the efficiency of water wheels, showing that CFD tools are adequate to simulate the hydraulic behavior of these hydropower converters. In particular, it is possible to recommend, for fast breastshot wheels, a distance between two blades shorter than 2.5 times the water depth just upstream of the wheel. Instead, concerning with the blade shape, some restrictions and suggestions were discussed in this thesis. A circular profile is recommended since its manufacturing process can be easily automated and realized, and indications on the optimal curvature radius were discussed.

Therefore, the objectives of this thesis have been achieved. Future works will aim to investigate with more details the improved design of the overshot water

wheel, for example investigating a wider range of flow rates.

Concluding, water wheels can be considered suitable micro hydropower converters, since they are efficient, simpler and cheaper to be installed than other turbines. However, their design must not be under evaluated: water wheels must be accurately designed, because an optimal design can be identified.

References

Akinyemi, O. S., and Liu, Y. (2015a). "CFD modeling and simulation of a hydropower system in generating clean electricity from water flow". *International Journal of Energy and Environmental Engineering, 1-10*.

Akinyemi, O. S., and Liu, Y. (2015b). "Evaluation of the power generation capacity of hydrokinetic generator device using computational analysis and hydrodynamics similitude". *Journal of Power and Energy Engineering, 3(8), 2015, 71-82*.

Bach, C. (1886). *Die Wasserräder: Atlas (The water wheels: technical drawings)*. Published by Konrad Wittwer Verlag, Stuttgart (in German).

Bagdhadi, A.H.A and Mikhail, S. (1985). "Design of momentum water wheels used for mini hydropower". *International Water Power and Dam Construction, 47-52*.

Barelli, L., Liucci, L., Ottaviano, A., and Valigi, D. (2013). "Mini-hydro: A design approach in case of torrential rivers". *Energy, 58, 695-706*.

Barstad, L. F. (2012). "CFD analysis of a Pelton turbine", MSc Thesis from the Norwegian University of Science and Technology.

Batten, WMJ and Müller, G. (2011). "Potential for using the floating body structure to increase the efficiency of a free stream energy converter". *Proceedings of 34th International Association of Hydraulic Engineering & Research (IAHR) Biennial Congress, Brisbane, Australia, June 16 – July 1, 2011*.

Bódis, K., Monforti, F., and Szabó, S. (2014). "Could Europe have more mini hydro sites? A suitability analysis based on continentally harmonized geograph-

ical and hydrological data". *Renewable and Sustainable Energy Reviews, 37, 794-808*.

Bozhinova, S., Kisliakov, D., Müller, G., Hecht, V., and Schneider, S. (2013). "Hydropower converters with head differences below 2.5 m". *Proceedings of the ICE-Energy, 166(3), 107-119*.

Bozhinova, S., Petkova, S., Kisliakov, D., Müller, G., and Schneider, S. (2014). "Large Scale Model design and monitoring -HPM". *EC Services Deliverable Report No. 3.2*.

Bresse, M. (1869). *Hydraulic Motors*. J. Wiley and sons, New York.

Brockhaus, F.A. (1903). *Brockhaus konversations-lexicon, chapter: wasserraeder. 14th Jubilee edition, volume 16, Leipzig (in German)*.

Busquet, R. (1906). *A manual of hydraulics*. London, Edward Arnold.

Cadolini, G., Neumann, K., and Eytelwein, J.A. (1835). *L'architettura pratica dei mulini: trattata con metodi semplici ed elementari desunti dal Neumann e dall'Eytelwein: unitovi un ragguaglio sulla teoria delle ruote idrauliche, sulla fabbricazione delle ruote metalliche e sui perfezionamenti dell'arte di macinare, Milano*.

Capecchi, D. (2013). "Over and Undershot Waterwheels in the 18th Century. Science-Technology Controversy". *Advances in Historical Studies, 2(3), 131-139*.

Chaudy, F. (1896). *Machines hydrauliques*. Bibliothèque du conducteur de travaux publics. Published by Vve. C. Dunod et P. Vicq (in French).

Church, I.P. (1914). *Hydraulic Motors, with Related Subjects, Including Centrifugal Pumps, Pipes, and Open Channels, Designed as a Text-book for Engineering Schools*. Published by J. Wiley and sons.

Citrini, D., and Noseda, D. (2012). *Idraulica, Casa Editrice Ambrosiana, Milano*.

Cullen, W. (1871). *A Practical Treatise on the Construction of Horizontal and Vertical Water-wheels*. E. & F.N. Spon.

Denny, M. (2004). "The efficiency of overshot and undershot waterwheels". *European Journal of Physics, 25(2), 193-202*.

Fairbairn, W. (1864). *Treatise on Mills and Millwork, Longman Roberts and Green, London*. Longman Roberts and Green, London.

Garuffa, E. (1897). *Macchine motrici ed operatrici a fluido*. Meccanica industriale. Published by U. Hoepli (in Italian).

Gotoh, M., Kowata, H., Okuyama, T., and Katayama, S. (2001). "Characteristics of a current water wheel set in a rectangular channel". *Proceedings of the ASME fluids engineering division summer meeting, 2, 707-712*.

Hadler, J. and K. Broekel. (2011) "Low head hydropower–its design and economic potential". *Hydropower Applications, 6, 1464-1471*.

Helmizar. (2016). "Turbine wheel - a hydropower converter for head differences between 2.5 and 5 m". *PhD Thesis, University of Southampton*.

International Energy Agency. (2013). "World energy outlook", http://www.iea.org/newsroom/news/2016/november/world-energy-outlook-2016.html.

Laghari, JA., Mokhlis, H., Bakar, AHA., and Mohammad, H. (2013). "A comprehensive overview of new designs in the hydraulic, electrical equipments and controllers of mini hydro power plants making it cost effective technology". *Renewable and Sustainable Energy Reviews, 20, 279-293*.

Liu, Y.C., and Peymani, F.Y. (2015). "Development and computational verification of an analytical model to evaluate performance of paddle wheel in generating electricity from moving fluid". *Distributed Generation and Alternative Energy Journal, 30(1), 2015, 58-80*.

Logan, E. (2003). "Handbook of turbomachinery". *New York: CRC Press*.

Lubitz, WD., Lyons, M., and Simmons, S. (2014). "Performance Model of Archimedes Screw Hydro Turbines with Variable Fill Level". *Journal of Hydraulic Engineering, 140(10), 04014050.*

Luther, S., Wardana, I.N.G., Soenoko, R., and Wahyudi, S. (2013). "Performance of a Straight-Bladed Water-Current Turbine". *Advances in Natural and Applied Sciences, 7(5), 455-461*.

Meerwarth, K.D. *(1935). Experimentelle und theoretische Untersuchungen am oberschlächtigen Wasserrad. (Experimental and theoretical investigation of an overshot water wheel), Technical University of Stuttgart*. PhD thesis.

Menter, F. (1994). “Two-equation eddy-viscosity turbulence models for engineering applications”. *AIAA Journal, 32(8), 1598-1605*.

Müller, G. and Batten, WMJ. (2010). “Potential, performance limits and environmental effects of floating mills for energy generation in rivers”. *Proceedings of River Flow 2010, International Conference on Fluvial Hydraulics, Braunschweig, September 8-10, 2010*.

Müller, G., Denchfield, S., Marth, R., and Shelmerdine, R. (2007). “Stream wheels for applications in shallow and deep water”. *Proc. 32nd IAHR Congress, Venice, 32(2), 707-716*.

Müller, G., Jenkins, R., and Batten, W.M.J. (2010). “Potential, performance limits and environmental effects of floating water mills”. *University of Southampton, School of Civil Engineering and the Environment, Highfield, Southampton SO17 1BJ, UK, Dittrich, Koll, Aberle & Geisenhainer*.

Müller, G. and Kauppert, K. (2002). “Old watermills— Britain’s new source of energy?”. *Proceedings of the ICE-Civil Engineering, 12738, 178-186*.

Müller, G., Kauppert, K., and Rüdiger, M. (2002). “Back to the future”, *Water Power and Dam Construction*.

Müller, G., and Kauppert, K. (2004). “Performance characteristics of water wheels”. *Journal of Hydraulic Research, 42(5), 451-460*.

Müller, G., and Wolter, C. (2004). “The breastshot waterwheel: design and model tests”. *Proceedings of the ICE-Engineering Sustainability, 157(4), 203-211*.

Müller, W. (1899). *Die eisernen Wasserräder, Erster Teil: Die Zellenräder und Zweiter Teil: Die Schaufelräder*. Veit & Comp., Leipzig (in German).

Neumayer, H., Rempp, W., Ruppert, J., and Schwörer, R. (1979). “Untersuchungen am Wasserrad-Triebwerk der Kunstmühle W. Seifried KG, Waldkirch-Br. (Investigation of a water wheel power plant at the flour mill) W. Seifried KG, Waldkirch/Breisach, in German”. *Technical Report, University of Stuttgart, Germany*.

Nuernbergk, D.M. (2014). “Overshot water wheels - Calculation and Design”. *Verlag Moritz SchäferDetmold*.

Olsson, E., Kreiss, G., and Zahedi, S. (2007). “A Conservative Level Set Method for Two Phase Flow II”. *Journal of computational Physics, 225(1), 785-807*.

Osher, S., and Sethian, J.A. (1988). "Fronts Propagating with Curvature-dependent Speed: Algorithms Based on Hamilton-Jacobi Formulations". *Journal of computational Physics, 79(1), 12-49*.

Ovens, W.G. (1989). *A Design Manual for Water Wheels, Published by Volunteers in Technical Assistance (1989), International Reference Centre for community water supply*.

Pacinotti, L. (1851). *Esperienze e principi d' idraulica pratica e dottrina sulle macchine idrauliche* . University of Michigan Library.

Paish, O. (2002). "Small hydro power: technology and current status". *Renewable & Sustainable Energy Reviews, 6, 537-556*.

Paoli, L. (2006). *La costruzione di una ruota idraulica*. Editor Il Rostro, CAST.

Paudel, S. (2015). "Experimental and Numerical Study of Dethridge Wheel for Pico-scale Hydropower Generation". *University of Darmstadt, Germany, Doctoral dissertation*.

Paudel, S., Linton, N., Zanke, U., and Saenger, N. (2013). "Experimental investigation on the effect of channel width on flexible rubber blade water wheel performance". *Renewable Energy, 2013, 52, 1-7*.

Pelliciardi, V. (2015). "Overshot waterwheel to power an olive oil mill in Nepal". *Journal of Applied Water Engineering and Research, 3(2), 157-165*.

Poncelet, J.V. (1843). *Memoria sulle ruote idrauliche a pale curve, mosse di sotto, seguita da sperienze sugli effetti meccanici di tali ruote.* Translated by Errico Dombré, published by Dalla tipografia Flautina, Napoli *in Italian*.

Pujol, T., Solà, J., Montoro, L., and Pelegrí, M. (2010). "Hydraulic performance of an ancient Spanish watermill". *Renewable Energy, 35(2), 387-396*.

Pujol, T., Vashisht, A.K., Ricart, J., Culubret, D., and Velayos, J. (2015). "Hydraulic efficiency of horizontal waterwheels: Laboratory data and CFD study for upgrading a western Himalayan watermill". *Renewable Energy, 83, 576-586*.

Quaranta, E. and Müller, G. (2017). "Zuppinger and Sagebien water wheels for very low head hydropower applications with head differences between 0.3 and 1.5 m". *Journal of Hydraulic Research, under review*.

Quaranta, E., and Revelli R. (2016a). "Optimization of breastshot water wheels performance using different inflow configurations". *Renewable Energy, (97), 243-251*.

Quaranta, E., and Revelli R. (2016b). “Hydraulic behavior and performance of breastshot water wheels for different numbers of blades”. *Hydraulic Engineering, 10.1061/(ASCE)HY.1943-7900.0001229.*

Quaranta, E., and Revelli R. (2016c). “CFD simulations to optimize the design of water wheels: study case of an existing breastshot water wheel”. *14th International CCWI Conference 7-9 November 2016 – IWC, Computing and Control for the Water Industry*.

Quaranta, E., and Revelli, R. (2015a). “Performance characteristics, power losses and mechanical power estimation for a breastshot water wheel”. *Energy, (87), 315-325*.

Quaranta, E., and Revelli, R. (2015b). “Output power and power losses estimation for an overshot water wheel”. *Renewable Energy, (83), 979-987*.

Quaranta, E., and Revelli, R. (2017d). “Overshot water wheels: numerical simulations and improved design at high flow rates”, *under review*.

Sagebien, M. (1866). *La Roue Hydraulique Sagebien. Expériences sur la roue hydraulique Sagebien, précédées d’un Exposé du principe de ce nouveau moteur à aubes immergentes et à niveau maintenu dans les aubes.* Eugène Lacroix, Paris *in French*.

Santolin, A., Cavazzini, G., Pavesi, G., Ardizzon, G., and Rossetti, A. (2011). “Techno-economical method for the capacity sizing of a small hydropower plant”. *Renewable and Sustainable Energy Reviews, 52, 2533-2541*.

Senior, J., Saenger, N., and Müller, G. (2010). “New hydropower converters for very low-head differences”. *Journal of Hydraulic Research, 48(6), 703-714*.

Senior, J.A. (2009). “Hydrostatic pressure converters for the exploitation of very low head hydropower potential”. *PhD Thesis, University of Southampton*.

Terna Rete Italia. (2012). “Dati statistici sull’energia elettrica in Italia”.

Tevata, A., and Chainarong, I. (2011). “The Effect of Paddle Number and Immersed Radius Ratio on Water Wheel Performance”. *Energy Procedia, 9 (0), 359-365*.

Tresca M. (1870. *Roue de l’établissement hydraulique de Trilbardou, par M. Sagebien*. Bulletin de la Société d’encouragement à l’industrie nationale, Avril 1870, tome XVII, 193-205.

v. Harten, M., Paudel, S., and Saenger, N. (2013). “Nutzung kleiner Fallhöhen: aus Forschung und Entwicklung (Utilisation of small head differences: research and development, in German)”. *Proc. Tagung Kleinwasserkraft, Technical University of Stuttgart*.

Vermaak, HJ., Kusakana, K., and Koko, SP. (2011). “Status of micro-hydrokinetic river technology in rural applications: A review of literature”. *Renewable and Sustainable Energy Reviews, 29, 625-633*.

Vidali, C., Fontan, S., Quaranta, E., Cavagnero, P., and Revelli, R. (2016). “Experimental and dimensional analysis of a breastshot water wheel”. *Journal of Hydraulic Research, 54(4), 473-479*.

Wahyudi, B. and Faizin, A., and Suparman, S. (2013). “Increasing Efficiency of Overshot Waterwheel with Overflow Keeper Double Nozzle”. *Applied mechanics and materials, 330, 209-213.*

Waters, S., and Aggidis, G. (2015). “Over 2000 years in review: Revival of the Archimedes Screw from Pump to Turbine”. *Renewable & Sustainable Energy Reviews, 51, 497-505*.

Weidner, Carl. (1913). “Test of a Steel Overshot Water Wheel”. *Engng. News, 1913, No. 69(1), 39-41*.

Weidner, Carl. (1913). “Theory and Test of An Overshot Water Wheel”. *Bulletin of the University of Wisconsin No. 529, Engineering Series, 1913, 7(2), 117-254*.

Weisbach, J. (1849). *Principles of the mechanics of machinery and engineering.* Published by Lea and Blanchard, Philadelphia.

Williams, A. and Bromley, P. (2000). “New ideas for old technology-experiments with an overshot waterwheel and implications for the drive system”. *International Conference of Gearing, transmission and mechanical system, 781-790.*

Williamson, S. J., Stark, B. H., and Booker, J.D. (2014). “Low head pico hydro turbine selection using a multi-criteria analysis”. *Renewable Energy, 61, 43-50*.